

2018-01-08

# Discrete Fourier Transform Techniques to Improve Diagnosis Accuracy in Biomedical Applications

Adibpour, Paniz

---

Adipour, P. (2018). Discrete Fourier Transform Techniques to Improve Diagnosis Accuracy in Biomedical Applications (Master's thesis, University of Calgary, Calgary, Canada). Retrieved from <https://prism.ucalgary.ca>.

<http://hdl.handle.net/1880/106295>

*Downloaded from PRISM Repository, University of Calgary*

UNIVERSITY OF CALGARY

Discrete Fourier Transform Techniques to Improve Diagnosis Accuracy in Biomedical  
Applications

by

Paniz Adibpour

A THESIS

SUBMITTED TO THE FACULTY OF GRADUATE STUDIES  
IN PARTIAL FULFILMENT OF THE REQUIREMENTS FOR THE  
DEGREE OF MASTER OF SCIENCE

GRADUATE PROGRAM IN ELECTRICAL AND COMPUTER ENGINEERING

CALGARY, ALBERTA

JANUARY, 2018

© Paniz Adibpour 2018

## Abstract

Transforming acquired data in time or space is necessary for many applications, due to practical constraints on time-domain sampling at high data rates or the requirement for algorithms to process frequency-domain data during the image reconstruction procedure. Therefore, the discrete Fourier transform (*DFT*) plays an important role in many fields for preprocessing, reconstruction or data analysis stages of algorithms. The hardware or physical constraints also necessitate acquisition of limited length raw data which results in *DFT*-imposed distortions after data processing for which low pass filters are considered as general solution. Through this thesis, fundamental *DFT* properties are investigated and an optimization method is introduced to take advantage of these properties. This method is a potential alternative to low pass filters which impose resolution loss to processed data. The formalized method is examined and validated using preliminary observer metrics for two magnetic resonance imaging reconstruction approaches and a microwave imaging technique.

## **Acknowledgements**

Although words are not capable of expressing my gratitude to people who have helped me through my M.Sc. studies, I want to take this opportunity to say some words in appreciation of their continuous support.

I would like to first thank my dear supervisor, Dr. Smith, who was my “academic” father during these years and always had my back. Without his ideas, his knowledge, his patience and his support, the thesis could not be finished. He always guided me kindly and supported me with all new experiences even when some of them could put him under pressure. He will always hold a special respectable place in my heart not just as a supervisor but as a wonderful person I was lucky enough to meet in my life.

I would like to express gratitude to my dear co-supervisor, Dr. Fear, for her invaluable support, her extensive knowledge and her continuous motivation during my research experiments. She provided me with the opportunity to extend the scope of my thesis and explore ideas in new imaging areas. Her careful reviews and comments helped promoting my work. Her professional discipline and her kind and supportive attitude will always be my pattern. I am thankful for the opportunity I had to work with Dr. Fear.

I want to also thank Dr. Fapojuwo whose consultation and his open vision helped me a lot through my M.Sc. studies.

I want to thank all the people who provided me with datasets, Dr. MacDonald, university of Calgary and Dr. Chen, Rotman Research Institute, Canada and Dr. Lebel, GE (Calgary), Canada. Without their help, I couldn’t verify my methods and couldn’t present them successfully.

I want to acknowledge the financial support of this thesis project from the Natural Sciences and Engineering Research Council (NSERC) of Canada Create I3T program and the University of Calgary.

I would also like to thank all my colleagues in the SMILE lab especially Mila, Dino, Ehsan and Jordan, whose friendship and support provided a great work atmosphere.

I am thankful of so many good friends I collected in Calgary by whom I experienced many wonderful moments. Many thanks to all who were there always for me and made my experience in Canada feel like home, especially Setareh and Mahshid.

I couldn't have done any of this without the endless love and support of my family, my mom Fariba, my dad Mehran, my wonderful brother Navid and my amazing sister Nasim who always supported me and encouraged me with all new experiences even when my decision of continuing education in Canada ended up me being far from them. I thank God, a million times, for being raised in such a precious family.

Last but not the least, I want to thank my special friend, Arash, who always believed in me and gave me his endless support and love during my M.Sc. studies and years of far from home. I am grateful of his presence in my life.

## **Dedication**

*To my beloved Parents  
whom I owe every success of my life*

## Table of Contents

Abstract .....	ii
Acknowledgements .....	iii
Dedication .....	v
Table of Contents .....	vi
List of Tables .....	ix
List of Figures and Illustrations .....	x
List of Symbols, Abbreviations and Nomenclature .....	xiii
 <b>Chapter One: Introduction .....</b>	<b>1</b>
1.1 Statement of the Problem .....	1
1.2 Objectives of this research .....	4
1.3 Thesis outline .....	5
1.4 Research contribution .....	6
 <b>Chapter Two: Background and Literature Review .....</b>	<b>9</b>
2.1 Introduction .....	9
2.2 Principles of Magnetic Resonance Imaging .....	10
2.2.1 Nuclear magnetic resonance .....	10
2.2.1.1 <i>Precession and Relaxation Procedures</i> .....	11
2.2.1.2 <i>Spatial Encoding Gradients</i> .....	12
2.2.2 MR Image Formation .....	12
2.3 Temporal vs. Spatial Resolution .....	14
2.4 Basic DFT reconstruction introducing Gibbs' artifacts .....	17
2.4.1 DSP relationship between high- resolution and low-resolution images of 1D objects .....	19
2.4.2 Truncation effects on isolated high intensity object close to a smoother broad region of interest .....	21
2.4.3 Fourier shift manipulation to increase basis function characteristics .....	24
2.5 Sparse reconstruction techniques .....	25
2.5.1 Positional dependent resolution of sparse reconstruction techniques .....	27
2.6 Validation tools in imaging applications .....	28
2.6.1 SSIM metric .....	30
2.6.1.1 <i>SSIM Index</i> .....	30
2.6.1.2 <i>Quality Assessment Using SSIM Index</i> .....	33
2.6.2 HDR-VDP-2.0 metric .....	33
2.6.2.1 <i>Optical and Retinal Pathway</i> .....	34
2.6.2.2 <i>Visibility metric</i> .....	36
2.6.2.3 <i>Image quality prediction</i> .....	36
2.7 Summary of the Chapter .....	36
 <b>Chapter Three: Proposed Methods in Compressed Sensing Algorithms (I) .....</b>	<b>38</b>
3.1 Introduction .....	38
3.2 Overview of the concept of Improved Compressed Sensing Resolution through Optimization of Basis Function Sparse Representation .....	39
3.3 Detailed background to MRI DFT and sparse reconstructions .....	40

3.4 Theory .....	42
3.4.1 CS-MRI with analytical sparse representation .....	43
3.4.2 Basis and non-Basis function characteristics of truncated frequency components .....	45
3.5 Proposed Alternative CS-MRI Formulation .....	47
3.5.1 Re-sparsification of basis function representation of finite length Frequency Components .....	47
3.5.2 Alternative CS-MRI with Analytical Sparse Representation .....	51
3.6 Method .....	52
3.6.1 Gibbs' Correction using FSM Estimation from initial preparatory scans .....	53
3.6.2 Gibbs' correction using FSM estimation from zero-filled under-sampled data .....	55
3.6.3 Quantitative metrics to compare standard and FSM supported CS reconstructions .....	56
3.6.4 CS software and dataset materials .....	57
3.7 Results and Discussion .....	57
3.7.1 Experimental Results .....	58
3.7.2 Performance measure of the proposed techniques .....	60
3.8 Conclusion and Future Work .....	63
3.9 Summary of the Chapter .....	64
 <b>Chapter Four: Proposed Methods in Compressed Sensing Algorithms (II) .....</b>	<b>65</b>
4.1 Introduction .....	65
4.2 Overview of the concept of Improved Dictionary learning CS MRI through Patch based TV regularization .....	66
4.3 Detailed background to CS MRI techniques and Motivation for the proposed methods .....	66
4.4 Theory .....	68
4.4.1 DL-MRI based on adaptive sparse representation .....	68
4.4.2 Positional resolution enhancement in DL-CS .....	69
4.5 Proposed Alternative DL-MRI Formulation .....	71
4.6 Materials and Methods .....	73
4.6.1 Proposed Design Pattern in DL-MRI Pipeline .....	74
4.6.2 Quantitative metrics to compare DL-CS and patch-based TV Regularization reconstructions .....	75
4.6.3 Imaging Details .....	76
4.7 Results and Discussion .....	77
4.7.1 Experimental results .....	77
4.7.2 Performance Measure of Proposed method .....	78
4.8 Conclusion and Future Work .....	80
4.9 Summary of the Chapter .....	81
 <b>Chapter Five: Alternative preprocessing for radar-based microwave imaging .....</b>	<b>82</b>
5.1 Introduction .....	82
5.2 Detailed background to microwave imaging and tissue sensing adaptive radar method .....	83
5.2.1 Tissue sensing adaptive radar .....	85
5.3 Preprocessing calculations in TSAR software .....	86



5.3.1 Necessary TSAR Preprocessing Steps and source of artifacts .....	86
<b>Chapter Six: Improving basis function characteristics of backscattered signals .....</b>	<b>91</b>
6.1 Introduction.....	91
6.2 Fourier manipulation of backscattered signals to improve basis function characteristics .....	92
6.3 Methods and materials .....	93
6.3.1 Simulated realistic breast models .....	93
6.3.2 Total variation optimization of Fourier manipulated back scattered signals ..	95
6.3.3 TSAR Pipelines .....	97
6.3.4 Measurement criteria .....	98
6.4 Results and discussions.....	99
6.4.1 Analysis of oversampling techniques .....	99
6.4.2 comparison of backscattered signals using three pipelines .....	100
6.4.3 Comparison of TSAR image maps.....	103
6.5 Conclusion and Future work.....	107
<b>Chapter Seven: Conclusion and Future Work.....</b>	<b>109</b>

## **List of Tables**

Table 6-1 simulated breast models .....	95
Table 6-2 Measurements on 2D cross sections of the maximum responses.....	100

## List of Figures and Illustrations

Figure 1.1 A) High resolution image, and associated cross-sections, from a <i>IDFT</i> reconstruction of large (full <i>k</i> -space data set with high resolution detail superimposed upon finer detail. B) Low resolution <i>IDFT</i> reconstruction of truncated (smaller) <i>k</i> -space data set. C) <i>IDFT</i> reconstruction of the apodized truncated <i>k</i> -space, data set show resolution loss across the full image. D) Reconstruction of the undersampled truncated <i>k</i> -space data set. A representation of the <i>K</i> -space data set is provided adjacent to each dataset. Red arrows demonstrates features mostly affected by <i>DFT</i> -imposed artifacts. ....	2
Figure 2.1 A) 512x512 <i>IDFT</i> reconstruction of full <i>k</i> -space, B) 108x018 <i>IDFT</i> reconstruction of truncated <i>k</i> -space, C) 108x108 sparse sampled reconstruction of undersampled <i>k</i> -space, D) 108x108 <i>IDFT</i> reconstruction of apodized <i>k</i> -space, with upper and lower cross sections of tine features and tines on top of a broad feature. <i>K</i> -space representation of each reconstructed image is provided below each dataset. Red arrows demonstrates features mostly affected by <i>DFT</i> -imposed artifacts.....	18
Figure 2.2 <i>K</i> -space truncated Continuous (broken line) and discrete (solid points) point spread functions of A) and B) sampled isolated fine detail objects with different positioning characteristics in <i>FOV</i> in terms of basis function representations. ....	20
Figure 2.3 A) 1D phantom containing one isolated narrow-width image component and a fine detail on top of a broad constant intensity image feature. The isolated narrow width peak (B) retains a higher intensity and narrower half intensity width (one with basis function representations) than the peak (C) (one with non-basis function representations) despite being sampled versions of the same continuous point spread functions (dotted line). Of particular interest is that the distortions from the discrete power spread function are enhanced when the peak with non-basis function characteristics is close to a broad feature, left side of Fig. 2C. ....	22
Figure 2.4 A) 512x512 <i>IDFT</i> reconstruction of full <i>k</i> -pace, B) 108x108 <i>IDFT</i> reconstruction of truncated <i>k</i> -space, C) 108x108 CS reconstruction of truncated <i>k</i> -space. All Lower <i>ROIs</i> have 0.4% <i>FOV</i> position shift with respect to upper <i>ROIs</i> .....	28
Figure 2.5 A) High-resolution <i>IDFT</i> reconstruction of GE data, B) High-resolution <i>IDFT</i> reconstruction plus gaussian noise, C) Low-resolution <i>k</i> -space truncated <i>IDFT</i> reconstruction. The <i>MSE</i> values under B and C doesn't correctly reflect the poor structural resolution of images. ....	29
Figure 2.6 Pipeline of <i>SSIM</i> metric modified from (©2004 IEEE) showing where and how necessary structural information are captured from test and reference images and combined into one descriptive numerical value reflecting the similarity measure.....	32
Figure 2.7 Pipeline of <i>HDR-VDP2.0</i> metric modified from (© Maniutik et al., 2011) showing procedure of how necessary information are acquired from reference and test images and combined into a descriptive numerical value reflecting the quality of test image compared to reference. ....	34

Figure 3.1 Sparse signal reconstruction of (A) 512-length high resolution signal, from (B) pseudo-random $k$ -space under sampling by thresholding technique. (C) Following $k$ -space data truncation, Gibbs distortions are introduced into the left patch signal peaks. (D) The true intensity and peak width will not be recovered from the under-sampled truncated data set using a thresholding technique. Applying a frequency upshift multiplication technique to shift the left patch peak positions by 0.25 of the pixel resolution recovers the true left patch peak intensity and width in both (E) the fully sampled and (F) under-sampled data sets. ....	50
Figure 3.2 A) The existing $CS$ pipeline can be modified to remove Gibbs' artifacts independently of under-sampling noise using $FSM$ estimates derived from B) a preparatory full $k$ -space scan or C) estimates derived from a zero-filled under-sampled data set. ....	54
Figure 3.3 A) The high resolution $DFT$ reconstruction from a 512 x 512 GE data set are compared to B) a standard $SPARSE-MRI$ $CS$ reconstruction, and $FSM$ supported reconstructions using $FSM$ estimates from C) the preliminary scan and D) low-pass filtered zero-filled sparse sampled data. ....	59
Figure 3.4 Zoomed portion of A) The high resolution $DFT$ reconstruction from a 384 x 384 renal study GE data set are compared to B) a standard $SPARSE-MRI$ $CS$ reconstruction, and $FSM$ supported reconstructions using $FSM$ estimates from C) the preliminary scan and D) low-pass filtered zero-filled sparse sampled data. ....	60
Figure 3.5 A) $HFEN$ , B) $SSIM$ -Contrast, C) $SSIM$ -Luminance, D) $SSIM$ -Structure measures applied on 108x108 GE $k$ -space $CS$ reconstructed using Sparse $MRI$ (blue lines), optimized Sparse $MRI$ with $FSM$ information acquired from zero-filled ( $ZF$ ) data (red lines) and optimized Sparse $MRI$ with $FSM$ information acquired from $IDFT$ of reference scan (yellow lines). ....	62
Figure 3.6 A) $HFEN$ , B) $mean$ - $SSIM$ measures applied on 128x128 Renal $k$ -space $CS$ reconstructed using Sparse $MRI$ (blue lines), optimized Sparse $MRI$ with $FSM$ information acquired from zero-filled ( $ZF$ ) data (red lines) and optimized Sparse $MRI$ with $FSM$ information acquired from $IDFT$ of reference scan (yellow lines). ....	63
Figure 4.1 A) $DFT$ reconstruction of a truncated data set is compared to B) $CS$ reconstruction using 33% of the data. ....	70
Figure 4.2 A) The existing $DL-MRI$ pipeline can be modified to remove Gibbs' artifacts independently of under-sampling noise using $FSM$ estimates derived from B) a preparatory full $k$ -space scan. ....	75
Figure 4.3 A) The high resolution $DFT$ reconstruction from a 512 x 512 GE data set are compared to B) a standard $SPARSE-MRI$ $CS$ reconstruction, C) a standard $DL-MRI$ $CS$ reconstruction and D) $patch$ -based $TV$ regularized $DL-MRI$ reconstructed with $FSM$ estimates from $IDFT$ of initial scan. ....	77

Figure 4.4 A) <i>HFEN</i> , B) <i>HDR-VDP</i> (%), C) <i>SSIM</i> -Luminance, D) <i>SSIM</i> -Contrast, E) <i>SSIM</i> -Structure measures applied on 108x108 GE <i>k</i> -space <i>CS</i> reconstructed using <i>DL-MRI</i> , optimized <i>DL-MRI</i> with <i>FSM</i> informaion acquired from <i>IDFT</i> of reference scan.....	79
Figure 5.1 Backscattered signals in preprocessing <i>TSAR</i> pipeline; Calibrated signal in A) frequency and B) time; signals after frequency truncation in C) frequency and D)time; signal after skin response subtraction in E) frequency and F) time; signals shifted to the aperture position in G) frequency and H) time; .....	88
Figure 6.1 Left: Computer-generated model of the breast phantom; © 2015 IEEE; Right: schematic of antenna and test object in simulation model; screenshot from SEMCAD @C.Curtis (Curtis, 2015) .....	94
Figure 6.2 It demonstrates how <i>TSAR</i> software generates three different slices of 3D simulated model; .....	95
Figure 6.3 Three pipelines for preprocessing procedure of <i>TSAR</i> software different in highlighted sections. Pipeline1: Without pulse shaping; Pipeline2: with pulse shaping; Pipeline3: <i>TV</i> optimized of Fourier shifted signals.....	97
Figure 6.4 Backscattered signals following three <i>TSAR</i> pipelines; A-1)frequency and B-1)time; signals after application of pipeline 1, baseline; A-2)frequency and B-2)time; signals after application of pipeline 2, baseline + <i>LPF</i> ; A-3)frequency and B-3)time; signals after application of pipeline 3, baseline + <i>TV-FSM</i> ; .....	102
Figure 6.5 Images of tumor only models .....	105
Figure 6.6 Images of more sophisticated models.....	106
Figure 6.7 Tumor position error.....	107

## List of Symbols, Abbreviations and Nomenclature

Symbol	Definition
DFT	Discrete Fourier Transform
IDFT	Inverse Discrete Fourier Transform
fMRI	Functional Magnetic Resonance Imaging
MR	Magnetic Resonance
CS	Compressed Sensing
MRI	Magnetic Resonance Imaging
TSAR	Tissue Sensing Adaptive Radar
DL	Dictionary Learning
CSMRI	Compressed Sensing Magnetic Resonance Imaging
RF	Radio Frequency
FOV	Field of View
TE	Time of Echo
TR	Repetition Time
T2WI	T2 Weighted Imaging
DWI	Diffusion Weighted Imaging
EPI	Echo Planar Imaging
SNR	Signal-to-Noise Ratio
PSF	Point Spread Function
ICFT	Inverse Continuous Fourier Transform
FT	Fourier Transform
FSM	Fourier Shift Manipulation
ROI	Region of Interest
FDCT	Fast Discrete Curvelet Transform
DST	Discrete Shearlet Transform
SFLCT	Sharp Frequency Localization Contourlet Transform
TEI	Transfer Edge Information
MSE	Mean Squared Error
MI	Mutual Information
HVS	Human Visual System
SSIM	Structural Similarity Index Map
HDR-VDP	High Dynamic Range Visual Difference Predictor
MOS	Mean Opinion Score
PSNR	Peak-Signal-to-Noise Ratio
MS-SSIM	Mean Score-Structural Similarity Index Map
TV	Total Variation
ZF	Zero-Filled
HFEN	High Frequency Error Norm
DL-MRI	Dictionary Learning-Magnetic Resonance Imaging
DL-CS	Dictionary Learning-Compressed Sensing
LPF	Low Pass Filter

PET	Positron Emission Tomography
CMI	Confocal Microwave Imaging
VNA	Vector Network Analyzer
ICZT	Inverse chirp Z-Transform
ISS	Ideal Skin Subtraction
RSS	Realistic Skin Subtraction
TV-FSM	Total Variation-Fourier Shift Manipulation
SCR	Signal-to-Clutter Ratio
FWHM	Full Width at Half Maximum
PL	Piecewise Linear
NN	Nearest Neighbor
PCH	Piecewise Cubic Hermite
CCR	Contrast-to-Clutter Ratio

## Chapter One: Introduction

### 1.1 Statement of the Problem

In many technologies, practical constraints on sampling time domain signals at high data rates when acquiring raw data has led to investigations into Fourier domain data acquisition and manipulation prior to further data interpretation. Data needs to be consistently transformed during the pre-processing or data reconstruction procedures to fulfill the requirements of algorithms such as discrete Fourier transform (*DFT*) reconstruction in magnetic resonance (*MR*) imaging applications. However, the constraints applied on raw data due to hardware limitations or the limited acquisition of data due to physical constraints appear in the form of distortions imposed on the transformed data each time the *DFT* is used for transformation of data between Fourier-space or Fourier-time domains (Chilla, 2015; Smith, 1993). The distortions created in pre-processing stages propagate through the algorithmic pipeline and may intensify in the final interpretable data, including the diagnostic results acquired from imaging techniques in biomedical applications.

We illustrate this issue with a biomedical application example. In Fig. 1.1A, a high resolution magnetic resonance image has been reconstructed by applying an inverse discrete Fourier transform (*IDFT*) to a large (full) *k*-space data set. The image shows two regions of interest (*ROI*) comprising of a fine detail comb superimposed upon a broader feature. The cross-sections clearly illustrate that there is little distortion surrounding the fine detail in the image, green arrows. Fig. 1.1B illustrates the result of a simulated functional magnetic resonance imaging (*fMRI*) reconstruction where, because of practical constraints, images have had to be reconstructed by applying the *IDFT* to a smaller, truncated, *k*-space data set. The image is impacted, red-arrows, by the well-known Gibbs' artifacts of intensity loss of fine detail, and



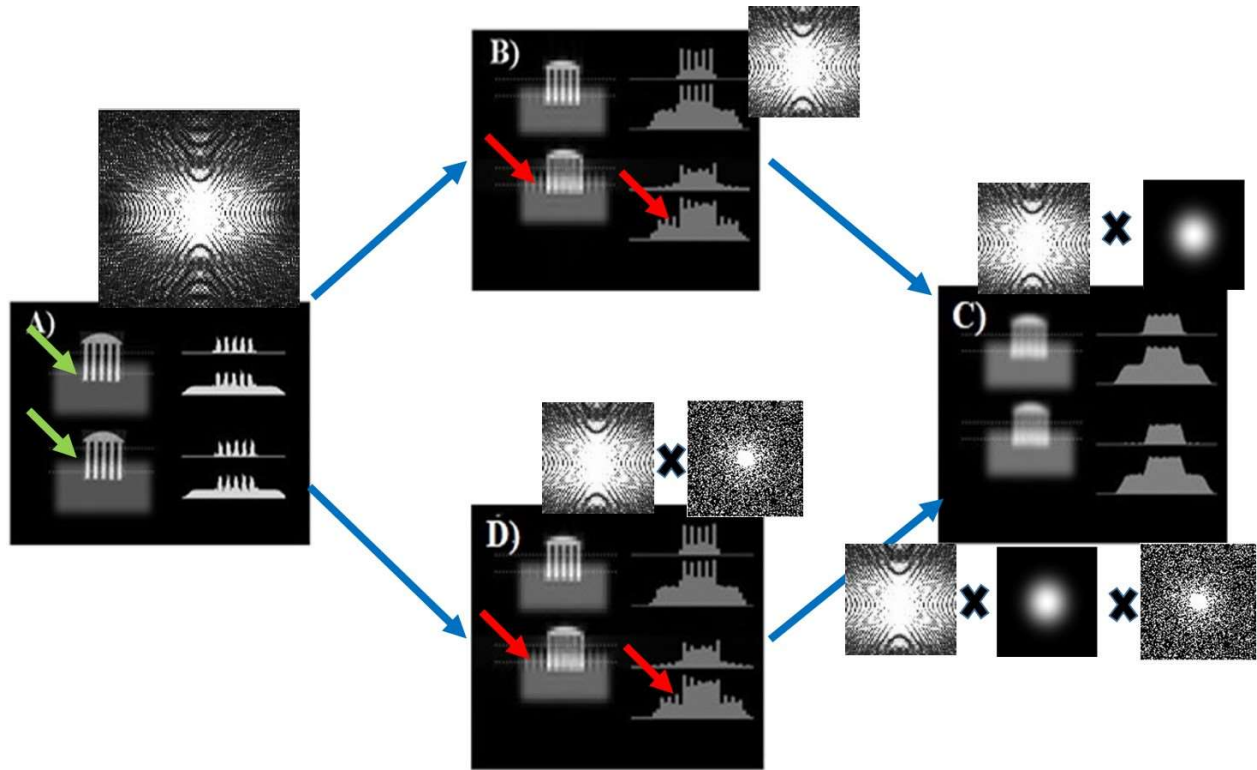


**Figure 1.1** A) High resolution image, and associated cross-sections, from a *IDFT* reconstruction of large (full  $k$ -space data set with high resolution detail superimposed upon finer detail. B) Low resolution *IDFT* reconstruction of truncated (smaller)  $k$ -space data set. C) *IDFT* reconstruction of the apodized truncated  $k$ -space, data set show resolution loss across the full image. D) Reconstruction of the undersampled truncated  $k$ -space data set. A representation of the  $K$ -space data set is provided adjacent to each dataset. Red arrows demonstrates features mostly affected by *DFT*-imposed artifacts.

blurriness associated with ringing around, and increased width of, image final detail (Dyrby et al., 2011; Ferreira et al., 2009; Harris, 1978; Jesmanowicz et al., 1998; Peled and Yeshurun 2001). A common approach to remove Gibbs's artifacts is the pre-processing application of an apodizing, low pass filter, to the truncated  $k$ -space data set before reconstruction. As can be seen in Fig. 1.1C, this approach removes the ringing artifacts at a cost of an overall resolution loss.

Under-sampling of the truncated  $k$ -space data is another approach to improve time resolution during *MR* imaging. Fig. 1.1D shows the compressed-sensing reconstruction, another *DFT*-based algorithm, of an under-sampled data set. Gibbs' artifacts are again present, an application of an apodizing filter leads to a low resolution image, Fig. 1.1C, equivalent to that of the apodized *DFT* reconstruction.

These artifacts are a common problem in other biomedical areas such as microwave imaging (Curtis et al., 2017) techniques for which limited bandwidth of acquired frequency signals and several time-to-frequency transformations during re-processing steps leads to processed signals with Gibbs' artifacts. Gibbs' ringing artifacts manifest at tissue boundaries and destroy the fine detail structure of tissues by decreasing the effective resolution, and introduces distortions in neighboring regions. In microwave imaging, the final interpretable data are images reconstructed from back-scattered microwave signals from breast tissue. Intensity loss and other artifacts present in back-scattered signals affect the accuracy of tumor detection in the reconstructed images. This indicates the importance of reliability and accuracy of pre-processing algorithms in biomedical pipelines to mitigate non-idealities of processed signals.

In *fMRI* applications, the Gibbs' effects may distort the relative intensity changes of signals through successive scans. This can affect the diagnostic results of stroke or hemorrhage in the brain (Gallichan et al., 2009). Considering this importance, many *MR* studies have focused on novel methods to improve resolution accuracy of final interpretable images by providing more reliable techniques for artifact removal. However, there is always a trade-off with the proposed approaches between lower contrast-to-noise ratio, lower temporal resolution or loss of details in exchange for data consistency (Plenge et al., 2012). A balance commonly discussed in

the literature is to take advantage of low pass filtering, or data windowing, to reduce Gibbs artifacts, an approach where resolution loss is inevitable.

Similar effects were discussed in an early paper by our group (Smith, 1993). There, *DFT*-imposed artifacts impacted the investigation of the operational efficiency of compressors used to pump natural gas down a pipeline. A new data manipulation approach was proposed to achieve higher accuracy without the resolution cost of filtering. However, at the time, the approach seemed highly customized to a particular, very specialized, industrial situation, and was not extended to other fields.

Recently, our team identified that a possible relationship exists between the solution to that industrial resolution problem and issues in *DFT* and compressed sensing reconstruction (Smith et al., 2013). The goal of this thesis is to formalize that relationship theoretically. By experimentally validating this new approach in two different imaging fields, we aim to demonstrate the general potential for applying these techniques to improve the resolution of *DFT*-based algorithms in many fields.

## **1.2 Objectives of this research**

As discussed in the previous section, reliable signal processing algorithms providing final images with improved resolution are a must in biomedical applications. I recently contributed to the identification that the (Smith, 1993) industrial solution can be considered an early example related to a new research area, dictionary learning in compressed sensing (Ravishankar et al., 2011). I extend that approach through this thesis to introduce a formalized general method for re-sparsification of *DFT* basis components to improve effective resolution in *DFT* and compressed sensing reconstruction applications. Such an approach is expected to provide both

improved resolution accuracy and data consistency when compared to other commonly used algorithms. This re-sparsification of *DFT* basis components will then be presented as an adaptive algorithm using a total variation optimization of frequency manipulated data. I have investigated, theoretically and empirically, the applicability of the proposed idea in advanced *MR* reconstruction techniques, common compressed sensing (*CS*) algorithms (Lustig et al., 2007; Ravishankar et al., 2011), and one of the recent microwave imaging techniques, tissue sensing adaptive radar (*TSAR*) (Sill and Fear, 2005). The proposed changes are then validated using several quantitative and qualitative metrics.

### 1.3 Thesis outline

In Chapter 2, the background of *MRI* and *fMRI* and the literature review of existing *DFT*-based data reconstruction algorithms are provided. Current solutions introduced in literature to mitigate *DFT*-imposed artifacts are discussed, with the shortcomings of such methods in balancing the trade-off between high temporal and spatial resolution in *MRI* applications detailed. This chapter also provides an introduction of metrics used in this thesis to emphasize the importance of appropriate choice of validation methods. An important lack in current literature studies on signal processing algorithms in imaging contexts is neglecting the appropriate choice of such metrics. These metrics help to validate the robustness of algorithms and also suggest hints on where algorithms fail when applied to a specific target. Two visual comparison techniques are developed to provide preliminary observer metrics for comparison of test and reference images in biomedical applications. The background discussion of a specific microwave imaging technique (tissue sensing adaptive radar - *TSAR*), also a target of this thesis, has been moved to Chapter 5 in order to keep the three Chapters associated with *MR* together.

Chapter 3 focuses on extending a common *MR* sparse reconstruction algorithm and shows how formalizing our general re-sparsification data manipulation technique leads to the ability to independently address Gibbs artifacts within the *CS* context. A modification to the algorithmic reconstruction pipeline of this compressed sensing algorithm is demonstrated. Chapter 4 takes advantage of a similar approach within an advanced sparse reconstruction algorithm known as dictionary learning *MRI*. Experimental and numerical results are provided, indicating performance of proposed reconstruction procedure compared to the original commonly used algorithm.

This thesis is intended to show that the increase in resolution by independently suppressing Gibbs artifacts is generally applicable to *DFT*-based algorithms in many fields. To demonstrate this potential, Chapter 5 and 6 focus on the removing equivalent *DFT*-imposed artifacts within the preprocessing procedure of *TSAR* microwave imaging technique with Chapter 5 focusing on background and 6 focusing more on methodology and discussion of results. A brief discussion of the tissue sensing adaptive radar (*TSAR*) microwave imaging technique is provided in chapter 5 as an example of *DFT*-based algorithms in a completely different imaging field. Then an approach is introduced in chapter 6 to formalize this issue within the *TSAR* preprocessing pipeline. Chapter 7 provides a conclusion and discusses possible future extensions.

## 1.4 Research contribution

I had a contribution in developing the theory of when Gibbs' artifacts are present in low resolution images and investigated improved techniques to automatically determine when Gibbs' effects will destroy useful information. After investigating the idea in common reconstructions, e.g. *IDFT*, I investigated more advanced *MR* reconstruction techniques, e.g. compressed sensing

(CS), for which Gibbs' artifacts are overlooked or are serendipitously removed through the standard regularization procedure but with an associated cost of resolution loss and increased blurriness in the final CS images.

I have investigated two common CS implementations, *Sparse MRI* (Lustig et al., 2007) and *CSMRI* based on dictionary learning (DL) (Ravishankar et al., 2011), and proposed how the theory of CS can be modified to improve the accuracy of CS techniques, i.e. improvement in contrast-to-noise ratio with minimum resolution loss. I have formalized an approach discovered in (Smith, 1993), a method to improve frequency analysis resolution, and extended this approach in the form of a general, adaptive algorithm to two different sparse reconstruction algorithms. Next, I have investigated the effect of proposed developed method in improving the tumor detection accuracy of *TSAR* and proposed changes to *TSAR* pre-processing pipeline to substitute the common low pass filtering which inevitably lowers the resolution of final images.

I was first author of the following papers presented or submitted in local and international conferences based on aspects of this thesis:

- **Adibpour, P.**, Smith, M., (June, 2015). An Approach to Improve the Effectiveness of Wavelet and Contourlet Compressed Sensing Reconstruction. *24th International Society of Magnetic Resonance in Medicine, Toronto, Canada.*
- **Adibpour, P.**, Smith, M. R., (2016). Total Variation Assisted Fourier Shift Manipulation to Remove Gibbs' Artifacts in Compressive Sensing Techniques. *IEEE MIC, Strasbourg, France, Poster Presentation.*
- **Adibpour, P.**, Fear, E., Smith, M., (2018). Improved Dictionary learning compressed sensing for MRI through Patch-based total variation regularization. *Submitted October 2017 for IEEE International Conference on Acoustics, Speech and Signal Processing (ICASSP), Calgary, Canada.*

Chapters in this thesis form the basis of the following journal papers for which I will be the first author:

- **Adibpour, P.**, Fear, E., Smith, M., (2017). Improved Compressive Sensing Resolution through Optimization of Basis Function Sparse Representation. *Ready for submission to IEEE Transaction on Computational Imaging by late January 2018.*
- **Adibpour, P.**, Smith, M., Fear, E., (2017). Fourier manipulation of Tissue Sensing Adaptive Radar data to improve Tumor Detection Accuracy by Gibbs' Ringing Removal. *Under revision for submission to IEEE Transactions on Computational Imaging or Progress in Electromagnetics Research by March 2018.*

I was also a major contributor and co-author on the following conference papers and international presentations

- Smith, M. R., MacDonald, M. E., Woehr\* J. and **Adibpour\* P.**, (June, 2015). Overcoming the Image Position-Dependent Resolution Inherent in DFT and CS Reconstructions. *24th International Society of Magnetic Resonance in Medicine, Toronto, Canada.*
- Shahrabi\*, E., **Adibpour\*, P.** and Smith, M. R., (May, 2016). Application of a Fourier Shift Preprocessing Stage to Improve the resolution of resting state fMRI images. *Proceedings of 32nd Canadian Medical and Biological Engineering Society. 32nd Canadian Medical and Biological Engineering Society, Calgary, Canada (A4 #4).*
- Smith, M. R., **Adibpour\*, P.**, Woehr\*, J., McDonald M. E. and Choudhury\*, S. H., (2014). To DSP or not to DSP; An overview of algorithms in the world of MRI. *IEEE EMBS and IEEE SP Societies, Melbourne, Australia.*
- Smith, M. R., **Adibpour\* P.**, Woehr\*, J., McDonald, M. E. and Choudhury \*, S. H., (2014). MRI and Signal Processing. *Digital signal processing class, Electrical and Computer Engineering, University of Melbourne, Melbourne, Australia.*

## Chapter Two: **Background and Literature Review**

### **2.1 Introduction**

The conflicting needs of spatial and temporal resolution in imaging applications is challenging in terms of their effects on diagnostic results and have attracted the focus of many studies. As discussed in the previous chapter, this thesis focuses on spatial and temporal trade-offs in two different imaging applications, *fMRI* and *TSAR*. These algorithms are both highly dependent on *DFT*-based reconstruction or pre-processing data manipulations and are subject to the loss of effective resolution due to temporal resolution restrictions. In this chapter, the background of *MRI*, the necessary data manipulation including pre-processing, post-processing and reconstruction procedures are discussed in detail. Current and recent studies focusing on improvement of diagnostic results via enhancement of the accuracy of structural differentiation of different anatomies in final image maps are also reviewed. This chapter bridges between *DFT* specific properties and the possibility of Fourier manipulation as a means to enhance *DFT*-imposed artifacts in *DFT*-based applications.

In this chapter, section 2.2 covers the fundamentals of *MR* imaging and principles of *MR* data acquisition. Section 2.3 outlines important challenges of *MR* imaging from scanning procedures to reconstruction techniques, temporal versus spatial resolution, and provides a brief literature review of existing post-processing algorithms developed to address resolution accuracy enhancement. Then basic *DFT* reconstructions and *DFT*-imposed artifacts, e.g. Gibbs artifacts, associated with constrained data gathering in low resolution *MR* applications are discussed in section 2.4. This section opens the door to alternative resolution enhancement techniques by taking advantage of *DFT* properties. Section 2.5 covers one of the common *DFT*-based reconstructions, sparse reconstruction, which is the focus of next two chapters. The final section



provides a brief review of common validation metrics used in *MR* studies. Considering the shortcomings of such metrics, two techniques are introduced and used as validation criteria for algorithms proposed in *MR* context through this thesis.

## 2.2 Principles of Magnetic Resonance Imaging

In the next sections, first the physics of *MRI*, data acquisition technique and *MR* data interpretation are discussed. The next section covers *MR* image formation method and interpretation of final *MR* data in the form of a Fourier transformation of acquired data.

### 2.2.1 Nuclear magnetic resonance

The physics of magnetic resonance imaging (*MRI*) is based on nuclear magnetic resonance (*NMR*) concepts which will be described using classical physics ideas, at a macroscopic scale, in this and the following sections (Bernstein et al., 2004; Haacke et al., 1999; Liang and Lauterbur, 1999). The protons in the body possess a magnetic moment due to their nuclear spin. The sum of all magnetic moments is termed the net magnetization, and is zero in the absence of an external field. In the presence of an external field ( $B_0$ ) there is a net magnetization ( $M_0$ ) oriented aligned with the static field. The external field is 1.5T or 3T for human scanning and is typically generated using superconducting magnets.

The alignment of individual protons with the external field can be described as parallel or anti-parallel to the main field. In a classical description, the protons gyrate (precess) around the  $B_0$  field, at the Larmor frequency  $f_0 = (\frac{\gamma}{2\pi})B_0$ , where  $\frac{\gamma}{2\pi}$  is the constant gyromagnetic ratio (42.57MHz / T) (Haacke et al., 1999). The spin magnetization vector of protons has two

orthogonal components, a transverse component which lies on the  $X$ - $Y$  plane and a longitudinal  $Z$  component which in total is aligned with the external field ( $B_0$ ).

The Bloch equation describes how the magnetization  $m$  changes in time (Hinshaw and Lent, 1983):

$$\frac{dm}{dt} = m \times \gamma B_0 + \frac{m_0 - m_z}{T_1} + \frac{m_{xy}}{T_2} \quad (2.1)$$

where  $m_0$ ,  $m_z$ ,  $m_{xy}$  are equilibrium, longitudinal and transverse magnetization and  $\gamma$ ,  $T_1$  and  $T_2$  are constants specific to types of tissues and materials. The external field homogeneity is very important since inhomogeneity results in image artifacts (Lustig et al., 2008).

### **2.2.1.1 Precession and Relaxation Procedures**

The key information for *MRI* image is obtained by modifying a proton's magnetization vector's precession. If a magnetic field ( $B_1$ ) generated by radiofrequency (*RF*) excitation perpendicular to  $B_0$  is applied, the magnetic resonance which is the interaction between spins and *RF* signal, happens. Through this interaction, spins whose Larmor frequency is the same as the frequency of *RF* pulse, will absorb energy from *RF* signal and transit to the higher energy state through a procedure called *excitation*. The longitudinal component of the magnetization,  $M_0$ , decreases and the transverse component,  $m_{xy}$ , increases. The transverse magnetization at position  $r$  and time  $t$ , denoted by  $m(r, t)$ , is a complex quantity which represents physical properties, e.g. proton density of tissues, relaxation and other information. The transverse magnetization induces a change of voltage in the receiver coil (tuned to the Larmor frequency).

This received *MR* signal is a complex harmonic describing contributions of all excited magnetization in the volume.

When the  $B_1$  pulse is removed, *relaxation* occurs with which the spins emit electromagnetic energy through two mechanisms. Longitudinal relaxation, *T1-relaxation* or *spin-lattice relaxation* is one mechanism through which the longitudinal component experiences exponential recovery ( $m_z(t + \tau) = M_0(1 - e^{-\tau/T_1}) + m_z(t)$ ) (McRobbie et al., 2003) with time constant  $T1$ . Transverse relaxation, *T2-decay* or *spin-spin dephasing* is the other relaxation mechanism with an intensity changing in time described by ( $m_{xy}(t + \tau) = m_{xy}(t)e^{-\tau/T_2}$ ) with time constant  $T2$  (McRobbie et al., 2003).

### 2.2.1.2 Spatial Encoding Gradients

In order to generate the spatial distribution information, three additional fields,  $G_x$ ,  $G_y$  and  $G_z$  are also applied with three gradient coils. These fields impose a linear variation upon the longitudinal magnetic field, changing the Larmor frequency of the spins in a spatially dependent manner. This characteristic means that gradient fields can be used to selectively excite small portions, e.g. a slice, rather than a whole volume.

### 2.2.2 MR Image Formation

As discussed previously, the application of gradient fields causes the magnetic field to vary with position. This means that we expect higher or lower precessional frequencies depending on whether the total field is increased or decreased. This leads to a Fourier relationship between the received *MR* signal and magnetization distribution (Ljunggren, 1983; Twieg, 1983).

The phase of magnetization can be calculated from the integral of gradient field amplitudes starting from time zero as:

$$\varphi(r, t) = 2\pi \int_0^t \frac{\gamma}{2\pi} G(s) \cdot r ds = 2\pi r \cdot k(t) \quad (2.2)$$

where  $k(t) \equiv \frac{\gamma}{2\pi} \int_0^t G(s) ds$

The signal equation for *MRI* acquired from the following equation is the magnetization distribution integrated over the entire volume:

$$s(t) = \int_R m(r, t) e^{-j2\pi k(t) \cdot r} dr \quad (2.3)$$

The above equation implies that the received signal at time  $t$  is the Fourier transform of object  $m(r, t)$  sampled at spatial frequency  $k(t)$ . In other words, Fourier transformation is used to convert the frequency information contained in the signal from each location in the image plane to corresponding intensity levels, which are then displayed as shades of gray in a matrix arrangement of pixels. Also, the integral of  $G(s)$  traces out a trajectory  $k(t)$  in spatial frequency space ( $k$ -space). At a high level, the acquisition method uses a sequence of gradients and the *RF* pulses which are called the *pulse sequence*. It is worth to mention that imaging speed and acquisition methods are affected by several imposed constraints. First, magnetization decays exponentially with time which limits the useful acquisition time window. Next,  $k$ -space is traversed at a speed limited by gradient system performance and physiological constraints. These are reasons behind the fact that most *MR* imaging methods use a sequence of acquisitions with which  $k$ -space and image are reconstructed from all the samples acquired from each acquisition.

In the next section, important factors which are the focuses of various developed *MR* imaging techniques are discussed. Before going through any details, let's define two important terms used in this regard in *MR* studies.

**Resolution:** is denoted by the sampled region of  $k$ -space, meaning that higher resolution is referred to a larger region of sampling,  $resolution \propto |k_{\max}|$ .

**Field of view (FOV):** is denoted by sampling density, meaning that in order to meet the Nyquist criterion, denser sampling is required for larger objects,  $FOV \propto \frac{1}{\Delta k}$ .

### 2.3 Temporal vs. Spatial Resolution

Different types of images are created by varying the sequence of *RF* pulses applied and collected. Time of echo (*TE*) is the time between the *RF* pulse delivered and the echo signal received. Also, repetition time (*TR*) is the time between successive pulse sequences applied to the same slice. An important factor which led to development of these different *MR* imaging techniques is meeting the conflicting needs of high spatial and high temporal resolution. Among various *MR* techniques, consider fast spin echo *MRI* (*T2* weighted imaging (*T2WI*)) which is produced by using longer *TE* and *TR* times. Such images for which the contrast and brightness are predominately determined by the *T2* properties of tissue are capable of high resolution visualization of structures. The more data acquired, the more spatial resolution will be achieved. However, as *MR* signal intensities decay in time, longer acquisition times required to achieve higher resolution introduce more image noise.

Those applications for which pathological changes need to be detected in early stages require complementary imaging methods to improve lesion detection and localization (Bihan et

al., 2006). For example, in pathological conditions such as strokes arising from ischemia, *T2WI* doesn't change until at least 8 hours after the onset of stroke and then appears hyper-intense in the stroke region. However, diffusion weighted imaging (*DWI*), as a complementary technique, can show the changes in brain as early as 30 mins after the onset of stroke (Allen et al., 2012; Srinivasan et al., 2006).

Diffusion means the movement of molecules in a system and follows a certain pattern based on properties and structures of tissues. This diffusion pattern will be disturbed in affected areas due to changes in pathological conditions such as acute stroke discussed above. In order to study these changes, specialized *MRI* techniques as *DWI* are used to track the diffusion pattern of water molecules to visualize internal physiology (Bihan et al., 1986; Stejskal and Tanner, 1965). *DWI* is able to generate image contrast using the diffusion property of water molecules in tissues. Such images, used as supplemental imaging scans to *T2WI* technique, aim to limit false-positive diagnosis.

However, *DWI* is not a sufficient substitution for conventional imaging due to its low resolution, noisy and blurry areas and artifacts present in the final image reconstructions. *DWI* is achieved through Echo Planar Imaging (*EPI*) gradient sequences. These enable fast image acquisition, generating *DWI* images with acquisition matrix of 128x128 and isotropic resolution limited to 2mm. For anisotropic scans, in-plane resolution of 2mm can be improved to 1mm but at lower Signal-to-Noise ratio (*SNR*). This low-resolution property is due to the limitations of *FOV* (which is directly related to the limitations of sampling density), low strength scanners. Fast acquisition techniques such as single shot *EPI* aim at acquiring images in very short time before complete signal decay and therefore have even greater limitations on maximum achievable resolution.

Since *DWI* images are used in conjunction with higher resolution scans such as *T2WI* images, the difference in the resolutions will result in over estimation of lesion area when *DWI* is super-imposed with *T2WI* and therefore higher resolution images are preferred. The artifacts and higher resolution challenges can be improved by hardware upgrading, acquisition parameter optimization or software-based post-processing techniques. Among post-processing software-based techniques are interpolation which interpolates a high-resolution voxel from various low-resolution ones. These interpolation methods, some adaptive and some non-adaptive (Lehmann et al., 1999; Thevenaz et al., 2000), have their own disadvantages such as ringing artifacts and blurring (Borman and Stevenson, 1998). Super-resolution reconstruction techniques are also among other post-processing techniques which aim at improving image quality. Unlike interpolation methods, they rely on adding information to the image to provide a high-resolution product. All aforementioned post-processing techniques directly or indirectly aim at recovering high frequency information to improve spatial resolution of low resolution *MR* applications. While promising in concept, the post-processing methods can lead to other types of artifacts or may need extra resources to acquire or estimate lost information.

So far, we have seen the Fourier relationship between data gathered in *MRI* and the reconstructed image. This necessitates reconstruction algorithms to use discrete Fourier transform (*DFT*) at some point during the processing procedure for Fourier domain transformation. We have also introduced the importance of low-resolution *MR* techniques and the resolution challenges associated with them. We have also reviewed various post-processing techniques introduced in literature which tend to enhance effective resolution while either leading to other types of artifacts or requiring extra resources. In the following section, the background on how constrained reconstruction and *DFT* reconstruction can be combined to

improve magnetic resonance imaging resolution is discussed. This section shows when limited-length data manipulation leads to destructive artifacts and provides the theoretical basis for the proposed algorithms in this thesis.

## 2.4 Basic *DFT* reconstruction introducing Gibbs' artifacts

In this section, the 2D *DFT*-based reconstruction of detailed feature of a simulated GE phantom positioned on top of a broad feature is demonstrated to illustrate how *DFT*-imposed artifacts impact 2D resolution of final *MR* images. The effect of most common solution for the elimination of artifacts, global low pass filtering, is also demonstrated on this dataset. Distortions in the image associated with *k*-space truncation can be interpreted in terms of the point spread functions (*PSF*) in 1D imaging models. Since 2D and 1D *DFT* reconstructions share characteristics, the discussions on 1D cross section of a 2D object can be extended to the 2D sense.

Fig. 2.1-A provides 512x512 high-resolution *inverse DFT (IDFT)* reconstruction of simulated GE phantom data using full *k*-space data. Fig 2.1-B is the 108x108 low resolution reconstruction of the truncated *k*-space data obtained with *IDFT*. Fig. 2.1-C is reconstructed using another *DFT*-based reconstruction (compressed sensing which will be introduced in section 2.6) from under-sampled of truncated *k*-space data also used for fig. 2.1-B. On the right side of each figure, a 1D cross section of the detailed feature is shown to help in analysing *DFT* properties. This comb feature has lost resolution after *IDFT* reconstruction (Fig. 2.1B) and residual ringing artifacts also affect parts of the image adjacent to the detailed feature which is observable in lower cross section. The application of a common approach to mitigate this effect, an apodizing filter, is shown in Fig. 2.1-D on *IDFT* reconstruction of truncated *k*-space data. This



approach destroys sufficient resolution in both cross sections and imposes blurriness and intensity loss to fine details even though the average intensity seems to look similar in both images. In other words, application of low-pass  $k$ -space filters suppress artifacts but degrade overall image quality. In the following, we provide the mathematical background to indicate when Gibbs' artifacts appear in the form of distortion in constrained  $DFT$  reconstruction. We show that relationships exist between the digital signal processing ( $DSP$ ) characteristics of high-resolution  $M \times M$  and truncated  $N \times N$  image reconstructions as an extension to (Smith et al., 2013) that make it possible to avoid introducing Gibbs artifacts into truncated  $k$ -space reconstructions.

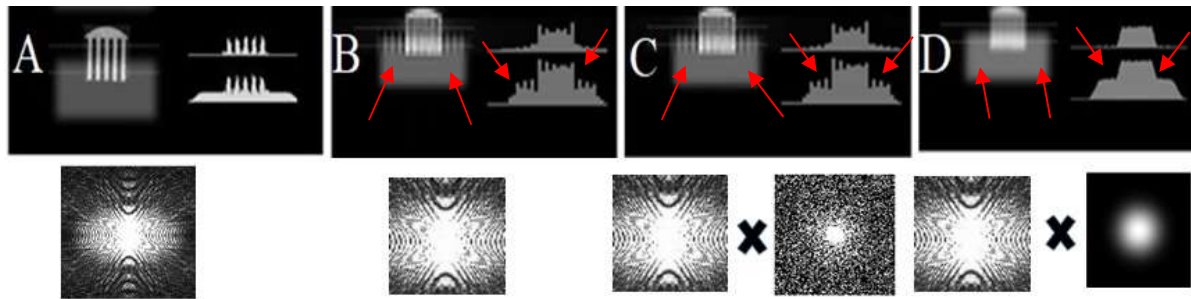


**Figure 2.1** A) 512x512  $IDFT$  reconstruction of full  $k$ -space, B) 108x1018  $IDFT$  reconstruction of truncated  $k$ -space, C) 108x108 sparse sampled reconstruction of undersampled  $k$ -space, D) 108x108  $IDFT$  reconstruction of apodized  $k$ -space, with upper and lower cross sections of tine features and tines on top of a broad feature.  $K$ -space representation of each reconstructed image is provided below each dataset. Red arrows demonstrates features mostly affected by  $DFT$ -imposed artifacts.

### 2.4.1 DSP relationship between high- resolution and low-resolution images of 1D objects

Consider an infinite continuous 1D image cross section data experimentally sampled to generate an  $M \times 1$   $k$ -space data set. The image has a pixel spacing given by  $\Delta x_M = FOV_M / M$  where  $FOV_M$  is the field of view of the  $M \times 1$  study.

The continuous 1D image cross-section  $I(x)$  arising from the inverse continuous Fourier transform (ICFT) of infinite MR  $k$ -space  $S(f)$  signal multiplied by a finite truncation window  $TW_C(f)$  is equivalent to the convolution  $I(x) = ICFT\{S(f)\} \otimes ICFT\{TW_C(f)\}$ . The image domain distortions arising from the finite window in  $k$ -space can be expressed in terms of the continuous point spread function  $PSF_C(x) = ICFT\{TW_C(f)\}$ ; (broken line, Figs. 2.2A and B).

The discrete complex valued image cross section samples can be expressed in terms of the orthonormal IDFT basis functions associated with the  $M \times 1$  sample space,  $\exp(2\pi j k_x x / M)$  as:

$$CI_M[x] = IDFT_M\{S[k_x]\} = \sum_{k_x=-M/2-1}^{M/2-1} S[k_x] \exp(2\pi j k_x x / M); \quad (2.4)$$

where  $S[k_x]$  are the sampled  $k$ -space values. Following an  $M$ -point IDFT of  $S_M[k_x]$  we have:

$$CI_M[x] = \frac{1}{M} \sum_{k_x=-M/2}^{M/2-1} S_M[k_x] \exp(2\pi j k_x x / M). \quad (2.5)$$

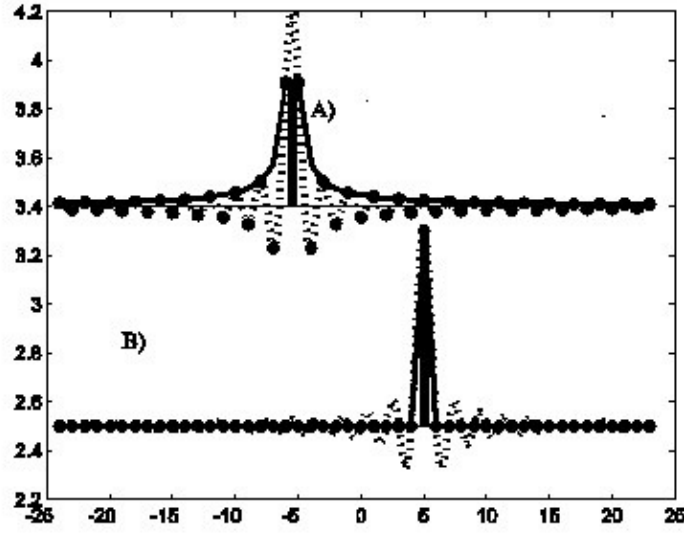


**Figure 2.2** *K*-space truncated Continuous (broken line) and discrete (solid points) point spread functions of A) and B) sampled isolated fine detail objects with different positioning characteristics in *FOV* in terms of basis function representations.

Similarly, the complex image cross section,  $CI_N[x]$ , generated from the same *k*-space data truncated to a length *N* can be expanded in terms of the orthonormal *IDFT* basis functions associated with the  $N \times N$  sample space.

$$CI_N[x] = \frac{1}{N} \sum_{k_x=-N/2}^{N/2-1} S_M[k_x] \exp(2\pi j k_x x / N). \quad (2.6)$$

where  $N = M/p$  (for an integer value *p*). For other values of *N*, the complex image cross section can be expanded in terms of sum of multiple basis functions (non-basis functions).

In Fig. 2.2, upper and lower cross sections, the broken line and solid dots respectively show the continuous,  $PSF_C(x)$ , and discrete  $PSF_N[]$  point spread functions of two point objects.

The modeled *ID* isolated objects A and B were placed with centers  $x_{B1}$  and  $x_{B2}$  which

respectively satisfy the conditions  $B1 = (2q+1)\Delta X_N / 2$  and  $B2 = (2q)\Delta X_N / 2$ ;  $0 \leq q < N$ . The

truncation window,  $TW_C(f)$ , was assigned to be rectangular and of length  $N\Delta f$  making  $PSF_C(x)$  a sinc function. Harris (Harris, 1978) indicated that the level of distortion in the spatial frequency domain increased for each signal derivative that was discontinuous across the frequency truncation boundary. For a rectangular truncation window,  $TW_C(f)$ , the distortions increase by  $3db$ , a factor of 2, for every discontinuous derivative (Harris, 1978). Point object 1 at position  $x_{B2} = x\Delta X_N$  has all boundary derivatives continuous for both real and imaginary  $k$ -space components. In contrast, point object 2 at position  $x_{B1} = x\Delta X_N + \Delta X_N / 2$  has no continuous boundary derivatives. A mathematical interpretation of cyclic continuity is that  $k$ -space representation of point object 2 can be closely approximated by a single basis function. By contrast, point object 1's  $k$ -space representation requires the sum of multiple basis functions associated with the  $N$  point  $k$ -space truncation window.

#### **2.4.2 Truncation effects on isolated high intensity object close to a smoother broad region of interest**

In this section, we discuss approaches to deliberately use the relationships between the orthonormal basis functions in the  $M \times I$  and  $N \times I$  spaces to control Gibbs' artifacts. Fig. 2.3A represents a cross section from a 1024x1024 high resolution image, specifically an isolated fine detail and a combined fine detail superimposed on a constant intensity broad feature. Identical broken lines in Figs. 2.3B and C represent the continuous point spread function of the isolated and combined objects  $k$ -space truncated to 64x64. The discrete point spread function responses demonstrated in Figs. 2.3B and C as solid dots have different effective resolution. Broad, smooth regions of interest span many samples (pixels in 2D image) and have a narrow representation in the  $M \times I$   $k$ -space that is not significantly impacted by truncation. Such features will appear

without artifacts when reconstructed from a truncated  $N \times I$   $k$ -space even when no low pass  $k$ -space filter is applied before the  $DFT$  (Fig. 2.3B and C). In contrast, the sharp, fine features near broad features will have broad  $k$ -space representations that may be considerably modified following truncation. However, we will now show that  $k$ -space modification does not necessarily mean that these features will appear surrounded by artifacts when displayed in the truncated  $N \times I$  reconstruction. This effect is shown in Fig. 2.3B and C, where both left tines are located on top of a broad feature. While no distortions and intensity loss is witnessed in B following truncation, C shows intensity loss of fine details and destructive effects of residual oscillations on broad features.

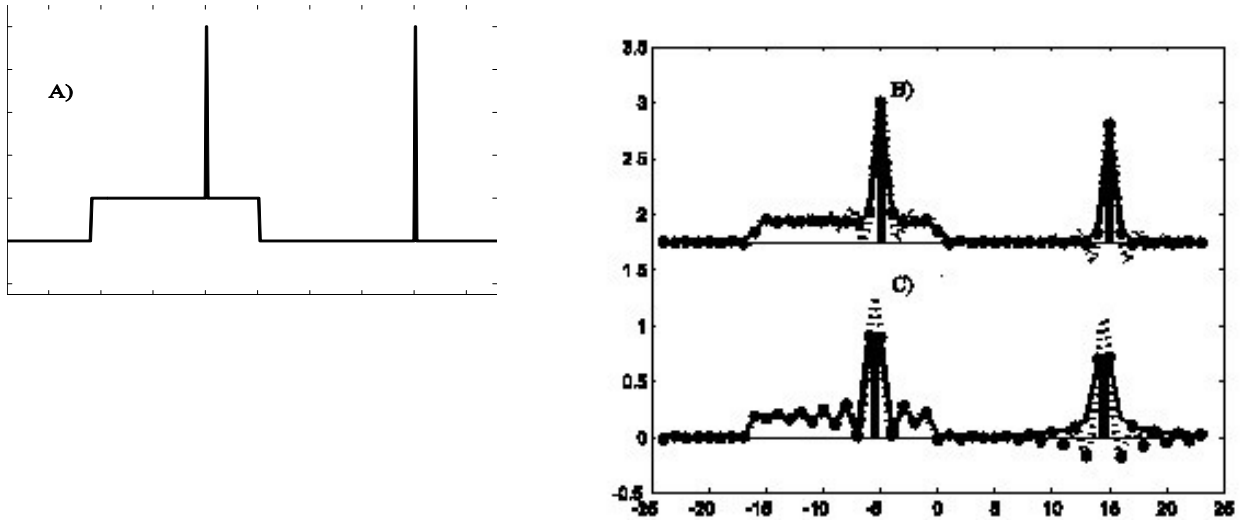


**Figure 2.3** A) 1D phantom containing one isolated narrow-width image component and a fine detail on top of a broad constant intensity image feature. The isolated narrow width peak (B) retains a higher intensity and narrower half intensity width (one with basis function representations) than the peak (C) (one with non-basis function representations) despite being sampled versions of the same continuous point spread functions (dotted line). Of particular interest is that the distortions from the discrete power spread function are enhanced when the peak with non-basis function characteristics is close to a broad feature, left side of Fig. 2C.

Consider a pixel situated at index  $x_{FD}$  in the 1D cross section  $CI_M[x]$  reconstruction. By definition, this image pixel's  $k$ -space can be expressed by a single  $IDFT$  basis function

$$S_M[k_x] = S_{FD} \exp(2\pi j k_x x_{FD} / M); \quad -M/2 \leq k_x < M/2 \quad (2.7)$$

For  $S_{FD}$ , the intensity of this pixel's  $IDFT$  basis function. If this pixel's index in  $CI_M[x]$  is  $x_{FD} = dp$ ;  $0 \leq d \leq p$ , an integer multiple of the truncation ratio  $p = M/N$ , then

$$S_M[k_x] = S_{FD} \exp(2\pi j k_x dp / M) = S_{FD} \exp(2\pi j k_x d / N); \quad (2.8)$$

which involves a single  $IDFT N \times I$  basis function. Assume this sharp isolated feature satisfied our original assumption of not being surrounded by truncation artifacts in the  $M \times I$  image cross section. Then Eqn. (2.8) indicates that this will remain a sharp isolated feature with no surrounding artifacts following truncated  $N \times I$  reconstruction (Fig. 2.3B). Any other sharp feature in the  $M \times I$  image will require a  $k$ -space representation involving a sum of multiple  $N \times I$  basis functions, i.e. the detail will become surrounded by truncation artifacts (Fig. 2.3C). A different, but equivalent, interpretation is that the presence or absence of truncation artifacts is related to the differences between how the underlying truncation point spread function, a *sinc* function, is discretely sampled for signals that do, or do not, satisfy the criterion  $x_{FD} = dp$ ;  $0 \leq d < p$ . (Smith 1993; Kellner et al., 2016).

### 2.4.3 Fourier shift manipulation to increase basis function characteristics

The distortions surrounding an individual fine detail are dependent on  $X_{SHIFT} = x_B - x\Delta X_N$ ; the difference between displayed pixel center positions,  $x\Delta X_N$ , relative to the high resolution fine detail peak intensity location,  $x_B$ . We can remove the distortions by deliberately planning the *MR FOV* placement to ensure that  $X_{SHIFT} = 0$  for some targeted fine detail of interest with a specific  $x_B$  value. In principle, this could be achieved by physically manipulating the object's position within the *FOV* (Mayer and Vrscay, 2007), or equivalently by selecting a specific *FOV* location by changing scan parameters (Tieng et al., 2011).

However, a fundamental Fourier property does provide a potential path to a more generalizable solution. The *DFTs* of impulses placed at positions  $x$  and  $x + \Delta x$  in an  $N$ -pt data sequence are respectively  $\exp(-j2\pi kx / N)$  and  $\exp(-j2\pi k(x + \Delta x) / N)$ . In this research program's context, inverting this property means that performing a pre-processing multiplication by  $\exp(+j2\pi k\Delta x / N)$  will induce a  $\Delta x$  virtual *FOV* position shift in the signal's properties. This  $k$ -space manipulation makes use of the Fourier transform (*FT*) property that multiplication by a complex sinusoid in one Fourier domain is equivalent to a position shift in the other domain. This manipulation ensures that the truncated  $M \times M$  high resolution  $k$ -space data can now be described with the minimum number of low resolution  $N \times N$  basis functions.

We are proposing new Fourier shift manipulated (*FSM*) *DFT* and sparse reconstructions where a suitable selection of  $\Delta x$  across specific *ROIs* would shift them into new *FOV* positions with higher, positionally dependent resolution.

This *FSM* approach involves uniformly re-modulating the *1D*  $k$ -space data by

$$S_{SHIFT}[k_x] = S[k_x] \exp(+j2\pi k_x X_{SHIFT} / N); \quad (2.9)$$

and 2D data by the equivalent

$$S_{SHIFT}[k_x, k_y] = S[k_x, k_y] \exp(+j2\pi k_x X_{SHIFT} / N) \exp(+j2\pi k_y Y_{SHIFT} / N); \quad (2.10)$$

Fig. 2.2B demonstrates how *FSM* helps adjusting the effective resolution of high frequency components by enforcing basis function characteristics in the local regions of *FOV*-shifted *ROI*. Similar observation is expected from fine details on top of a broad feature in Fig. 2.3B which is *FSM* representation of Fig. 2.3C, without intensity loss and residual artifacts.

In the following section, one of the common *DFT*-based reconstruction techniques, compressed sensing (*CS*) and associated *DFT*-imposed artifacts in *CS* context is discussed which is the focus of the rest of this thesis.

## 2.5 Sparse reconstruction techniques

Given the issues around overcoming problems with acquiring a sufficient amount of data (meeting spatial resolution requirements) in lowest possible scanning time, rapid *MR* imaging techniques remain a constantly evolving research area. Among those, Sparse *MRI* is one of the most recent and common techniques which enables acquisition of less data without resolution loss. In this section, sparse *MRI* techniques and resolution challenges are discussed.

Compressed sensing (*CS*) techniques were introduced first in the literature of information theory as an abstract mathematical idea. It proposes sensing of the compressed data (acquired at a sampling rate less than Nyquist sampling rate) and recovering the full samples from random, non-adaptive measurements provided that the original data has sparse representation. This



reconstruction scheme is possible if the signal or image has a specific form of sparse representation and the acquisition is incoherent with the transform (Donoho, 2006).

The necessity of high imaging speed in *MR* imaging, a relatively slow imaging modality, led to the *CS* idea emerging in *MR* applications. This idea developed rapidly during the last ten years focusing on nonlinear optimization algorithms, adaptive sparse bases and *k*-space sampling patterns to improve final *CS* image quality. Several *CS MRI* methods have been proposed, focusing on analytic or trained sparse dictionaries which are believed to have significant effect on artifact reduction. These methods aim at solving ill-posed inverse problems to acquire more robust *CS* algorithms.

A common *CS* method based on analytic sparse bases includes discrete wavelet transform (*DWT*) (Lustig et al., 2008) which is able to recover point-like and singular features from highly undersampled data. Other sparse bases include fast discrete curvelet transform (*FDCT*) (Ma, 2011) and discrete shearlet transform (*DST*) (Pejoski et al., 2015). An iterative soft thresholding optimization algorithm has also been introduced in (Hao et al., 2013; Qu et al., 2010) which takes advantage of *MR* image sparsity in sharp frequency localization Contourlet transform (*SFLCT*). Sparsity based on *SFLCT* cancels aliasing components and outperforms wavelet-based methods by successfully reconstructing curve and edges. Other methods include the combination of these transforms (Qu et al., 2010).

Dictionary learning (*DL*) has also been introduced for adaptive data fitting (Huang et al., 2014; Ravishankar et al., 2011). Patch-based adaptive sparsity or *CS* based on dictionary learning (*DL*) from image patches are believed to outperform global analytical image sparsity since patch-based dictionaries capture local image features and eliminate noise and artifacts in *CSMRI* algorithms without resolution loss. Based on such techniques, an image is decomposed into

overlapping patches to train a sparsifying dictionary and so provide higher sparsity which potentially leads to higher under sampling factors (Huang et al., 2014). Additional methods introduced in (Liu et al., 2013) combine dictionary learning and predefined sparse priors for stability under noise and reducing overfitting.

Using aforementioned sparse bases, the following references indicate the wide range of different *CS* approaches currently discussed in the literature (Haldar, 2014; Huang et al., 2014; Jiang et al., 2013; Ma et al., 2008; Qu et al., 2010). Various *CS* methods have also been proposed in literature combining different sparse bases to address shortcomings of specific analytical sparse basis including (Kim et al., 2010).

### **2.5.1 Positional dependent resolution of sparse reconstruction techniques**

In most advanced *CS MRI* techniques, it is believed that artifacts arise due to two main reasons: under sampling of *k*-space and inherent noisy images. These factors attract the most attention in recent *CS* research, overlooking the unavoidable *DFT*-imposed artifacts. This important factor is one of the main aspects of this thesis which is discussed in detail in Chapters 3 and 4. The observations discussed in section 2.4 in terms of positional dependency of resolution of *DFT* reconstructions are also demonstrated in the following in context of *CS* reconstructions.

Low resolution *CS* reconstruction of data (Fig. 2.4C, lower *ROI*) results in equivalent parts of images, as low resolution *IDFT* reconstruction (Fig. 2.4B, lower *ROI*), suffer from ringing artifacts. This observation is predictable since *CS* uses *DFT* to move constantly between Fourier domains. Positional dependent resolution is demonstrated in Fig. 2.4C for which the upper cross section is 0.4% *FOV* positional shift of lower cross section. The comb tines are recovered (represented as basis function components) and residual ringing artifacts impacting the

neighboring pixels is eliminated for both low resolution *IDFT* and *CS* (Fig. 2.4B, C). The observed positional dependency resolution in *CS* results, indicates the applicability of *FSM*, as discussed in previous section, as a potential method to improve characteristics of *CS* reconstruction procedures.

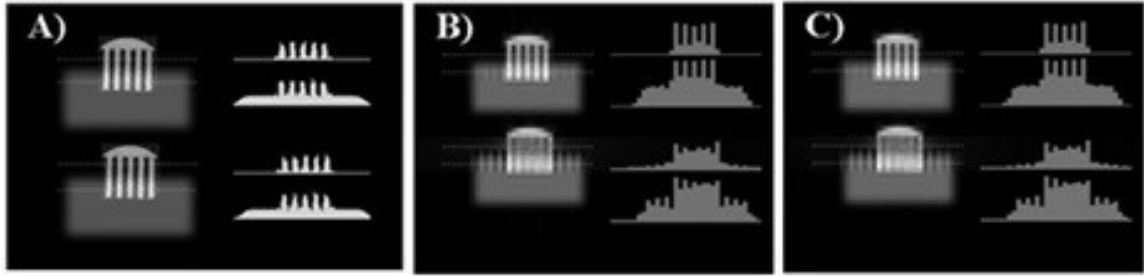


**Figure 2.4** A) 512x512 *IDFT* reconstruction of full *k*-pace, B) 108x108 *IDFT* reconstruction of truncated *k*-space, C) 108x108 *CS* reconstruction of truncated *k*-space. All Lower *ROIs* have 0.4% *FOV* position shift with respect to upper *ROIs*.

## 2.6 Validation tools in imaging applications

The choice of a reliable measurement criteria is an important factor in determining the validity of a proposed algorithm for which the final product is an image, e.g. medical imaging applications. Common objective quality metrics used for fidelity evaluation of reconstructed images include peak signal to noise ratio (*PSNR*) (Anand and Sahambi, 2008; Wiest et al., 2008), transfer edge information (*TEI*) (Xydeas and Petrovic, 2000), mean squared error (*MSE*) (Gregoria et al., 2013) and mutual information (*MI*) (Qu et al., 2002).

While they are simple to calculate, mathematically convenient (Wang et al., 2004) and independent of individual observers (Basant et al., 2013), their inference is not well-matched to perceived visual quality. This will result in unreliable conclusions on the validity of a proposed technique (Eckert and Bradley, 1998; Eskicioglu and Fisher, 1995; Girod, 1993; Teo and Heeger,

1994). This fact is shown in Fig. 2.5 in which a high-resolution *IDFT* reconstruction with and without additive noise (B, A) and low-resolution *IDFT* reconstruction of *k*-space truncation are demonstrated. Based on *MSE* values, C should be considered as a more appropriate algorithm for accurately imaging the *ROI* pointed out by red arrow. However, B in fact has higher quality in terms of visual comparison of *ROI* which is completely recovered through the other algorithm. Therefore, structural similarity comparison should be considered as an important factor for numerical metrics used as validation methods in imaging applications.

This important fact has not been neglected in literature and has resulted in modified existing quantitative metrics where errors are penalized depending on their visibility (Eckert and Bradely, 1998; Pappas and Safranek, 2000; Winkler, 1999). Some error-sensitivity approaches attempt to mimic human visual system (*HVS*) perception to determine error measures. However, the uncertainty in mapping the error visibility to the loss of quality (Silverstein and Farrell, 1996) and the effectiveness of cognitive understanding and interactive visual processing in perception of quality of images (Fuhrmann et al., 1995) has led to the proposal of more advanced qualitative metrics.

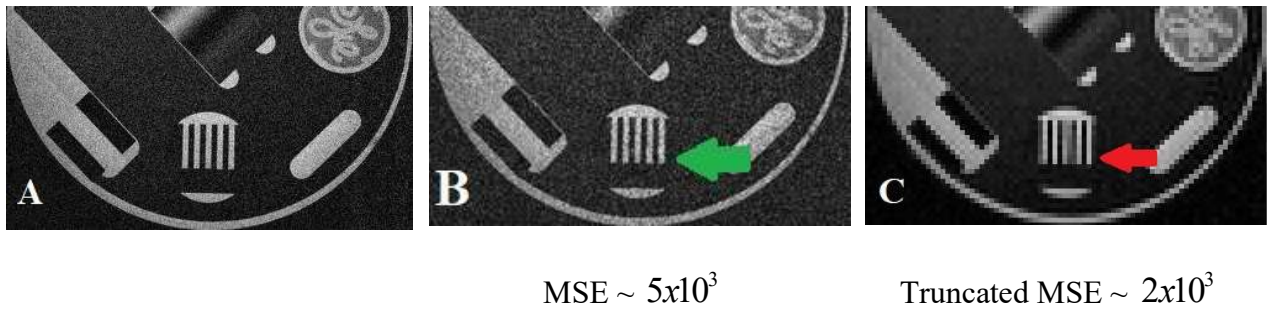


**Figure 2.5 A) High-resolution *IDFT* reconstruction of GE data, B) High-resolution *IDFT* reconstruction plus gaussian noise, C) Low-resolution *k*-space truncated *IDFT* reconstruction. The *MSE* values under B and C doesn't correctly reflect the poor structural resolution of images.**

The modified imaging algorithms in this thesis have been validated using a number of specialized metrics. The structural-similarity-based (*SSIM*) image quality assessment in section 2.6.1 and high dynamic range visual difference predictor (*HDR-VDP*) metrics in section 2.6.2 will be introduced. These visual difference metrics possess a high correlation coefficient with the mean-opinion-score (*MOS*) subjective quality metric (Basant et al., 2013).

### 2.6.1 *SSIM* metric

Based on the assumption that the human visual perception is adapted for extracting structural information from a scene, the structural-similarity-based *SSIM* metric relies on the measure of structural information change as a good approximation of perceived image distortion. The following subsections summarize the *SSIM* description by (Wang et al., 2004).

#### 2.6.1.1 *SSIM* Index

As shown in Fig. 2.6, the metric compares luminance, contrast and structure separately for similarity measurement and defines the comparison similarity measures which satisfy the following conditions:

1.  $S(x, y) = S(y, x)$
2.  $S(x, y) \leq 1$
3. 1 if and only if  $x = y$

for which  $S$  is the *SSIM* operator and  $x$  and  $y$  are reference and test images.

**Luminance:** The luminance function  $l(x, y)$  is defined as the function of the luminance of two signals (or images) which are estimated as the mean intensity of the signals (images),  $\mu$

$$\mu_x = \frac{1}{N} \sum_{i=1}^N x_i \quad (2.11)$$

$$l(x, y) = \frac{2\mu_x\mu_y + C_1}{\mu_x^2 + \mu_y^2 + C_1} \quad (2.12)$$

The inclusion of constant  $C_1$  will avoid instability when  $\mu_x^2 + \mu_y^2$  is very close to zero.  $C_1$  is defined as  $C_1 = (K_1 L)^2$  with  $L$ , dynamic range of the pixel values and  $K_1 \ll 1$ , a small constant [Wang et al., 2004].

**Contrast:** The standard deviation of luminance subtracted signals (images) is considered as the estimate of their contrast and so contrast function  $c(x, y)$  is the comparison of standard deviations  $\sigma_x$  and  $\sigma_y$

$$\sigma_x = \left( \frac{1}{N-1} \sum_{i=1}^N (x_i - \mu_x)^2 \right)^{1/2} \quad (2.13)$$

$$c(x, y) = \frac{2\sigma_x\sigma_y + C_2}{\sigma_x^2 + \sigma_y^2 + C_2} \quad (2.14)$$

where  $C_2 = (K_2 L)^2$  and  $K_2 \ll 1$  is a small constant [Wang2004].

**Structure:** the normalized signals  $\frac{x - \mu_x}{\sigma_x}$  and  $\frac{y - \mu_y}{\sigma_y}$  will be used as the inputs of the structure

comparison function,  $s(x, y)$ , as

$$s(x, y) = \frac{\sigma_{xy} + C_3}{\sigma_x \sigma_y + C_3} \quad (2.15)$$

for which,  $\sigma_{xy} = \frac{1}{N-1} \sum_{i=1}^N (x_i - \mu_x)(y_i - \mu_y)$ .

Finally, the *SSIM* index between signals  $x$  and  $y$  is defined as the combination of the three comparison functions

$$SSIM(x, y) = [l(x, y)]^\alpha \cdot [c(x, y)]^\beta \cdot [s(x, y)]^\gamma \quad (2.16)$$

where,  $\alpha > 0$ ,  $\beta > 0$  and  $\gamma > 0$ . (Wang2004) suggested to set these parameters as  $\alpha = \beta = \gamma = 1$

and  $C_3 = C_2 / 2$ .

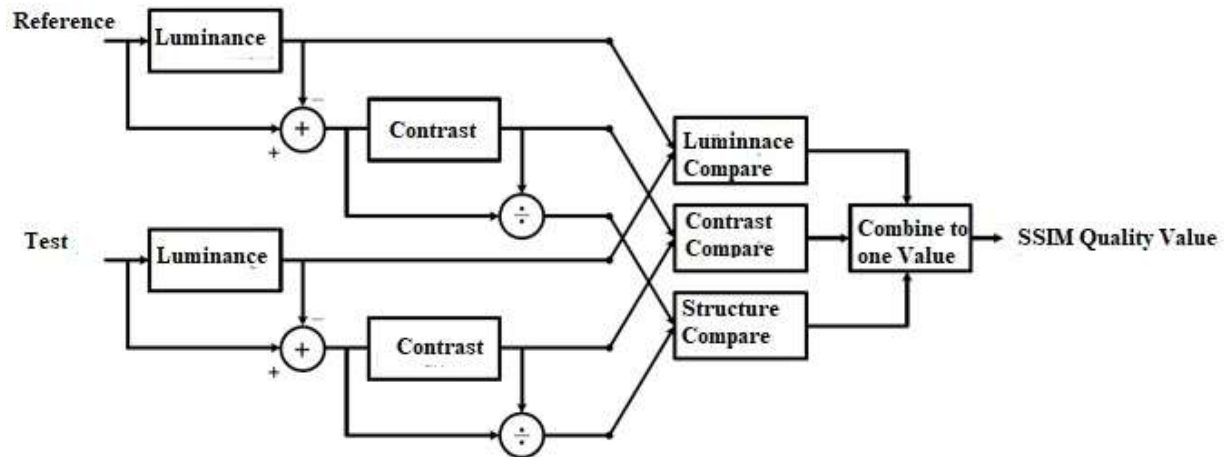


**Figure 2.6 Pipeline of *SSIM* metric modified from (©2004 IEEE) showing where and how necessary structural information are captured from test and reference images and combined into one descriptive numerical value reflecting the similarity measure.**

### 2.6.1.2 Quality Assessment Using SSIM Index

Unlike the quantitative metrics (e.g. *MSE*, *PSNR*, etc.) which are applied globally, qualitative measures such as *SSIM* are applied locally for the following reasons (Wang et al., 2004). First, the image statistical features are spatially nonstationary. Second, image distortions may also be space variant. For this purpose, the local statistics  $\mu_x, \sigma_x$  and  $\sigma_{xy}$  are computed within a local square window or a circular-symmetric Gaussian weighting window (Wang et al., 2004). Rather than the local quality measurement, the mean *SSIM* (*MSSIM*) index evaluates the overall image quality for  $M$  local windows where *SSIM* is calculated (Fig. 2.6)

$$MSSIM(x, y) = \frac{1}{M} \sum_{j=1}^M SSIM(x_j, y_j) \quad (2.17)$$

### 2.6.2 HDR-VDP-2.0 metric

This visual metric aims at prediction of visibility and quality. It is based on a new visual model for all luminance conditions and compensates for the former visual metrics introduced in (Mantiuk et al., 2011) which only work for narrow intensity ranges (Mantiuk et al., 2011). It has been shown in literature that the quality predictions of this metric are comparable or better than *MS-SSIM* (defined in 3.7) (Mantiuk et al., 2011). However, studies in (Mantiuk et al., 2011) shows that correlation between the results of these metrics with subjective *MOS* scores from two quality databases confirms that *HDR-VDP2.0* has higher correlation for both databases compared to *MS-SSIM*. However, it has not been extensively used in biomedical applications. The schematic of the metric is presented in Fig. 2.7.



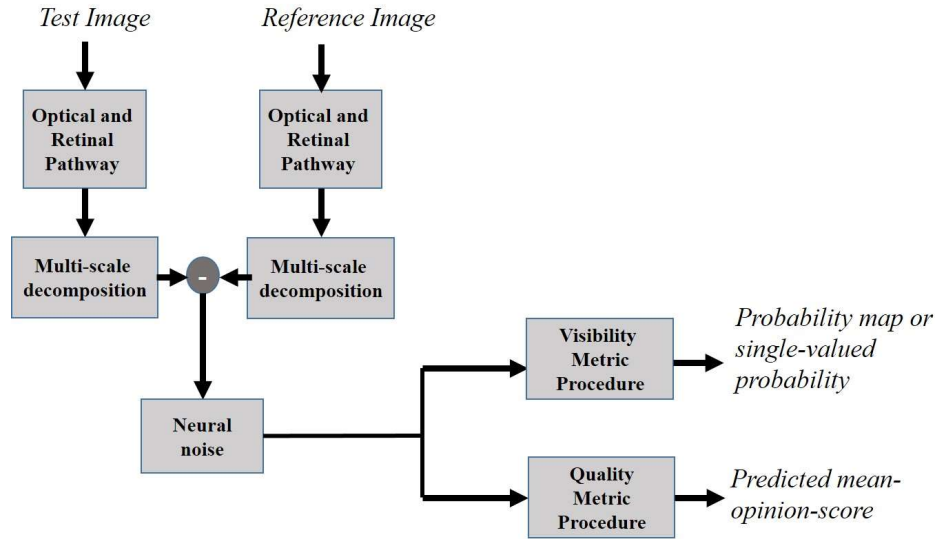


**Figure 2.7 Pipeline of *HDR-VDP2.0* metric modified from (© Maniutik et al., 2011) showing procedure of how necessary information are acquired from reference and test images and combined into a descriptive numerical value reflecting the quality of test image compared to reference.**

This algorithm is based on the comparison of the distorted and ground truth images which are inputs to the algorithm as test and reference respectively. Without going through any mathematical detail of such metric, various stages of metric's pipeline are defined. Both images will be first analyzed in “optical and retinal pathway” section which is responsible for the following processing flow:

#### ***2.6.2.1 Optical and Retinal Pathway***

The following is various stages through which test and reference images are passed simulating optical and retinal pathway of human visual system.

***Intra-ocular light scatter:*** This block models the light scattering in the cornea, inside the eye chamber and on the retina as a modulation transfer function acting on the input images. The idea

is actually modeling the scattering which attenuates the high spatial frequencies and the light pollution it results which reduces the contrast of the light projected on the retina.

***Photoreceptor spectral sensitivity:*** This block calculates the total amount of light sensed by each type of photoreceptor and the expected fraction of light sensed by each type of photoreceptors.

***Luminance masking:*** This block represents the non-linear photoreceptor response to light. The gain control of photoreceptors regulates sensitivity to the intensity of the incoming light and provides the ability to see the huge range of physical light. Only photoreceptor response for *L*-, *M*-cones and rods is modeled. The effect of *S*-cones has been omitted since they have almost no effect on the luminance perception (Mantiuk et al., 2010).

***Achromatic response:*** In this stage, the rod and cone responses are summed up to compute the joint cone and rod achromatic response. The achromatic response is then passed through the “Multi-scale decomposition” stage which mimics the decomposition happening in the visual cortex. In this algorithm, steerable pyramid is used which offers good spatial frequency and orientation separation (Wang et al., 2004).

After necessary information are acquired from test and reference images through optical and retinal pathway, the information is passed through a noise modeling stage. Due to the appropriate assumption that the differences in contrast detection comes from the several sources of noise, the sum of signal independent noise (neural *CSF*) and signal dependent noise (visual masking) needs to also be modeled.

As discussed earlier, this metric provides a visualization map to enable a local difference detection evaluation on the test image. Along with this, just like state-of-the-art quantitative metrics, it introduces a numeric value indicating the overall quality of the image decided based on the *HVS* perception.

### 2.6.2.2 *Visibility metric*

The aim of this section is to introduce a spatially varying map with each pixel representing the probability of detecting a difference. First the values are transferred from contrast units to probability values using psychometric functions (Mantiuk et al., 2011). The maximum of the local probability map, can also be used as a single value representing the probability of difference detection for the entire image.

### 2.6.2.3 *Image quality prediction*

In order to get a quick sense of an algorithm's performance, a single numerical value is preferable. Besides, the overall image quality rather than difference visibility might sometimes be the main target of image comparison. For this purpose,  $Q_{mos}$  is introduced by which  $Q$  is the output of a pooling function which pools the information from all pixels and all bands to arrive at a single value.

## 2.7 Summary of the Chapter

In this chapter, the background behind *MR* imaging applications, e.g. *fMRI* is discussed including the physics behind *MRI* techniques, data gathering in *k*-space form and the necessity of data reconstruction using *DFT*-based algorithms to move data into image space. The necessity of constrained data gathering and inevitable *DFT*-imposed artifacts are also discussed in this chapter. The theoretical background of *DFT* reconstruction properties is outlined which points out when *DFT*-imposed artifacts are destructive and how Fourier manipulation helps to eliminate those distortions without resolution loss. A brief review on common evaluation metrics in

biomedical applications specifically *MRI* is outlined in the final section and a brief introduction on two imaging metrics used to validate algorithms proposed in this thesis are also introduced.

## Chapter Three: **Proposed Methods in Compressed Sensing Algorithms (I)**

### **3.1 Introduction<sup>1</sup>**

Compressed sensing (*CS*) algorithms attempt to exploit the sparseness of magnetic resonance (*MR*) data when addressing one of the critical challenges of *MR* imaging, maintaining both temporal and spatial resolution. The nature of *CS* data manipulation first requires acquiring limited *k*-space information followed by post-processing stages to remove noise and under-sampling artifacts. *CS* reconstruction involves iteratively moving between spatial and frequency (*k*-space) domains to achieve a data regularization that generates an image approximating an *IDFT* reconstruction on a full data set.

The current *CS* literature has introduced several regularization and sparse techniques to improve *CS* results. However, these have not taken into account a key feature of *CS* methods: that there is the continual iteration of *DFT*-based techniques to move between Fourier domains. Each iteration reintroduces the common problems associated with *DFT*-based algorithms (as discussed in Chapter 2) onto a solution involved with noise and under-sampling artifact reduction. In particular, Gibbs' distortions are inherently re-introduced at each iteration, which can be expected to have a considerable impact on the final resolution of image regions of interest, *ROIs*. The impact of Gibbs' distortions during *CS* reconstruction is not well explored in the literature. It has been shown that there is an inherent filtering feature present in the regularization functions used to reduce noise-like under sampling artifacts which removes the ringing Gibbs' artifacts around a high-resolution detail (Ravishankar et al., 2011; Smith et al.,

---

<sup>1</sup>This chapter is based on the paper "Improved Compressive Sensing Resolution through Optimization of Basis Function Sparse Representation" by Paniz Adibpour, Elise Fear and Michael Smith under revision for submission to IEEE Transactions on Computational Imaging, January 2018.

2013). However, the *CS* weighting factors in existing objective functions make no attempt to directly correct the other Gibbs' distortions: associated loss of fine detail resolution and lower intensity.

The focus of this and the next Chapter is to address the *DFT* imposed artifacts present in common *CS* methods. Each chapter consists of a recently submitted manuscript which focuses on one of the common *CS* software packages. We propose complementary objective functions with the purpose of differentiating between under-sampling noise and Gibbs' distortions by proposing regularization solutions by which these artifacts will be separately addressed and eliminated. The intention is to make the proposed methods general enough to improve the reconstruction characteristics of *CS* techniques that use either adaptive or non-adaptive sparse basis concepts.

### **3.2 Overview of the concept of Improved Compressed Sensing Resolution through Optimization of Basis Function Sparse Representation <sup>2</sup>**

Compressed sensing (*CS*) reconstruction techniques attempt to utilize the sparsity of magnetic resonance images for accurate reconstruction of highly under-sampled *k*-space data. These *CS* nonlinear optimization algorithms iteratively move between image and *k*-space Fourier domains. Custom sparse transforms and optimization techniques have become the main *CS* focus to more accurately eliminate noise and under-sampling artifacts. However, the literature does not specifically explore a key feature of *CS* methods: the impact of reintroducing Gibbs' distortions when repeatedly using discrete Fourier transform (*DFT*) based techniques to move between Fourier domains. *CS* regularization will achieve suppression of the ringing components of Gibbs' artifacts around a high-resolution detail through an inherent low pass filtering operation.

---

<sup>2</sup> This is the abstract of the submitted paper and repeats material discussed in earlier chapters

However, the *CS* weighting factors in existing objective functions make no attempt to directly correct other Gibbs' distortions: the loss of fine detail resolution through lower peak intensity and increased detail width following this low-pass filtering operation. In this chapter, we propose changes to the objective function of the non-linear optimization procedure, and indicate corresponding changes to *CS* algorithm pipelines to improve the effective resolution of *CS* results in low resolution *MR* applications to recover the information lost due to Gibbs' effects. Experiments are conducted on a GE phantom and *MR* clinical data of several anatomies by applying the proposed changes as an addition to a common *CS* software package. The results confirm improvements in effective resolution of final images following independent Gibbs' correction within *CS* procedures.

### 3.3 Detailed background to <sup>3</sup>*MRI DFT* and sparse reconstructions

Magnetic resonance imaging (*MRI*) is a non-invasive imaging modality which provides high-quality visualization of anatomical structure and physiological function. A key limitation of *MRI* is meeting the conflicting needs of high spatial and high temporal resolution (Hollingworth, 2015; kim et al., 1997; Lustig et al., 2008; Uecker et al., 2010) This limitation arises from experimental and physiological constraints in sequentially acquiring the samples of the object's *k*-space. The emergence of compressed sensing (*CS*) techniques in an *MR* context revolutionized the data acquisition capability of *MR* scanners. Faster scanning times are achieved by gathering less *k*-space data (Hollingworth, 2015; Lustig et al., 2008), while using non-linear techniques in

---

<sup>3</sup> This is the introduction of the submitted paper and repeats material mentioned in earlier chapters

an attempt to achieve reconstruction of images with final resolution equivalent to full  $k$ -space reconstruction.

Resolution and intensity loss through the introduction of Gibbs' distortions around fine detail is an issue for analysis in any field where  $DFT$ -based algorithms are applied on finite length data (Harris, 1978). These distortions mean, for example, that a sharp peak in a high resolution  $IDFT$  reconstruction becomes a wider, smaller intensity peak surrounded by ringing artifacts in a lower resolution, truncated  $DFT$  reconstruction.  $CS$  is an algorithm that iteratively moves between image and  $k$ -space by repeated application of  $DFT$ -based stages. The  $CS$  regularization is designed to remove the noise-like artifacts that derive from reconstruction of under-sampled data sets (Lustig et al., 2007). This non-linear operation acts as a low pass filter operation to remove the under-sampling noise which, as a by-product, also removes the Gibbs' ringing artifact around any distorted high-resolution peak (Candes and Wakin, 2008; Smith et al., 2013). However,  $CS$  studies overlook the fact that the three Gibbs' distortions of ringing, intensity loss and widened detail width arise from a different mechanism than the noise and under-sampling artifacts. These studies frequently focus on improvement of one  $CS$  technique over another with test cases that are under-sampled versions of large high-resolution data sets where the impact of Gibbs' effects is not immediately obvious in the experimental results (Qu et al., 2010; Ravishankar et al., 2011). This means that any proposed  $CS$  improvements developed using these case studies will be less realizable in low resolution applications, e.g. functional  $MRI$  ( $fMRI$ ) studies, with different temporal resolution constraints.

In this chapter, we examine a common  $CS$  reconstruction algorithm ( $SPARSE-MRI$ , (Lustig, 2006)) whose theory and pipeline can be considered the basis of other recently developed  $CS-MRI$  techniques. We propose changes that we believe are generalizable to many advanced  $CS$



techniques regardless of the choice of sparse domain, regularization technique or  $k$ -space trajectory used. A Fourier manipulation of  $CS$   $k$ -space is investigated where the three Gibbs' distortions are correctable in either a local or global sense independently of the suppression of under-sampling noise artifacts.

This chapter is organized as follows. In section 3.4, we provide the theory of when  $DFT$  basis functions will remain sparse (i.e. Gibbs' artifact free) after  $k$ -space truncation (low resolution representation). The theory behind the investigated  $CS$  technique is also introduced in this section. In section 3.5, we will propose how to re-sparsify basis functions of frequency components by a Fourier shift manipulation ( $FSM$ ) method. Theoretical changes will be then introduced to the  $SPARSE$ - $MRI$   $CS$  algorithm taking advantage of an adaptive  $FSM$  approach using a total variation regularization technique. In section 3.6, the necessary changes to the  $CS$  algorithm pipeline to accommodate the proposed re-sparsification are introduced. The scan information of datasets and specific software settings used in this work are specified in section 3.7. In section 3.8 the results are presented for experiments conducted using the  $SPARSE$ - $MRI$  package applied on GE phantom and clinical  $MR$  data before providing a conclusion and discussing future perspectives.

### 3.4 Theory

The concepts and optimization procedures surrounding compressed sensing  $MRI$  ( $CS$ - $MRI$ ) are introduced in this session. We propose that Gibbs' ringing be re-interpreted as arising from a data truncation-induced de-sparsification of the  $MR$  data. We provide a plausibility argument to indicate why our proposed Fourier shift manipulation filter can introduce re-sparsification of the truncated data sets.

### 3.4.1 CS-MRI with analytical sparse representation

Based on the most dominant features of the image, various analytical sparse transforms have been introduced in the literature ranging from wavelets appropriate for point-like features (Kim et al., 2009) to over-complete contour-lets to recover curve-like features (Qu et al., 2010).

Regardless of the type of analytical sparse transform, CS is generally formulated as

$$\min_I \|\Psi I\|_0 \quad \text{s.t. } F_u I = y \quad (3.1)$$

In the above formulation, the vector representations of the 2D  $p$ -pixel complex image,  $I$ , and the under-sampled  $k$ -space samples measured during acquisition,  $y$ , in the complex domain,  $C$ , are respectively given by  $I \in C^p$  and  $y \in C^q (q \ll p)$ .  $\Psi$  is the global analytical sparse transform of the image. In absence of noise,  $I$  and  $y$  are related via  $y = F_u I$  for which  $F_u \in C^{pq}$  is the under sampled Fourier encoding matrix (Lustig et al., 2007).

In the presence of noise, the CS problem is formulated as a constrained optimization problem which minimizes the  $l_0$  quasi norm of the sparsified image,  $\Psi I$ . In practice, the  $l_0$  quasi norm is replaced with the  $l_1$  norm which promotes sparsity (Chen et al., 1999; Donoho, 2004), and the data consistency modified to include a noise term,  $\varepsilon \in C^m$ , scaled to the expected noise level (Lustig et al., 2007) producing

$$\min_I \|\Psi I\|_1 \quad \text{s.t. } \|F_u I - y\|_2^2 \leq \varepsilon \quad (3.2)$$

A total variation ( $TV$ ) regularization is added to the objective function to increase spatial homogeneity and improve noise reduction (Lustig et al., 2007; Tsaig and Donoho, 2006) as

$$\min_I \|\Psi I\|_1 + \lambda TV(I) \text{ s.t. } \|F_u I - y\|_2^2 \leq \varepsilon, \text{ for } \lambda > 0 \quad (3.3)$$

Adding this  $TV$  penalty, which is a measure of the sum of absolute variations in the image and minimizes the finite differences, is intended to “enforce spatial homogeneity” and improve peak-signal-to-noise ratio ( $PSNR$ ) (Lustig et al., 2007; Qu et al., 2010). A number of authors have, however, indicated that applying a  $TV$  penalty comes at the cost of resolution loss. (Ravishankar et al., 2011) indicates that the “*choice of  $TV$  weight after empirical studies on angiographic and brain images, not only removes excess noise but also eliminates Gibbs’ artifacts through an inherent filtering effect of data optimization to provide data consistency*”. This implies that adding a  $TV$  penalty to the  $CS$  objective function introduces an additional trade-off between data consistency and resolution loss in final  $CS$  images. In the context of this research, we suggest deliberately taking into account the differentiation between noise-like under sampling artifacts and Gibbs’ distortion ringing artifacts to improve resolution, and lower intensity degradation and blurriness to the high-resolution image detail. Our proposed approach avoids unnecessarily removing high frequency components responsible for resolution detail compared to application of piece-wise constant features formulated with a low frequency representation less subject to Gibbs’ distortions (e.g. Qu et al., 2010).

### 3.4.2 Basis and non-Basis function characteristics of truncated frequency components

Smith et al. (Smith et al., 2013) demonstrated that not all high-resolution image components would be subject to Gibbs' distortions following data truncation for algorithms such as direct *DFT* or *DFT*-based *CS* reconstructions. In this section, we extend the discussions in (Smith et al., 2013) and (Smith et al., 2015) and explore the relationship between the discrete signal representations of high and low-resolution data which is used to identify these components.

Consider a high-resolution  $M \times M$   $k$ -space set,  $FS[k_x, k_y]$ , where  $M \times M$  is large enough that the complex-valued image,  $I_{M \times M}[x, y]$  shows no Gibbs distortions. The discrete form of the sampled *IDFT* reconstruction of  $FS[k_x, k_y]$  can be expressed as

$$I_{M \times M}[x, y] = IDFT_{M \times M}\{FS[k_x, k_y]\} = \sum_{k_x=-M/2}^{M/2-1} \sum_{k_y=-M/2}^{M/2-1} FS[k_x, k_y] \exp(2\pi j k_x x / M) \exp(2\pi j k_y y / M); \quad (3.4)$$

where  $\exp(2\pi j k_x x / M)$  and  $\exp(2\pi j k_y y / M)$  are the orthonormal *IDFT* basis functions.

Following an  $M$ -point *IDFT* along the  $y$ -direction of  $FS[k_x, k_y]$  to obtain  $FSR_{M \times M}[k_x, y]$ , for the  $y^{th}$  image row we have:

$$I_{M \times M}[x, y] = \frac{1}{M} \sum_{k_x=-M/2}^{M/2-1} FSR_{M \times M}[k_x, y] \exp(2\pi j k_x x / M). \quad (3.5)$$

Similarly, the  $y^{th}$  row of the complex image,  $I_{NxN}[x, y]$ , generated from the same  $k$ -space data truncated to a length  $N$  can be expanded in terms of the orthonormal *IDFT* basis functions associated with the new truncated  $N \times N$  sample space.

$$I_{NxN}[x, y] = \frac{1}{N} \sum_{k_x=-N/2}^{N/2-1} FSR_{MxM}[k_x, y] \exp(2\pi j k_x x / N). \quad (3.6)$$

A pixel associated with a high-resolution image detail situated at position  $x_{FD}$  is represented by a single *IDFT* basis function in the high-resolution  $M \times M$  space

$$FSR_{MxM}[k_x, y] = FSR_{FD} \exp(2\pi j k_x x_{FD} / M); \quad -M/2 \leq k_x \leq M/2 - 1 \quad (3.7)$$

If the pixel position satisfies  $x_{FD} = dT_R$ ;  $0 \leq d < T_R$ , where  $T_R = M / N$  is the truncation ratio, then this high-resolution pixel is also represented by a single *IDFT* basis function in the truncated, low resolution  $N \times N$  space

$$FSR_{MxM}[k_x, y] = FSR_{FD} \exp(2\pi j k_x dT_R / M) = FSR_{FD} \exp(2\pi j k_x d / N); \quad (3.8)$$

This implies that this pixel will appear without Gibbs distortions in a truncated reconstruction. A pixel at any other high-resolution image location will require a  $k$ -space representation involving a sum of multiple  $N \times N$  basis functions (Harris, 1978), i.e. the detail will become surrounded by truncation artifacts and suffer intensity loss and increased peak width.

### 3.5 Proposed Alternative *CS-MRI* Formulation

The fact that high resolution pixels not satisfying the position criterion,  $x_{FD} = dT_R; 0 \leq d < T_R$  exhibit Gibbs' distortions after truncation can be re-interpreted as implying that Gibbs' distortions are the result of a position-dependent de-sparsification of image components imposed by the data truncation operation. In the next sections, we propose the foundation for a framework by which these components can be re-sparsified, and show that this concept can be expressed as a complementary objective function fitted into *CS* theory.

#### 3.5.1 Re-sparsification of basis function representation of finite length Frequency Components

Lustig et al. (Lustig et al., 2007) provided a plausibility argument to explain the *CS* recovery scheme. This recursive thresholding technique starts with detection of the highest peak through amplitude thresholding followed by the calculation of interference caused from that peak. Image quality is improved by the subtraction of this interference, and the same procedure is recursively used to improve the characteristics of the weaker peaks. We follow a similar argument to explain how re-sparsification can be used to recover the main peak intensity and remove side lobes during data truncation independently of the suppression of under-sampling noise.

Fig. 3.1 shows various different reconstruction approaches applied to a 512-point high resolution 1D signal containing two signal patches. The first patch has fine detail peaks at location 131 / 512 and 147 / 512, the second has peaks at 320 / 512 and 354 / 512, described using relative field of view (*FOV*) positions,  $0 \leq posn < 1.0$ , within the data set. Thresholding will recover four peaks above the threshold line in the fully sampled high resolution signal, Fig. 3.1A. Under-sampling introduces noise-like artifacts, but we can expect to successfully recover the

sharp peaks on the under-sampled high-resolution data set by thresholding out this noise, Fig. 3.1B with a standard sparse algorithm.

Fig. 3.1C shows the impact of four-fold data truncation on the fully-sampled data patches. The actual right signal patch peaks are now located at relative *FOV* positions  $76 / 128$  and  $78 / 128$  with integer numerator values. By comparison, the actual left-hand peaks are now located at relative *FOV* positions with non-integer numerators,  $30.25 / 128$  and  $34.25 / 128$ .

Peaks with a relative *FOV* position having integer numerator values, can be represented by a single *k*-space basis function in the new truncated 128 *DFT* space. Thresholding will recover the true intensity of these peaks as they are minimally impacted by Gibbs' distortions following truncation. However, multiple *k*-space basis functions in the new truncated 128 *DFT* space must be used to represent peaks whose relative *FOV* positions are described with non-integer numerator values. The need to use multiple basis functions is an alternative expression of the introduction of the three Gibbs' distortions.

The Gibbs' distortions (blurriness, increased peak width, and loss of intensity) present in the left signal patch will remain following under-sampling, Fig. 3.1D. They will be untouched when sparse reconstruction thresholding removes both the under-sampling noise like artifacts and the Gibbs' distortion ringing artifacts.

We propose to introduce re-sparsification of the Fig. 3.1-C truncated reconstruction by taking advantage of a Fourier shift modulation (*FSM*) property that multiplication by a complex exponential,  $W(X_{Sh} / N) = \exp(2\pi j k_x X_{Sh} / N)$  in the  $N \times N$  *k*-space domain will introduce a relative shift,  $X_{Sh} / N$ , in the position of components in the  $N \times N$  image domain [Smith et al., 2015]. Selecting  $-1/2 \leq X_S < 1/2$  will cause a frequency up-shift operation sufficient to

introduce a position shift in the range  $-1/2\Delta X \leq \Delta posn < 1/2\Delta X$ , where  $\Delta X$  is the image resolution. Fig. 3.1E shows the re-sparsification of Fig. 3.1C following a left-patch *ROI* specific  $k$ -space multiplication by  $W(-0.25/128)$ , which causes the left patch peak characteristics to become describable by basis functions with no Gibbs' distortions present. Fig 3.1F demonstrates that the *FSM* re-sparsification is transitive with the under-sampling operation.

Specifically targeting the characteristics of the Gibbs' distortions imposes restrictions upon how the *TV* measure is evaluated. Calculating *TV* from the magnitude image, e.g.

$$TV_{MAG} = \sum_{IMAGE} abs(|I(x+1, y)| - |I(x, y)|) \text{ is inappropriate. This calculation incorrectly}$$

calculates a lower *TV* measure for the Gibbs' distorted left patch (Fig. 3.1C) than for the re-sparsified, non-Gibbs' distorted, Fig. 3.1E whenever the fine detail is superimposed upon a background intensity smaller than approximately 10% of the peak height. This introduces an error similar to that introduced if *MRI* signal-to-noise ratios are calculated under similar circumstances (Henkleman, 1985; McGibney et al., 1993). An image wide global *TV*,

$$TV_{GLOBAL} = \sum_{TV} abs(I(x+1, y) - I(x, y)), \text{ calculated from the complex image would also be invalid}$$

as the re-sparsification operation applied to the left-hand peaks in Fig. 3.1C has de-sparsified the right patch peaks increasing the global *TV*.



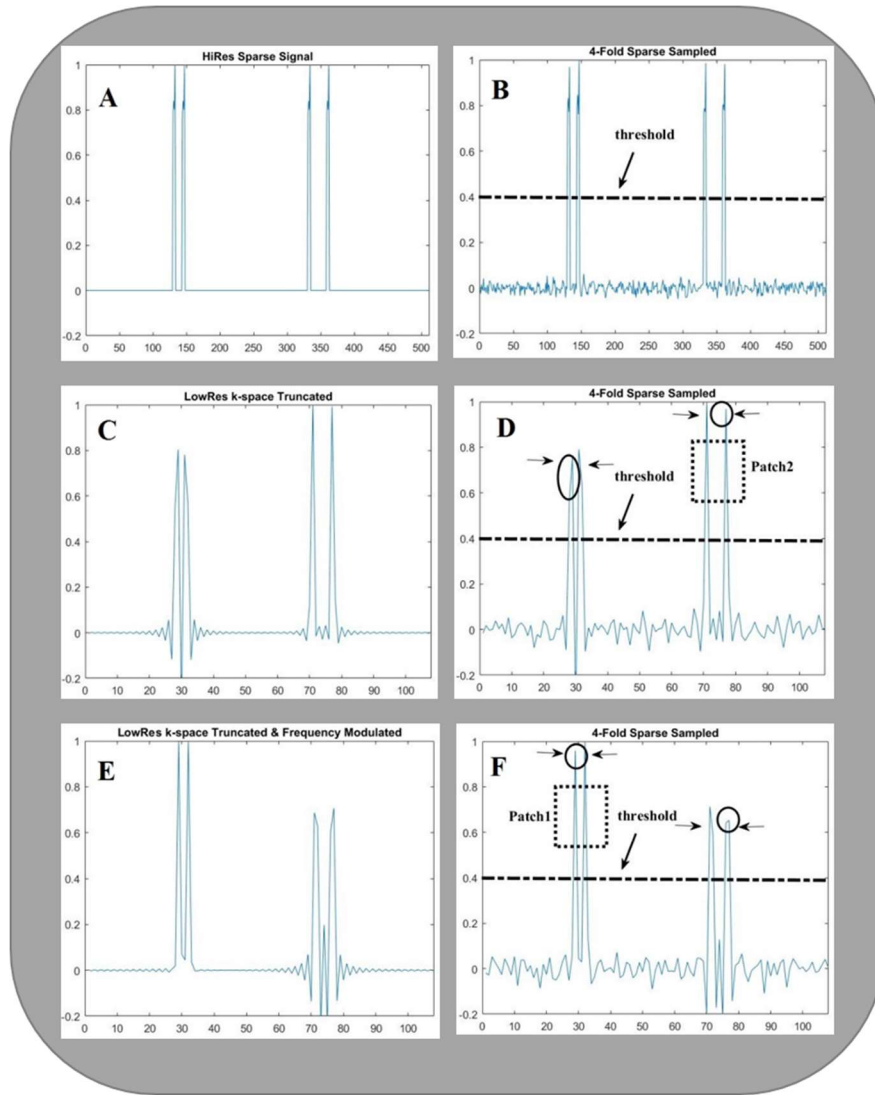


**Figure 3.1** Sparse signal reconstruction of (A) 512-length high resolution signal, from (B) pseudo-random  $k$ -space under sampling by thresholding technique. (C) Following  $k$ -space data truncation, Gibbs distortions are introduced into the left patch signal peaks. (D) The true intensity and peak width will not be recovered from the under-sampled truncated data set using a thresholding technique. Applying a frequency upshift multiplication technique to shift the left patch peak positions by 0.25 of the pixel resolution recovers the true left patch peak intensity and width in both (E) the fully sampled and (F) under-sampled data sets.

We propose a local  $TV$  calculated across specific  $ROIs$ ,

$$TV_{ROI} = \sum_{ROI} abs(I(x+1, y) - I(x, y)) .$$

This approach differs from that taken of the independent work Kellner et al (Kellner et al., 2016) who evaluated point-by-point  $TV$  measures to suppress truncation artifacts in the context of standard truncated  $DFT$  reconstructions rather than sparse reconstructions. The Kellner approach treats every image pixel as if it was impacted by truncation artifacts, resulting in a more intense image smoothing, i.e. loss of fine detail across the  $ROI$ . Our proposed regionally-applied  $TV$  measures are applicable to both  $DFT$  and  $CS$  reconstructions.

### 3.5.2 Alternative $CS$ -MRI with Analytical Sparse Representation

The aim of the following sections is to formulate the  $CS$ -MRI problem in a form which improves both de-noising and spatial homogeneity properties of  $CS$  result while preserving or improving the effective resolution, local contrast-to-noise ratio, of  $CS$  image through adaptive re-sparsification of high resolution details. Eqn. 3.3 is the  $SPARSE$ -MRI formulation which represents sparsity in both analytical sparse transform and finite differences. A more flexible choice of  $TV$  weight helps to remove much of the noise while not enforcing spatial homogeneity as strong as the  $SPARSE$ -MRI protocol. With this approach, the Gibbs' artifacts originally smoothed out through  $TV$  regularization will be present and the  $IDFT$  basis functions become non-sparse. The proposed  $CS$ -MRI formulation of Eqn. 3.9 and 3.10 together provide a  $CS$  reconstruction which balances the conflicting needs of noise reduction and spatial homogeneity. Gibbs' artifacts will be independently eliminated from the  $CS$  result by solving a new objective

problem (Eqn. 3.10) which enforces a row-based Gibbs' removal by optimizing the frequency upshifting factor which results in minimum  $TV$  among the various Fourier shift modulated data.

$$\min_x \| \Psi I \|_1 + \beta TV(I) \text{ s.t. } \| F_u I - y \|_2^2 \leq \varepsilon, \text{ for } \lambda > \beta > 0 \quad (3.9)$$

$$\min_{x_{sh_1}, \dots, x_{sh_N}} \lambda TV(RS_{x_{sh_i}}(I)) \text{ s.t. } -1/2 \leq x_{sh_1}, \dots, x_{sh_N} \leq 1/2, \quad (3.10A)$$

$$\text{where } RS_{x_{sh_i}}(I) = IDFT(S(k).W(k, x_{sh_i})) \quad (3.10B)$$

and

$$W(k, x_{sh_i}) = \begin{bmatrix} \exp(2\pi j(-N/2)x_{sh_i}\Delta k) & \dots & \exp(2\pi j(N/2-1)x_{sh_i}\Delta k) \\ \dots & \dots & \dots \\ \exp(2\pi j(-N/2)x_{sh_N}\Delta k) & \dots & \exp(2\pi j(N/2-1)x_{sh_N}\Delta k) \end{bmatrix} \quad (3.10C)$$

Eqs. 3.10 (A) – (C) form a complementary  $TV$  regularization of the re-sparsification matrix ( $RS_{x_{sh_i}}(I)$ ) of  $CS$  image (signal) acquired from the  $CS$  optimization formula in Eqn. (3.9).

$W(k, x_{sh_i})$  is the frequency shift modulation matrix which applies frequency upshifting through the operation  $S(k).W(k, x_{sh_i})$  containing distinguished shift factors ( $x_{sh_1}, \dots, x_{sh_N}$ ) for each row of the image  $k$ -space ( $S(k)$ ) which needs to be optimized within Eqn. 3.10. Using this technique, we will minimize the trade-off between data consistency and noise reduction by differentiating important types of artifacts and proposing distinct approaches for elimination of each artifact.

### 3.6 Method

The current  $CS$  algorithm pipeline is shown schematically in Fig. 3.2A. In this chapter, we illustrate the two proposed uses of the Fourier shift manipulation ( $FSM$ ) approach as an

independent optimization algorithm designed to be inserted into the existing *CS* algorithm pipeline, see Figs. 3.2A and 3.2B.

### 3.6.1 Gibbs' Correction using *FSM* Estimation from initial preparatory scans

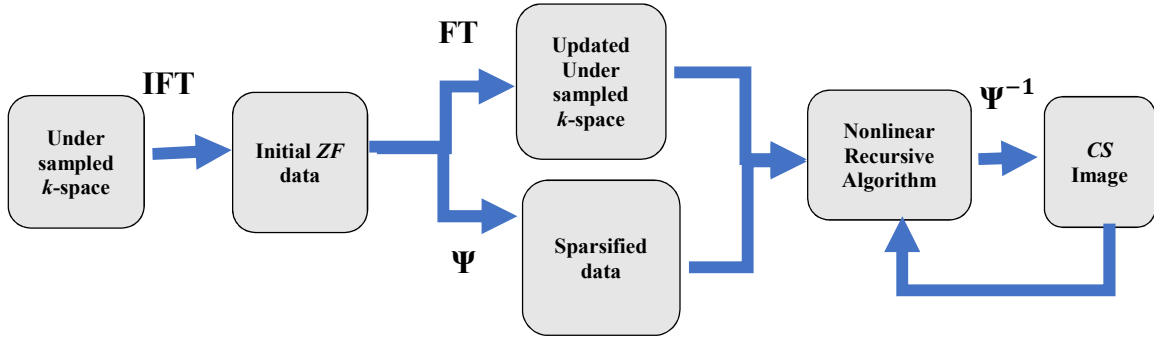
In low resolution applications, e.g. *fMRI* studies, an initial reference scan is acquired to calibrate the system and adjust the field of view for further acquisition of time series scans. In addition, information from the initial scan can be used as *a priori* information to support further analysis (e.g. Ravishankar et al., 2011). In Fig. 3.2B we propose a modified *CS* pipeline where estimates for the *FSM* resolution enhancement are used to correct the zero-filled sparse data before it is processed by a sparse algorithm.

One approach for generating the *FSM* estimates is to directly determine the high-resolution relative *FOV* position of any sharp detail near desired *ROI* likely to generate the three Gibbs distortion. A corrective *FSM*  $\Delta x$  can then be proposed if the relative *FOV* position does not satisfy the x-position criterion,  $x_{FD} = dT_R; 0 \leq d < T_R$  or the corresponding y-position criteria. Alternatively, a truncated reconstruction of the preliminary scan can be generated, and *TV* measures used to identify *ROIs* impacted by Gibbs artifacts.

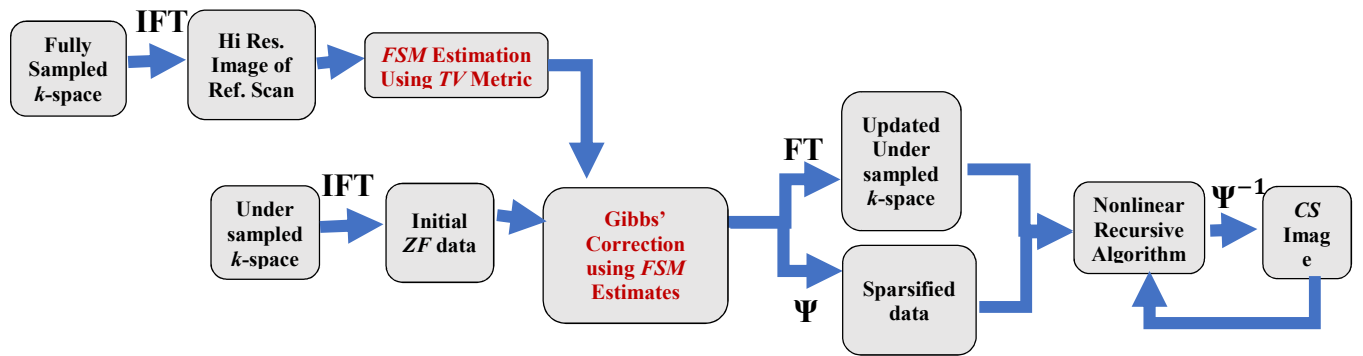
The following steps introduce the order of procedure taken in the first proposed method:

- Acquire several *FSM* estimates of the sparse-sampled *k*-space
- Apply *CS* algorithm on each set of *FSM* processed *k*-space
- Determine the optimized *FSM* estimates using *TV* measure (this can be done in a row-by-row, column-by-column or with the focus on a local *ROI*)
- Select the *CS* results of *FSM* estimate which has been identified as the optimal one when investigating the initial scan (this can be one *FSM* estimate focusing on one region of *ROI* or combination of optimal *FSM* estimates for rows or columns of dataset)
- In cases where multiple *FSM* estimates are acquired, registration of final image is required to re-adjust the sampling positions due to phase ramping of dataset in step 1

A) *Common CS Scheme*



B) *Modification 1*



C) *Modification 2*

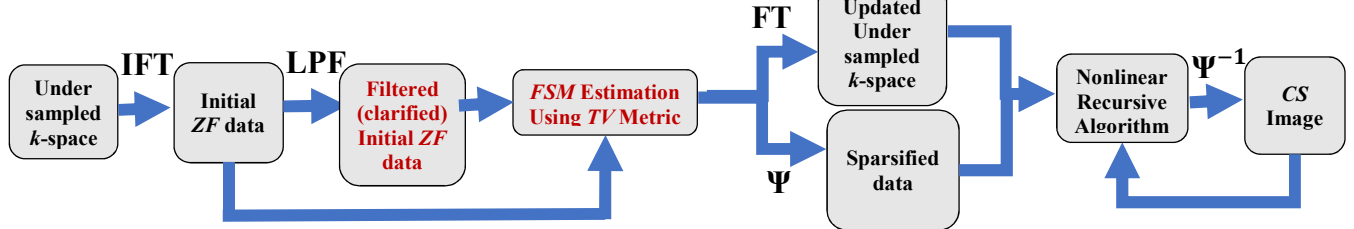


Figure 3.2 A) The existing CS pipeline can be modified to remove Gibbs' artifacts independently of under-sampling noise using *FSM* estimates derived from B) a preparatory full *k*-space scan or C) estimates derived from a zero-filled under-sampled data set.

### 3.6.2 Gibbs' correction using *FSM* estimation from zero-filled under-sampled data

In order to implement the first proposed pipeline, Fig. 3.2B, an initial reference scan is needed to perform reliable *FSM* estimation. The aim of the second proposed pipeline, Fig. 3.2C is to provide a potential framework by which independent Gibbs' correction is possible. This approach may result in lower accuracy compared to the first pipeline and yet higher accuracy compared to the original *CS* pipeline without the necessity of acquiring preliminary information from initial reference scan or the use of full, non-sparse, truncated scans. To achieve this, *FSM* estimates should be acquired prior to the first time a *DFT*-stage is employed to process the sparse sampled data. Later determination is inappropriate as the iterative *CS* reconstruction have already corrupted the *TV* information needed to identify the necessary *FSM* correction, and this corruption will propagate further through the algorithm.

Fig. 3.2C shows this *CS* pipeline modification where *FSM* estimates are acquired from an initial *IDFT* of the zero-filled (*ZF*) under-sampled *k*-space data. Our empirical studies show that *FSM* estimates of acquired sparse sampled data are not as interpretable as *FSM* estimates acquired from fully-sampled *k*-space data since noise-like under sampling artifacts are also changing the intensity of pixels in addition to *DFT* artifacts, e.g. Gibbs' distortions. On the other hand, *FSM* estimates of *CS* reconstructed data are not interpretable since the regularization procedure filters data and will have already smoothed out ringing. Therefore, in the second modification shown schematically in Fig. 3.2C, we propose to acquire the *FSM* estimates from the initial *ZF* data before any optional inherent *CS* low pass filtering removes fundamentally useful information for the reliable *FSM* estimates. But, in order to improve the accuracy of *FSM* estimates, we propose to improve *SNR* of zero-filled data and fade the effect of noise-like under-sampling artifacts while keeping the effect of *DFT* artifacts. We then perform *FSM* estimation on

pre-filtered *ZF* data. It has been pointed out frequently in several *CS* studies (Lustig2007, Doneva2010) that random under-sampling schemes yield noise-like under-sampling artifacts with characteristics similar to Gaussian noise. Therefore, to boost the *SNR* of *ZF* data, the Wiener filter is used in the model to improve the accuracy of *FSM* estimates. The filter parameters are deliberately adjusted to decrease the background noise while preserving most of the destroying effects of Gibbs' artifacts. Upon acquiring *FSM* estimates from filtered *ZF* data, the information is used to correct Gibbs' effects from *ZF* data. This method will certainly remove part of Gibbs' distortions from *ZF* data when improving *SNR* of undersampled data, which will also certainly decrease the accuracy of *FSM* estimates in the next step of the algorithm. However, the empirical studies show that the cost of accuracy loss for the algorithm is less than the temporal resolution cost of the first *CS* alternative. This means that most of the corrupted features in the *ROI* after regular *CS* reconstruction are still recovered which suggests the reliability of the proposed algorithm.

### **3.6.3 Quantitative metrics to compare standard and *FSM* supported *CS* reconstructions**

An important factor when comparing clinical results acquired from different algorithms is that diagnosis is performed by radiologists or human specialist. While direct comparisons of different algorithm results using least square error measures relative to a standard image are useful, we propose the use of three metrics which focus on the structural similarity, or lack of it, between images as perceived by human vision. The high-frequency error norm (*HFEN*) quantifies the quality of reconstruction of edges and fine features (Ravishankar et al., 2011). The structural similarity index map (*SSIM*) represents a comparison map for luminance, contrast and structure with each pixel intensity quantifying the level of similarity between gold standard and the test

image (Wang et al., 2004). It also represents a numerical value for each of the aforementioned image visual properties<sup>4</sup>

### 3.6.4 CS software and dataset materials

The protocol associated with *SPARSE-MRI* software [Lustig, 2006] is kept unchanged. The  $k$ -space under-sampling pattern included 10% full sampled central core and variable density random sampling pattern of periphery of  $k$ -space. *SPARSE-MRI* wavelet reconstruction approach was used in all simulations. The *MRI* experimental  $512 \times 512$  raw  $k$ -space data set from a GE phantom presented in Fig. 3.3 was provided by Dr. MacDonald, University of Calgary, Canada, and was obtained using a fast gradient recalled echo sequence with  $FOV_M$  of  $18\text{ cm} \times 18\text{ cm}$ . *CS* reconstruction involved 21% of a  $108 \times 108$  truncation of an original high resolution  $512 \times 512$  sampling. The truncation length was deliberately chosen to enhance potential distortions in the GE phantom. Figure 3.4 is a slice of a 3D multi-slab, magnetic resonance renal angiography study from anonymized data provided by Dr. Chen, Rotman Research Institute, Canada and Dr. Lebel, GE (Calgary), Canada. *CS* reconstructions made use of a 33% sparse sampled truncated  $128 \times 128$  subset from an initial  $384 \times 384$  high resolution data set.

## 3.7 Results and Discussion

In this section, we report on how the approaches to adding *FSM* support affects the quality of *ROIs* in images before comparing the performance of the standard *SPARSE-MRI* and modified *CS* pipelines using the *HFEN*, and *SSIM* which simulate the human perception of image quality.

---

<sup>4</sup> These metrics were described in detail in Chapter 2



### 3.7.1 Experimental Results

Figs. 3.3 and 3.4 respectively show the results from the current and proposed modifications of the *SPARSE-MRI* pipeline used for GE phantom and clinical reconstructions. For each Fig., A) shows the original image and B) the standard *SPARSE-MRI CS* reconstruction. Figs. C) and D) respectively show *FSM* supported *SPARSE-MRI CS* reconstructions supported by estimates from the initial scan, pipeline Fig. 3.2B, and from the zero-filled data, pipeline Fig. 3.2C.

In Fig. 3.3B, the standard *SPARSE-MRI CS* generates blurred tines (solid arrows) and there is evidence of residual artifacts (dotted arrows) around the comb feature. There is full recovery of comb feature (Fig 3.3C, solid arrows) and the complete elimination of Gibbs oscillations surrounding high frequency components (dotted arrows) for the *FSM* supported *CS* reconstruction using *TV* optimization of *FSM* estimates from the *IDFT* of the initial scan. The results from *FSM* supported *CS* reconstruction using *TV* optimization of *FSM* estimates from zero-filled data with improved *SNR* shows complete elimination of the Gibbs ringing (Fig. 3.3D, dotted arrows) and a superior recovery of the tines within the comb feature (solid arrows).

The zoomed version of Fig. 3.4 provides better insight into structural differences following the application of the proposed *TV* optimization of *FSM* estimations. The results from both proposed pipelines (Fig. 3.3 C and D) provide images which are less blurry and the specific *ROIs* have recovered effective resolution (solid white arrows). Using *FSM* estimation from a preliminary reference scan provides the opportunity to more accurately reconstruct structural details of fine objects. Unlike that, the results of pipeline using *FSM* estimations of *SNR*-boosted zero-filled data demonstrates less accuracy in recovery of structural details.

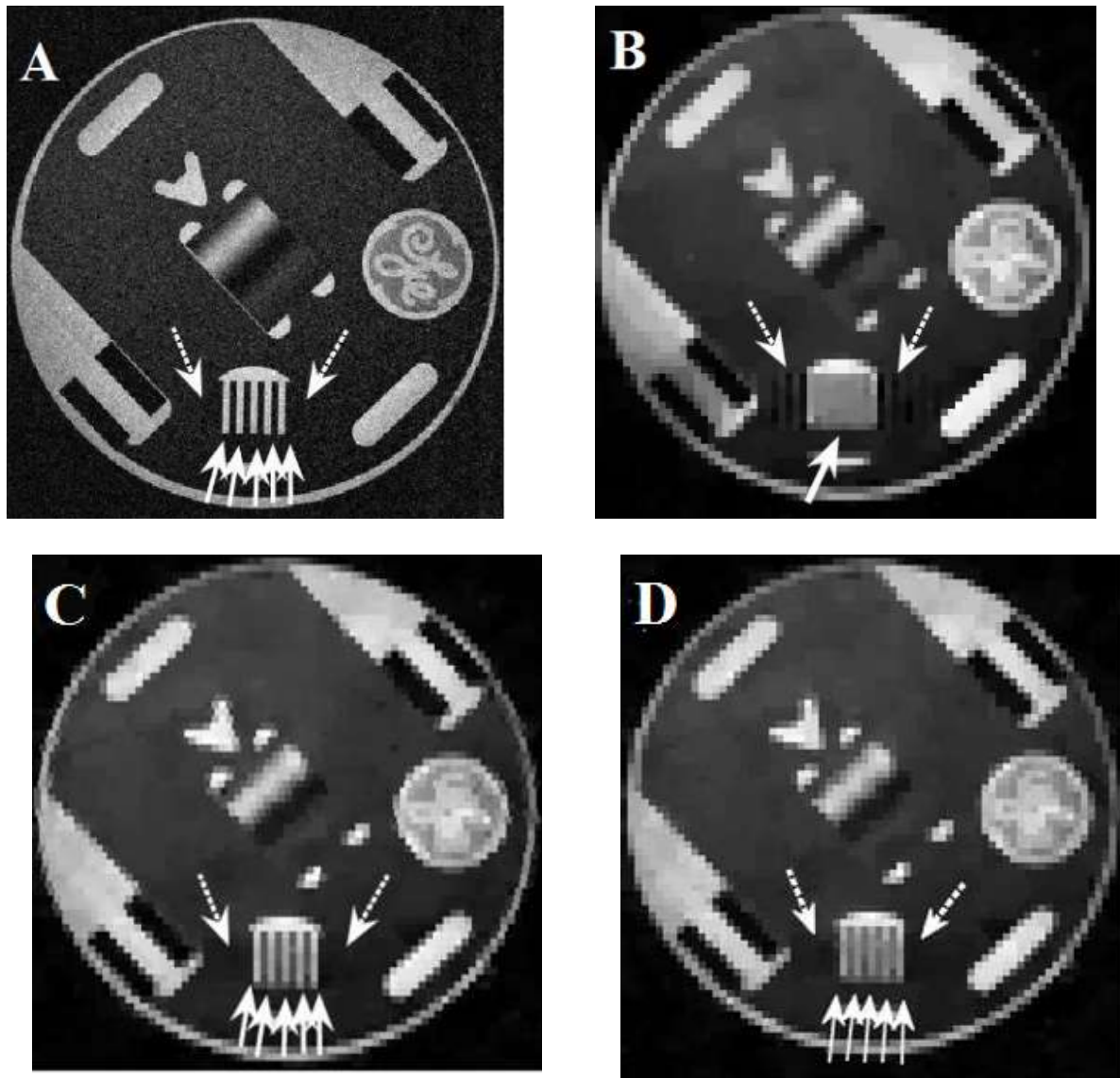
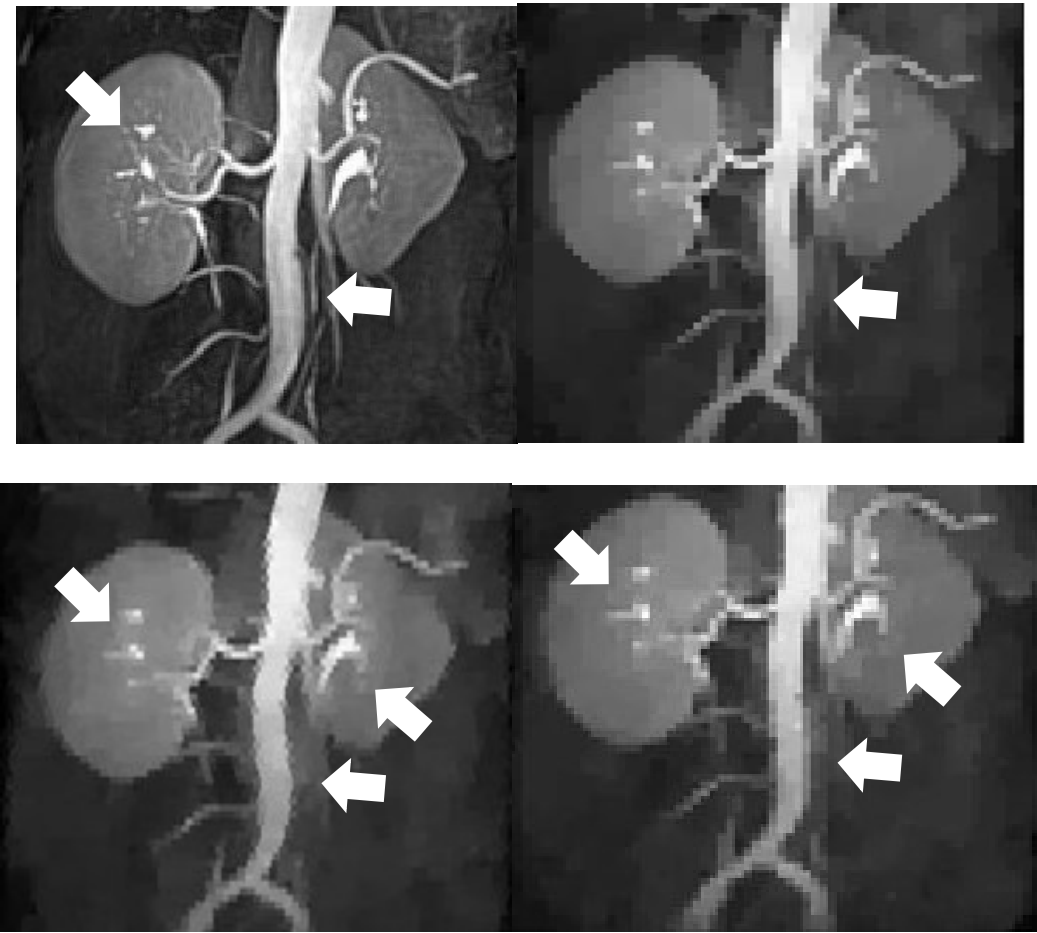


Figure 3.3 A) The high resolution *DFT* reconstruction from a  $512 \times 512$  GE data set are compared to B) a standard *SPARSE-MRI CS* reconstruction, and *FSM* supported reconstructions using *FSM* estimates from C) the preliminary scan and D) low-pass filtered zero-filled sparse sampled data.



**Figure 3.4** Zoomed portion of A) The high resolution *DFT* reconstruction from a  $384 \times 384$  renal study GE data set are compared to B) a standard *SPARSE-MRI CS* reconstruction, and *FSM* supported reconstructions using *FSM* estimates from C) the preliminary scan and D) low-pass filtered zero-filled sparse sampled data.

### 3.7.2 Performance measure of the proposed techniques

To compare performance with common *SPARSE-MRI* software results, the numerical metrics are calculated for results acquired from proposed algorithms and the gold standard, Fig. 3.3A and 3.4A. Fig. 3.5 provides numerical metrics calculated for simulated GE data demonstrated in Fig. 3.3 and Fig. 3.6 provides results of similar metrics for the experimental renal data demonstrated

in Fig. 3.4. The consistency of results is examined for various sparse sampling rates and each graph represents results of the metric versus various sampling rates for three algorithms, original *SPARSE-MRI* with blue line, proposed optimized *SPARSE-MRI* using *FSM* estimations of preliminary reference scan with yellow line and proposed optimized *SPARSE-MRI* using *FSM* estimations of *SNR*-boosted *ZF* data with red line.

The *HFEN* metric versus various sampling rates, Fig. 3.5A, quantifies the quality of reconstruction of edges and fine features (Ravishankar et al., 2011). *HFEN* shows the highest performance (smallest error, yellow line) for the proposed pipeline modification where *FSM* estimates are generated from the preliminary full-scan. *HFEN* metrics are lower when *FSM* estimates are derived from the *ZF IDFT* reconstruction (red line) but still outperforms the standard *CS* reconstruction. This result is predictable based on discussions we had on image results in previous section. The *SSIM* comparisons of contrast (Fig. 3.5-B), luminance (Fig. 3.5-C) and structure (Fig. 3.5-D) demonstrate that both modified *CS* pipelines outperform the standard *CS* pipeline. This means that both pipelines succeeded in recovery of structural and contrast information of datasets while there is not much difference between the quality of results of proposed pipelines in terms of numerical comparisons.

Fig. 3.6 provides the *HFEN* and *mean-SSIM* metrics for the renal data with Fig. 3.4A used as a gold standard. *Mean-SSIM* is used for this dataset which provides an estimation of image quality perceived considering elements of natural visual system. Again, these metrics demonstrate the better performance of alternative *CS* methods compared with standard *CS*

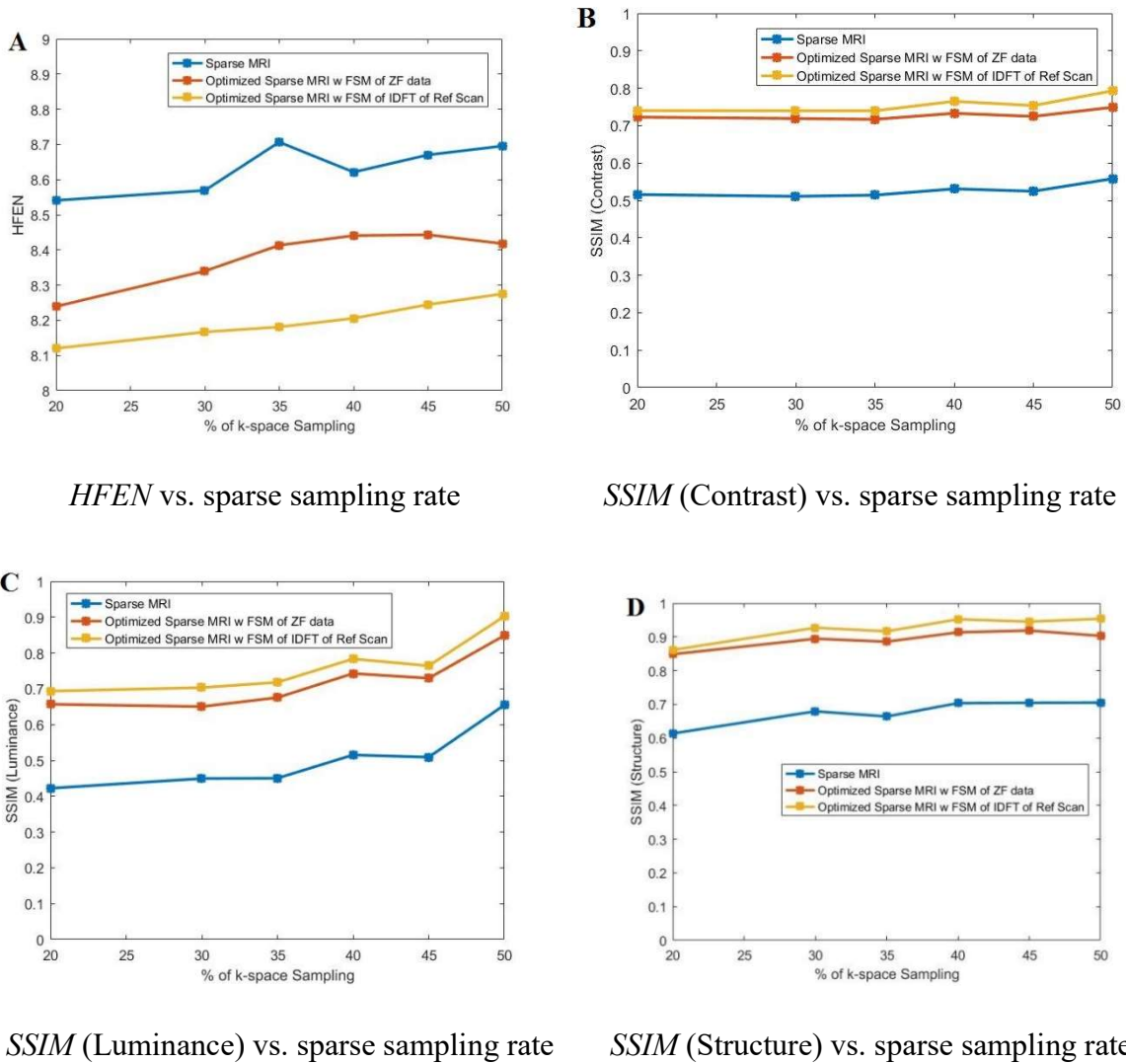
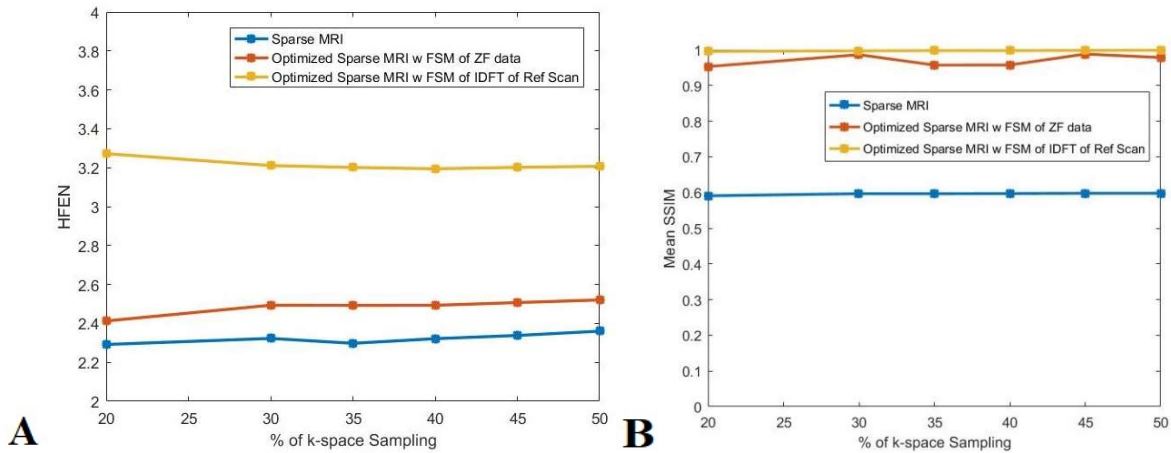


**Figure 3.5** A) *HFEN*, B) *SSIM*-Contrast, C) *SSIM*-Luminance, D) *SSIM*-Structure measures applied on  $108 \times 108$  GE *k*-space CS reconstructed using Sparse MRI (blue lines), optimized Sparse MRI with *FSM* information acquired from zero-filled (*ZF*) data (red lines) and optimized Sparse MRI with *FSM* information acquired from *IDFT* of reference scan (yellow lines).



*HFEN* vs. sparse sampling rate

mean-*SSIM* vs. sparse sampling rate

**Figure 3.6 A) *HFEN*, B) *mean-SSIM* measures applied on  $128 \times 128$  Renal *k*-space *CS* reconstructed using Sparse *MRI* (blue lines), optimized Sparse *MRI* with *FSM* information acquired from zero-filled (*ZF*) data (red lines) and optimized Sparse *MRI* with *FSM* informaion acquired from *IDFT* of reference scan (yellow lines).**

reconstruction technique. The mean-*SSIM* for both alternative *CS* methods provides very similar results which is also predictable from Fig. 3.4 for which C and D differ in specific structural accuracy. Similar conclusions can be made from Fig. 3.5 for which luminance, structure and contrast show very close numerical results. This indicates that such metrics provide insights additional to visual comparison to emphasize where and how different methods differ.

### 3.8 Conclusion and Future Work<sup>5</sup>

In this study, changes to acquired *MR k*-space data are proposed in *CS* pipelines to improve the resolution achieved during *CS* reconstruction of under sampled data by correcting Gibbs' artifacts independently of the suppression of under sampling noise. The theory of how adaptive

<sup>5</sup> This Conclusion from the submitted paper partially overlaps with the content of Chapter 6.

*FSM* through *TV* optimization will enable correction of Gibbs' effects was discussed. Two approaches to providing *FSM* estimates are proposed, to be acquired from *IDFT* of fully sampled *k*-space initial reference scan, as a pre-processing stage, or from *IDFT* of initial zero-filled under sampled *k*-space, as a post-processing stage. The former provides more accurate results but is less applicable in comparison to the later technique. The algorithms are validated for a common *CS-MRI* protocol (*SPARSE-MRI*) using a GE phantom and clinical *MR* data. The performance measurement of algorithms using preliminary observer tools shows the potential of proposed changes in positively affecting the diagnostic results. Future work is needed to improve the accuracy of *FSM* estimates acquired from initial zero-filled under sampled *k*-space to possibly mimic the reconstruction accuracy of *FSM* estimates acquired from *IDFT* reconstruction of initial reference scans.

### 3.9 Summary of the Chapter

In this chapter, the common *DFT*-imposed distortions associated with one of *DFT*-based algorithms, *CS*, is explored. The focus was a common *CS* package, *SPARSE-MRI*, for which an improved objective function is proposed which considers individual weights for regularization of fundamentally different artifacts, Gibbs's and under-sampling. *SPARSE-MRI* is chosen in this context as representative of compressed sensing based on non-adaptive sparse basis. Although the scope of this paper is limited to certain sparse bases, the proposed changes can be fitted into any *CS* software. This is demonstrated in the next chapter where the proposed changes are applied in the context of the new *CS* approach based on adaptive sparsity, or dictionary learning *CS-MRI*.

## Chapter Four: **Proposed Methods in Compressed Sensing Algorithms (II)**

### **4.1 Introduction<sup>6</sup>**

A significant mutation in compressed sensing (*CS*) techniques occurred with the introduction of dictionary learning (*DL*) theory to *MR* applications. *DL* emerged as a method to better represent data sets in reduced dimensionality subspaces. Such subspaces were aimed to be adaptive to both the characteristics of the signals and the processing method (Olshausen and Field, 1996; Engan et al., 1999; Aharon et al., 2006; Yaghoobi et al., 2009).

As discussed in the previous chapter, *CS* emerged in *MR* applications as a compromise between temporal and spatial resolution when current *DFT* reconstruction approaches failed to overcome all challenges of limited data acquisition. *CS MRI* based on dictionary learning (*DL-MRI*) has been suggested to solve some of the challenges present in the original *CS* approaches. This technique outperforms the primary *CS* techniques in reconstruction of high frequency components (Qu et al., 2010; Ravishankar et al., 2011; Hao et al., 2013). However, once again, we suggest that neglecting to consider suppressing *DFT*-imposed artifacts independently of other factors will cause *DL-MRI* results to have lower than expected image quality. The inherent filtering effect present in *CS* approaches such as *SPARSE-MRI* algorithm that partly removed *DFT* artifacts are eliminated in *DL-MRI*. This effect leaves behind the potential for an increased level of ringing artifacts in the neighborhood of image fine detail during each *DFT*-based reconstruction stage. Therefore, we suggest that overlooking these *DFT* issues will have an even more expensive cost than with earlier *CS* approaches since *DL-MRI* targets more accurate reconstruction of edges and fine details.

---

<sup>6</sup> This chapter is reformatted from the paper “Improved Dictionary learning *CS MRI* through Patch based *TV* regularization” by **Paniz Adibpour**, Elise Fear and Michael Smith submitted to IEEE ICASSP 2018, October 2017.



## 4.2 Overview of the concept of Improved Dictionary learning *CS MRI* through Patch based *TV* regularization<sup>7</sup>

Lower data acquisition times that provide accurate magnetic resonance imaging (*MRI*) reconstructions are achieved with compressed sensing (*CS*) by modeling under-sampled data using non-linear algorithms employing analytical sparse bases. Improved reconstruction can be achieved using dictionary learning (*DL*) frameworks to adaptively identify sparsifying transforms better matched to local feature characteristics. Both the original and *DL-CS* approaches make use of the discrete Fourier transform (*DFT*), and are inherently subject to Gibbs artifacts. These artifacts are suppressed alongside under-sampling and other artifacts during *CS* and *DL-CS* reconstruction. We suggest that the *DFT*-related artifacts will appear stronger in *DL-CS* approaches because of the improved sparsification inherent in the *DL-CS* approach. We propose a patch-based total variation (*TV*) regularization that independently corrects *DFT*-imposed Gibbs distortions, leading to sparser basis function representation of the local patches. The proposed method is validated by comparison with *CS* and *DL-CS* algorithms using GE phantom data.

## 4.3 Detailed background to *CS MRI* techniques and Motivation for the proposed methods

Compressed sensing (*CS*) algorithms are non-linear algorithmic approaches to reconstructing images from under-sampled data sets in areas such as magnetic resonance imaging (*MRI*).

Standard *CS* approaches (e.g Lustig et al., 2007; Qu et al., 2010; Ma, 2011; Hao et al., 2013) make use of analytical sparse bases originating in standard functions, e.g. wavelet, curvelet,

---

<sup>7</sup> This section is the abstract of submitted paper.

contourlet or discrete cosine, to generate sparse parameters regardless of the specifics of the anatomical structure present in an image. Adaptive sparsity based on dictionary learning (*DL*) has recently been suggested to mitigate limitations introduced by analytical sparsity (e.g. Ravishankar et al., 2011). Adaptive approaches attempt to sparsify based on patch-based image dictionaries to improve the reconstruction of high frequency components.

As with the original *CS* approach, *DL-CS* makes repeated use of discrete Fourier transform (*DFT*) processing stages. Each stage's results are inherently subject to the well-known associated limitations of three Gibbs related distortions near high resolution features – ringing artifacts, peak intensity loss and feature width increase (Harris, 1978). While it is anticipated these will be suppressed during reconstruction, the impact of *DFT*-related artifacts will appear stronger in *DL-CS* than with standard *CS* reconstructions because of the fine tuning of the basis representation.

The suppression of *DFT* artifacts independent of *CS*-related problems hasn't been considered important since *DL-CS* often focuses on the reconstruction of under-sampled high-resolution *MR* data (Aharon et al., 2006; Engan et al., 1999; Olshausen and Field, 1996; Yaghoobi et al., 2009). However, it has been demonstrated that applying *CS* reconstruction to unfiltered, truncated *MRI* data sets led to preferential enhancement of patch resolution depending on the patch's position within the field of view (*FOV*) (Ravishankar et al., 2011; Smith et al., 2013; Smith et al., 2015). We propose changes to the pipeline of *DL-CS* software to take advantage of this position dependent resolution enhancement in the absence of *k*-space filtering.

The chapter is organized as follows. In Section 4.4, the theory behind *DL-CS* technique is introduced. Section 4.5 outlines the proposed complementary objective function to adaptively re-sparsify basis functions of local patches through our proposed Fourier shift manipulation (*FSM*).

In Section 4.6, the necessary changes to the *DL-CS* pipeline to fit the proposed theory are introduced. Section 4.7 provides results from a GE phantom study.

#### 4.4 Theory

In the following sections, first theoretical background of *DL-MRI* technique is introduced. Then, the positional resolution enhancement of such technique is detailed as a basis for the proposed alternative *DL-MRI* theory discussed in this study.

##### 4.4.1 *DL-MRI* based on adaptive sparse representation

Since the choice of sparse transform in *CS* algorithms is very much dependent on image features, patch-based adaptive sparsity or *CS* based on dictionary learning (*DL*) uses patch-based dictionaries to capture local image features. It is shown in (Ravishankar et al., 2011) that such property provides higher sparsity and eliminates noise and under-sampling artifacts without imposing resolution loss. In an adaptive *DL* sparse representation in the complex domain,  $C$ ,  $I_{ij} \in C^n$  is the vector representation of 2D image patch of  $n$  pixels of size  $\sqrt{n} \times \sqrt{n}$ , with  $ij$  the index of location of its top-left corner,  $(i, j)$ , in the 2D image. The image patch,  $I_{ij}$ , can be formulated as a linear combination of its sparse representation,  $\alpha_{ij} \in C^K$ , through  $D\alpha_{ij}$  where  $D \in C^{n \times K}$  is the image patch-based dictionary with  $K$  atoms (columns) with each atom corresponding to an  $\sqrt{n} \times \sqrt{n}$  “elemental patch”.

In *DL-MRI*, first the dictionary and patch-based sparse representations are identified from an initial scan  $I$  by solving the following cost function

$$\min_{D, \Gamma} \sum_{ij} \| R_{ij} I - D \alpha_{ij} \|_2^2 \text{ s.t. } \| \alpha_{ij} \|_0 \leq T_0, \forall i, j \quad (4.1)$$

In Eqn. (4.1),  $R_{ij} \in C^{mp}$  is the patch extracting operator from image  $I$  through  $R_{ij} I = I_{ij}$ ,  $\Gamma$  is the sparse representation set  $\{\alpha_{ij}\}_{ij}$  of all training patches of image and  $T_0$  is the sparse threshold. As Fig. 4.2 (*DL-MRI* scheme) also demonstrates, in (Ravishankar et al., 2011) the *K-SVD* algorithm is used to adaptively generate the dictionary sets from reference *MR* scans and  $\alpha_{ij}$  is determined by performing sparse coding on all patches (Aharon et al., 2006). Based on Fig. 4.2-A,  $I$  can then be determined using learned sparse dictionaries and from under sampled  $k$ -space through the following least squares problem

$$\min_I \sum_{ij} \| R_{ij} I - D \alpha_{ij} \|_2^2 + \nu \| F_u I - y \|_2^2 \quad (4.2)$$

once sparse representations and the dictionary are determined and fixed.

With the above *CS* formulation, sparsity is generated based on learning local image features. This approach avoids the natural noise buried in acquired  $k$ -space samples and the aliasing caused by under sampling of  $k$ -space (Ravishankar et al., 2011). Unlike *CS-MRI* based on an analytical sparse basis, this method has the potential to lead to a more accurate reconstruction of high frequency components.

#### 4.4.2 <sup>8</sup>Positional resolution enhancement in *DL-CS*

The left side of each image in Fig. 4.1 shows reconstructions of two patches containing the comb features from a GE *MRI* phantom superimposed on a smooth broad feature. The x-position of the

---

<sup>8</sup> This section is a re-worked section of the paper adapted to the chapter format due to conceptual similarity to section 3.4.2.

lower patch is shifted by 2 high resolution pixels relative to the upper, a positional shift of only 0.4% *FOV*. The right side of each image shows two cross-sections of each patch.

Fig. 4.1A is the 108x108 *DFT* reconstruction of truncated data with no *k*-space filtering. The shifted patch demonstrates a higher level of Gibbs artifacts distortion than noted in the upper patch. In Fig. 4.1B, the *CS* reconstruction using 33% of the truncated data shows an upper patch with most of the artifacts removed. The lower patch, shifted by 0.4% *FOV*, shows minimal reduction in the Gibbs artifacts and no intensity gain despite removal of the under-sampled noise. This positional resolution enhancement occurs because, after truncation, the upper patch signal components for both *DFT*-based algorithms are exactly represented by the basis (sparse) functions of the truncated data space, but those of the lower patch are not.

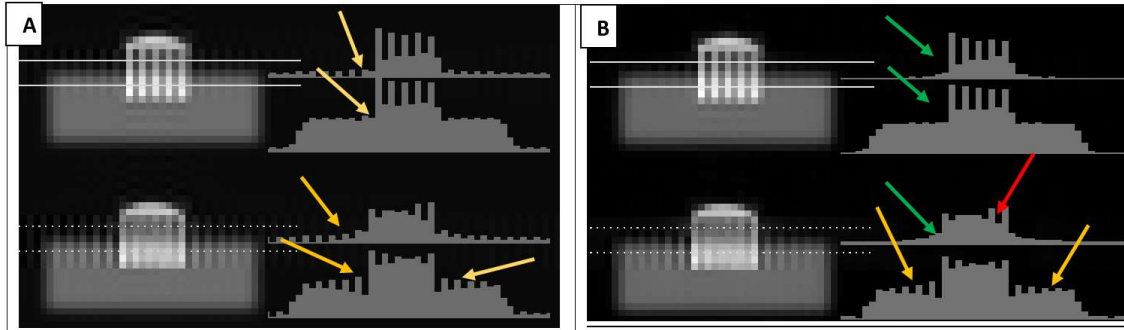


**Figure 4.1 A) *DFT* reconstruction of a truncated data set is compared to B) *CS* reconstruction using 33% of the data.**

We suggest the use of a fundamental Fourier property to gain deliberate advantage of this positional dependent patch enhancement. The *DFTs* of impulses placed at positions  $x$  and  $x + \Delta x$  in an  $N$  point data sequence are respectively  $\exp(-j2\pi kx / N)$  and  $\exp(-j2\pi k(x + \Delta x) / N)$ . We propose applying a Fourier shift manipulation, *FSM*, of the *k*-

space data, specifically multiplication by  $\exp(+j2\pi k\Delta x / N)$ . This introduces a  $\Delta x$  virtual position shift in the *FOV*. We propose a complementary optimization which aims to re-sparsify basis function characteristics of image patches. This is achieved through a *TV* regularization procedure by which image patches are automatically and selectively resampled through *FSM* phase ramping. Since *DL-CS* adapts the dictionary and sparse frame work using a fixed reference scan, the approach will re-sparsify basis function characteristics of the reference scan and use this information for further phase correction of under sampled *k*-space.

#### 4.5 Proposed Alternative *DL-MRI* Formulation

We propose a complementary optimization which aims to re-sparsify basis function characteristics of image patches. To achieve this, a *TV* regularization procedure is introduced by which image patches are automatically and selectively resampled through phase ramping. Since *DL-MRI* adapts the dictionary and sparse frame work using a fixed reference scan, we propose to re-sparsify basis function characteristics of the reference scan and use that information for further phase correction of under sampled *k*-space.

The following optimization provides the mathematical representation of the proposed changes to *DL-MRI* procedure

$$\min_{D, \Gamma, x_{shj}, y_{shj}} \sum_{ij} \|I_{ij} - D\alpha_{ij}\|_2^2 + TV(RS_{x_{shj}, y_{shj}}(I_{ij})), \quad (4.3-A)$$

$$\forall i, j, -1/2 \leq x_{shj}, y_{shj} \leq 1/2; -1/2 \leq y_{sh1}, \dots, y_{shN} \leq 1/2 \text{ s.t. } \|\alpha_{ij}\|_0 \leq T_0, \forall i, j$$

$$\text{where } RS_{x_{shj}, y_{shj}}(I_{ij}) = IDFT(S_{ij}(k).W(k, x_{shj}, y_{shj})) \text{ and } I_{ij} = R_{ij}I \quad (4.3-B)$$

$$\begin{aligned}
& \text{for } W(k, x_{sh_j}, y_{sh_j}) = \\
& \exp(2\pi j [(-\sqrt{N}/2)x_{sh_j} \Delta k_x + (-\sqrt{N}/2)y_{sh_j} \Delta k_y]) \dots \exp(2\pi j [(\sqrt{N}/2-1)x_{sh_j} \Delta k_x + (\sqrt{N}/2-1)y_{sh_j} \Delta k_y]) \\
& \dots \dots \dots \\
& \exp(2\pi j [(-\sqrt{N}/2)x_{sh_j} \Delta k_x + (-\sqrt{N}/2)y_{sh_j} \Delta k_y]) \dots \exp(2\pi j [(\sqrt{N}/2-1)x_{sh_j} \Delta k_x + (\sqrt{N}/2-1)y_{sh_j} \Delta k_y])
\end{aligned} \tag{4.3-C}$$

Eqns. 4.3 (A) – (C) form a complementary dictionary learning objective function which enables definition of set of dictionaries using patch-based analysis. A  $TV$  regularization objective function is also added as part of this learning method which clarifies patch-based features to avoid common artifacts, e.g. Gibbs' distortions, that decrease the accuracy of dictionary sets.

$RS_{x_{sh_j}, y_{sh_j}}(I_{ij})$  is the Fourier manipulated patch of reference image acquired through multiplication of  $W(k, x_{sh_j}, y_{sh_j})$ , the frequency shift modulation matrix which applies frequency upshifting through  $S_{ij}(k)$ .  $W(k, x_{sh_j}, y_{sh_j})$  contains shift factors  $x_{ij}, y_{ij}$  for specific patch of the image  $k$ -space ( $S_{ij}(k)$ ), and specific image patch.

After learning dictionaries by patch-based analysis of initial reference image, the reconstruction procedure can be applied on sparse sampled data set using the following equations:

$$\min_{I, x_{sh_j}, y_{sh_j}} \sum_{ij} \|R_{ij}I - D\alpha_{ij}\|_2^2 + \nu \|F_u I - y\|_2^2 \text{ s.t. } \|\alpha_{ij}\|_0 \leq T_0, \forall i, j \tag{4.4}$$

$$\min_{x_{sh_j}, y_{sh_j}} TV(RS_{x_{sh_j}, y_{sh_j}}'(I)) \text{ s.t. } -1/2 \leq x_{sh_1}, \dots, x_{sh_N} \leq 1/2; -1/2 \leq y_{sh_1}, \dots, y_{sh_N} \leq 1/2 \tag{4.5-}$$

A)

$$\text{where } RS'_{x_{shj}, y_{shj}}(I) = IDFT(S(k).W'(k, x'_{shj}, y'_{shj})) \quad (4.5-B)$$

$$\begin{aligned} W(k, x'_{shj}, y'_{shj}) = & \exp(2\pi j [(-\sqrt{N}/2)x'_{shj} \Delta k_x + (-\sqrt{N}/2)y'_{shj} \Delta k_y]) \dots \exp(2\pi j [(\sqrt{N}/2-1)x'_{shj} \Delta k_x + (\sqrt{N}/2-1)y'_{shj} \Delta k_y]) \\ & \dots \dots \dots \\ & \exp(2\pi j [(-\sqrt{N}/2)x'_{shj} \Delta k_x + (-\sqrt{N}/2)y'_{shj} \Delta k_y]) \dots \exp(2\pi j [(\sqrt{N}/2-1)x'_{shj} \Delta k_x + (\sqrt{N}/2-1)y'_{shj} \Delta k_y]) \end{aligned} \quad (4.5-C)$$

Based on above formulation, the appropriate dictionary, sparse representations and frequency shift manipulation estimates are first determined (Eqn. 4.4) and then optimized  $I$  will be calculated solving objective function of Eqn. 4.4 using 4.5. The interpretation of Eqn. 4.5 is that sparse framework is adaptively determined through the  $l_2$ -norm optimization and the data fidelity is controlled through the second objective function. The  $FSM$  factors are optimized for 2D  $DFT$  in both  $x$  and  $y$  directions using Eqn. 4.5. From now on, we will refer to this procedure as ***patch-based TV optimization*** technique.

## 4.6 Materials and Methods

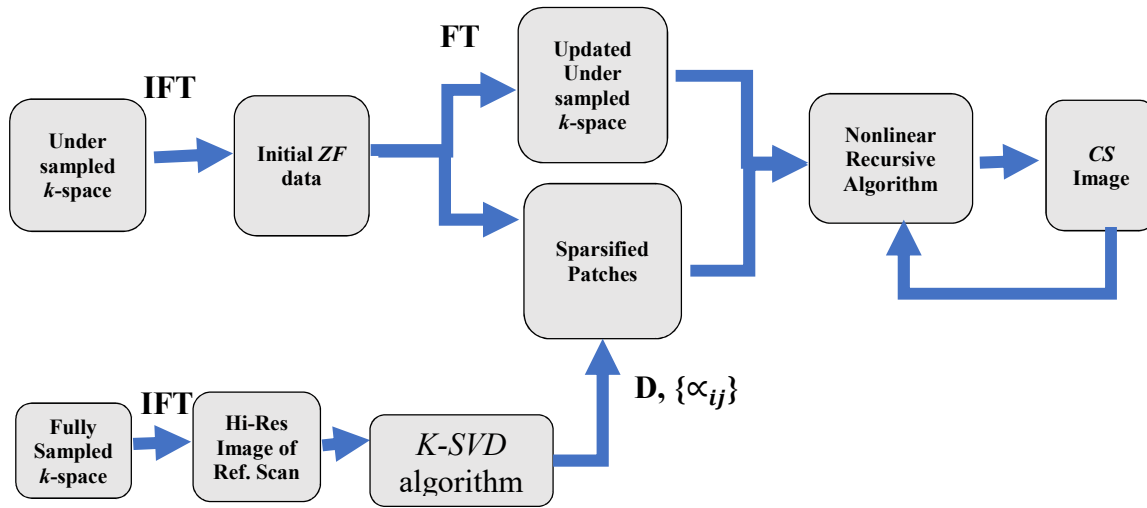
In the following sections, first proposed changes in *DL-MRI* pipeline are introduced to match the proposed theory. Then appropriate quantitative metrics are suggested to be used for validation of proposed algorithm. Imaging details of the datasets used in this study are also discussed in the last section.



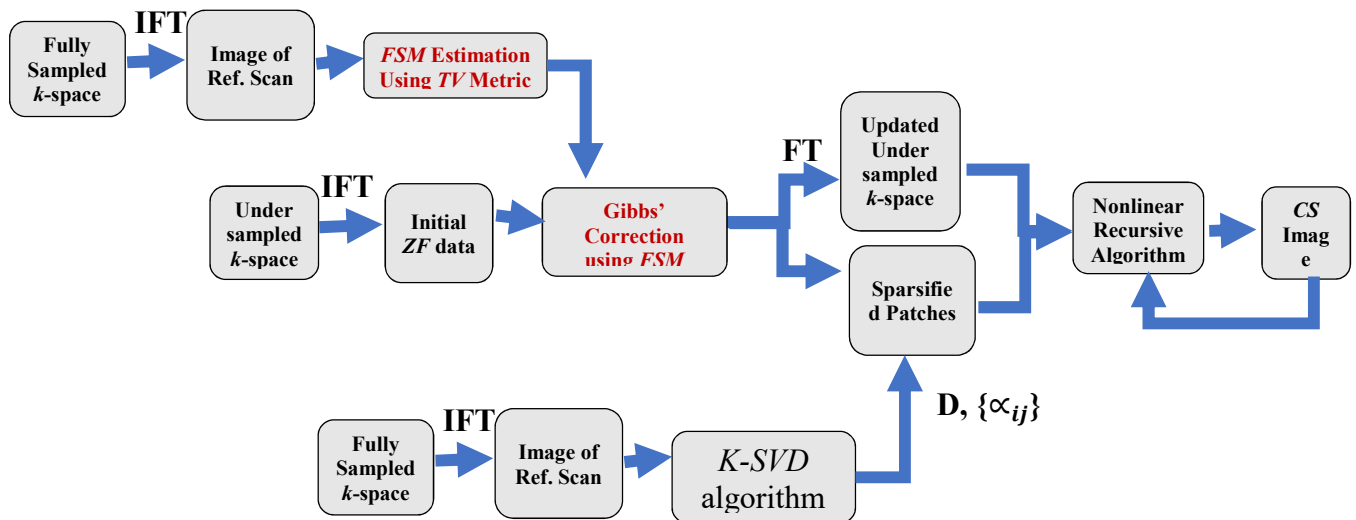
#### 4.6.1 Proposed Design Pattern in *DL-MRI* Pipeline

Fig. 4.2B represents the practical implementation of the proposed *DL-CS* algorithm to change both the dictionary set definition stage and the reconstruction procedure using pre-defined adapted dictionary sets. As in the original algorithm (Ravishankar et al., 2011), we propose to first define patch-based sparse bases through a dictionary learning method using an initial scan

##### A) *DL MRI Scheme*



##### B) *Proposed DL MRI Scheme*



**Figure 4.2 A) The existing *DL-MRI* pipeline can be modified to remove Gibbs' artifacts independently of under-sampling noise using *FSM* estimates derived from B) a preparatory full *k*-space scan.**

which possess undistorted features. This may impose longer post-processing time to define all sets of dictionaries.

In the next step, the regularization procedure is applied on under-sampled datasets. Although *DL-CS* is shown (Ravishankar et al., 2011) to have better fine detail reconstruction compared to *SPARSE-MRI* (Lutig et al., 2008), the constant validation of these algorithms with high resolution experimental datasets, leaves the practical usage of such algorithms under question. Through the proposed pipeline we offer to use smaller under-sampled datasets and ~~instead~~ correct *DFT*-imposed distortions using similar patch-based *TV* optimization applied to the first step. This method improves temporal resolution by decreasing acquisition time while preserving the effective resolution.

#### **4.6.2 <sup>9</sup>Quantitative metrics to compare *DL-CS* and patch-based *TV* Regularization reconstructions**

In order to validate proposed algorithm, we suggest the use of three metrics which focus on the structural similarity, or lack of it, between images as perceived by human vision. The high-frequency error norm (*HFEN*) quantifies the quality of reconstruction of edges and fine features (Ravishankar et al., 2011). The structural similarity index map (*SSIM*) represents a comparison map for luminance, contrast and structure with each pixel intensity quantifying the level of similarity between gold standard and the test image (Wang et al., 2004), and provides a

---

<sup>9</sup> This section has contents in common with section 3.6.2, both describing necessary numerical metrics used for validation of algorithms presented in two individual papers.

numerical value for each of the properties. The high dynamic range visual difference predictor (*HDR-VDP-2.0*) provides a visual comparison map with pixel intensities identifying the probability of difference detection by the human visual system. This metric examines the quality of the reconstructed image and a gold standard, numerically predicting the percentage of similarity between gold standard and the test image (Mantiuk et al., 2011).

#### 4.6.3 Imaging Details

The *MRI* experimental  $512 \times 512$  raw  $k$ -space data set from a GE phantom presented in Fig. 4.1 was provided by Dr. MacDonald, University of Calgary, Canada. The data was obtained using a fast gradient recalled echo sequence with  $FOV_M$  of  $18\text{ cm} \times 18\text{ cm}$ .

*DL-MRI* software (Ravishankar et al., 2011) is studied in this work. The software protocol is kept unchanged.  $K$ -space sampling pattern with 33% sampled including 10% full sampled central core and variable density random sampling pattern of periphery of  $k$ -space is applied on the input data. *SPARSE-MRI* software (Lustig, 2006) is also used in this study to examine performance of algorithms, with that software's protocol kept unchanged. A similar  $k$ -space sampling pattern to that used for *DL-MRI* study is applied -- 33% sampled including 10% full sampled central core and variable density random sampling pattern in the periphery of  $k$ -space.

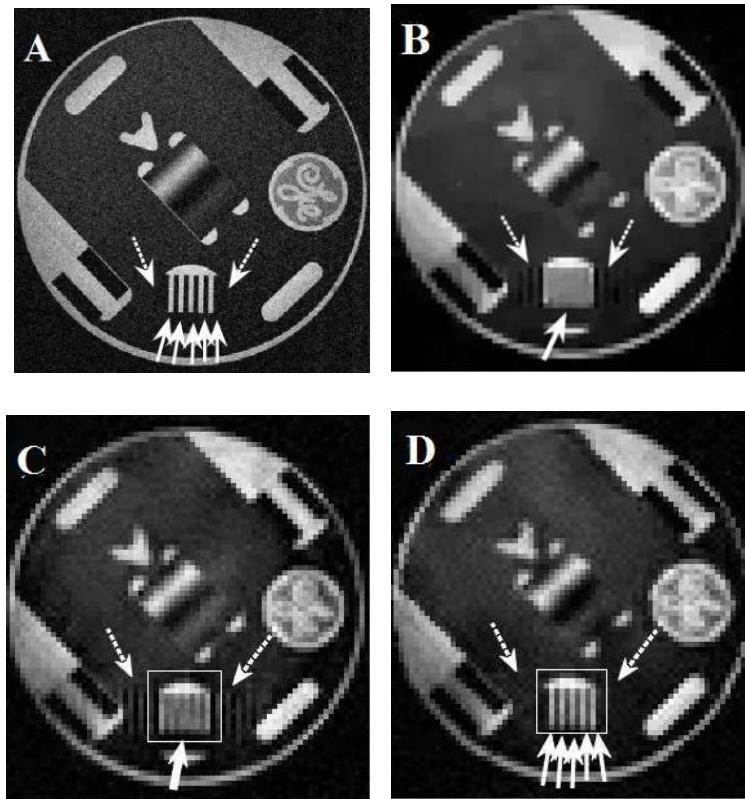


**Figure 4.3** A) The high resolution *DFT* reconstruction from a  $512 \times 512$  GE data set are compared to B) a standard *SPARSE-MRI CS* reconstruction, C) a standard *DL-MRI CS* reconstruction and D) *patch-based TV* regularized *DL-MRI* reconstructed with *FSM* estimates from *IDFT* of initial scan.

## 4.7 Results and Discussion

### 4.7.1 Experimental results

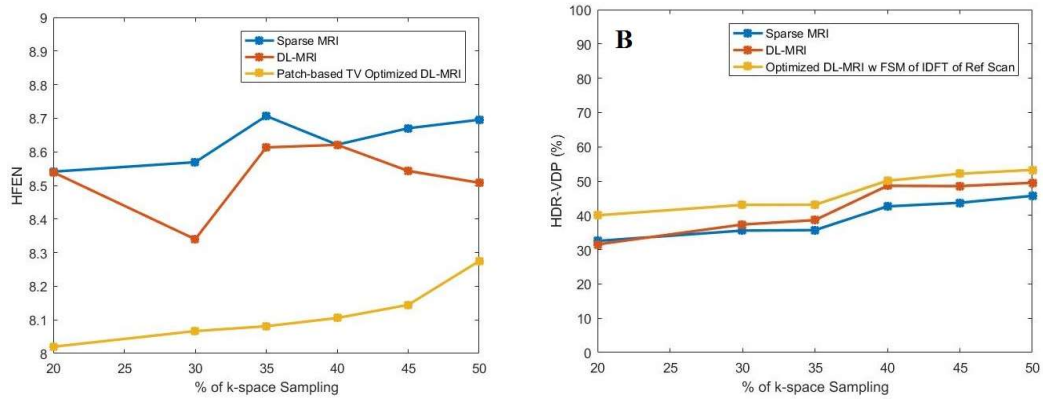
Fig. 4.3-B, C and D represent results of the *CS* algorithms applied on the GE data in comparison with the high-resolution GE phantom shown in Fig. 4.3-A. For illustration purposes, *CS* algorithms are applied on  $108 \times 108$   $k$ -space truncated data that is sparse reconstructed using *SPARSE-MRI* software. In Fig. 4.3-B, some patches have lost information due to Gibbs' artifacts (solid white arrow) and the residual Gibbs' effects have also affected neighborhood areas

(dashed white arrows). The result of *DL-CS* software, Fig. 4.3-C, demonstrates that this algorithm fails in differentiation of artifacts (solid and dashed arrows of *DFT*-imposed Gibbs' artifacts). Also, the residual artifacts appear even stronger (dashed arrows) since the regularization procedure hasn't smoothed out residual Gibbs' effects leading to enhanced distortions on the neighboring pixels.

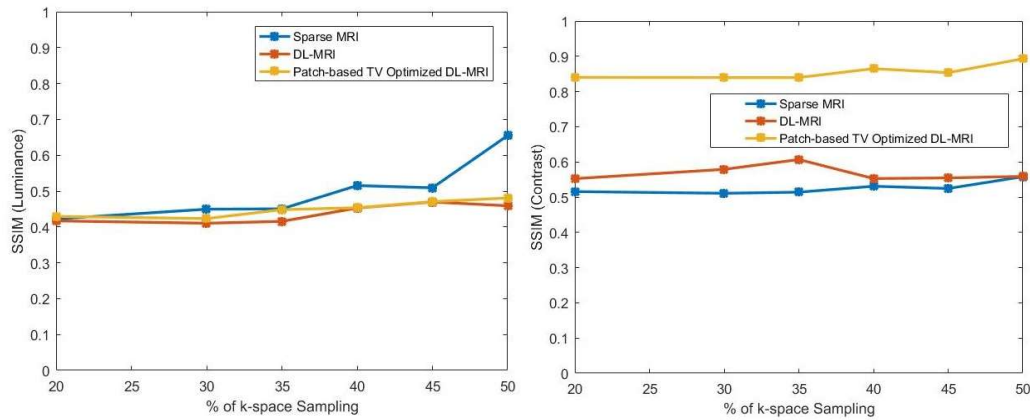
Fig. 4.3-D, the result from patch-based *TV* optimized *DL-CS*, demonstrates the effectiveness of adaptive Fourier manipulation of an *ROI* as a technique for mitigation of *DFT*-imposed artifacts. The area enclosed by the white rectangle is the specific patch (*ROI*) size used for the complementary optimization algorithm. The specific *ROI* enclosed with this rectangle has an effective resolution comparable to the gold standard, Fig. 4.3-A. The comb tines are fully recovered, and the residual Gibbs' effects, which strongly appeared in neighborhood of comb feature, are completely removed (white dashed arrows). This indicates the advantage of separately tackling the two independent noise sources – Gibbs artifacts and under-sampling noise.

#### 4.7.2 Performance Measure of Proposed method

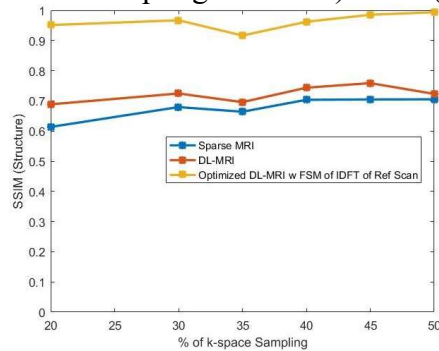
Application of a numerical quality measure can be indicative of stability of the proposed techniques. Fig. 4.4 provides a comparison of the *HFEN*, *HDR-VDP* (percentage) and *SSIM* metrics for 108x108 GE data reconstructed using *DL-CS*, proposed optimized *DL-CS* algorithms and *SPARSE-MRI* software results.



A)  $HFEN$  versus sampling rate    B)  $HDR-VDP$  (%) versus sampling rate



C)  $SSIM$  (Luminance) versus sampling rate    D)  $SSIM$  (Contrast) versus sampling rate



E)  $SSIM$  (Structure) versus sampling rate

**Figure 4.4 A)  $HFEN$ , B)  $HDR-VDP$  (%), C)  $SSIM$ -Luminance, D)  $SSIM$ -Contrast, E)  $SSIM$ -Structure measures applied on 108x108 GE  $k$ -space  $CS$  reconstructed using  $DL-MRI$ , optimized  $DL-MRI$  with  $FSM$  information acquired from  $IDFT$  of reference scan.**

The high frequency error is the lowest for patch-based *TV* optimized *DL-CS*. Although *DL-CS* also demonstrates less high frequency error, this metric indicates little difference between *DL-CS* and *SPARSE-MRI*; this numerical result reflects the qualitative appearance seen in Fig. 4.3. *DL-CS* attempts to mimic characteristics of reconstructed high frequency components, lines and edges. However, as with *SPARSE-MRI*, it fails to clarify Gibbs's distortions as shown by the low success in the *HFEN* results. The *SSIM-Luminance* results do not provide much insight into the relative effectiveness of the algorithms. However, the *SSIM-Contrast* and *SSIM-Structure* results support the claim of the superiority of *TV* optimized *DL-CS* in improving the effective resolution (contrast). This better structural detail reconstruction of proposed algorithm is also evident from *HDR-VDP* results.

#### 4.8 Conclusion and Future Work

In this study, a complementary optimization algorithm is proposed for a new generation of *CS* techniques (*DL-CS*). We suggest that there are advantages to separately modeling the artifacts associated from under-sampling that are suppressed in *CS* and *DL-CS* reconstruction and the inherent artifacts generated by employing *DFT*-based reconstruction stages. While ringing may be suppressed during *CS* and *DL-CS*, the other Gibbs's artifacts, loss of intensity and increased width of sharp detail, remain. The proposed objective function aims to reconstruct images from pre-learned dictionaries while independently optimizing the basis *DFT* functional characteristics on a patch-based level. The proposed algorithm is theoretically outlined, and a new *DL-CS* pipeline proposed. A qualitative improvement is shown in images when the new approach is empirically employed on GE phantom data. The advantage of separating the

elimination of Gibbs and other *CS*-related artifacts is supported by the quantitative results using *SSIM*, *HFEN* and *HDR-VDP2.0* metrics.

#### 4.9 Summary of the Chapter

In this chapter, the *DFT* imposed artifacts are explored in a new generation of *CS* techniques based on dictionary learning. It is shown that the effect of Gibbs' artifacts appears stronger near edges and sharp features, which make it a challengeable phenomenon in recent developed *CS* techniques. New changes have been proposed using patch-based *TV* regularization to eliminate Gibbs' effects appearing after regularization process. The proposed method is tied into *DL MRI* software theoretically and empirically. The results indicate that the proposed changes to the objective function and *CS* pipeline will introduce a two-level optimization to the *CS* technique which generates effective resolution more comparable with *IDFT* of full *k*-space data.

In order to show the applicability and generality of the optimized method in various algorithms based on *DFT* during data processing, I am going to explore an additional algorithm in context of my thesis. In the following chapter, the *DFT*-imposed problems will be explored in a microwave imaging technique known as tissue sensing adaptive radar (*TSAR*). It is shown that the optimization method based on Fourier manipulation of data can be a potential method in suppressing clutter and *DFT*-imposed artifacts in this microwave imaging application.



## Chapter Five: **Alternative preprocessing for radar-based microwave imaging**

### **5.1 Introduction**

Early diagnosis is critical for detection of many diseases to accelerate the treatment procedure. In some imaging applications, e.g. breast tumor detection, low resolution imaging techniques may also play an important role in applications such as treatment monitoring. Improvements to such techniques aim to increase accuracy of processing algorithms for reliability of detecting changes in tissues. The accuracy in processing has a direct relation with spatial resolution of the final 2D or 3D images. Therefore, studying factors that affect the final spatial resolution can assist in accuracy improvement of such algorithms.

In this chapter, one of the microwave imaging methods used for imaging is studied. Tissue sensing adaptive radar (*TSAR*) uses back-scattered microwave signals from breast anatomy to estimate the position of the tumor. One of the factors affecting spatial resolution, and possibly the accuracy of tumor detection, is the limitation in data gathering procedures. The necessary limited length of data acquisition imposes artifacts on the back-scattered signals. As discussed in previous chapters, this issue can be identified via fundamentals of discrete Fourier transform. In this chapter, the scope of studied algorithms is extended to microwave imaging techniques and the application of alternative methods in such imaging technique is studied.

In order to acquire a focused response for image formation, several pre-processing steps are required to reduce early and late time clutter, including removing the dominant response from the skin (Bond et al., 2003; Maklad et al., 2012) and additional necessary or optional data manipulation steps. While raw data acquisition and most of the preprocessing data manipulations are applied in frequency space, time transformation of data is required for specific steps of *TSAR*

system. The necessity of limited-length data acquisition (Curtis, 2015) and the use of discrete Fourier transform (*DFT*) to move data between Fourier domains introduce additional oscillations during these preprocessing steps. While low pass filters (*LPF*) can be considered as a straightforward option to reduce additional signal distortions, their usage always causes a trade-off between simplicity and loss of contrast-to-noise ratio. In fact, *LPF* impact an important feature of reconstruction maps, contrast ratio, which plays an important role in further tumor detection accuracy.

In this work, we explore extensions suggested in (Smith, 1993) to take advantage of digital signal processing (*DSP*) signal characteristics to reduce artifacts by making minor adjustments to frequency characteristics of pre-processed data. We will introduce the Fourier shift manipulation (*FSM*) approach to tune the frequency data such that ringing effects are reduced without the need to compromise between resolution loss and Gibbs' removal imposed by the global application of *LPF*. We will take advantage of the total variation (*TV*) metric to adapt the Gibbs' artifact suppression when using the *FSM* approach.

In section 5.2, the detailed background on microwave imaging techniques are reviewed with a focus on tissue sensing adaptive radar (*TSAR*). Then we provide an overview of the necessary *TSAR* preprocessing steps and demonstrate how each step might affect the time signals in section 5.3.

## **5.2 Detailed background to microwave imaging and tissue sensing adaptive radar method**

Breast cancer is the most common cancer among women and the top threat to women's health for which various imaging modalities are used at several stages including screening, diagnosis, biopsy, and treatment monitoring (American Cancer Society, 2005). Among various imaging

modalities for screening and early detection of breast tumors, x-ray mammography has broad clinical use (Morgan and Bair, 2013). While providing high spatial resolution, mammographic techniques have limitations in terms of repeated scanning for treatment monitoring.

Ultrasonography is a safe and inexpensive imaging approach, however has not been demonstrated to track changes during treatment. Magnetic resonance imaging (*MRI*) is applicable in different stages of screening, diagnosis and monitoring. However, as an expensive modality, it is suited for repeated imaging. Microwave imaging techniques are based on the significant contrast in dielectric properties of malignant and normal breast tissues at microwave frequencies. As these methods are very low power, non-ionizing, non-invasive and cost effective, they have been proposed as alternative imaging techniques for breast health monitoring. Contrary to X-ray techniques with potential high spatial resolution, microwave technology offers contrast corresponding to physiological factors of clinical interest (Fear et al., 2002). It also enables the 3D volumetric map representation of tissue properties which eliminates the need for breast compression (Fear et al., 2002).

The two classes of microwave imaging techniques include tomography and backscatter. Tomography requires solving an ill-conditioned nonlinear inverse scattering problem, which involves computationally intensive techniques (Fear et al., 2002). Backscatter methods aim at detecting the location of microwave scatterers in the breast. These methods were first introduced by Hagness *et al.* (Hagness et al., 1998) as confocal microwave imaging (*CFMI*). *CFMI* illuminates the breast with microwave signals from antennas located at different positions and measures the energy distribution from backscattered signals. The backscattered signals are used to calculate the round-trip time delay from each reconstruction point to each antenna position using an average propagation speed. Combining the distance estimates from each antenna position, a 3D

map of scattering objects can be created. This technique has shown capability in detecting tumors in physical phantoms, and patient studies.

### **5.2.1 Tissue sensing adaptive radar**

Tissue sensing adaptive radar (*TSAR*) (Sill and Fear, 2005) is a backscatter microwave imaging technique. The *TSAR* system consists of an imaging tank filled with a matching medium (canola oil), a vector network analyzer (*VNA*) used to record signals, the antenna which is used for both transmitting and receiving, a laser used to estimate the surface of the breast in the scanner, and an antenna positioning system used to scan the antenna around the breast 4 degrees of freedom (Curtis, 2015).

During data acquisition, the woman lies prone on the surface of the prototype with her breast extending through the tank. The antenna positioning system is used to rotate the antennas around the breast. At each azimuth location, the laser is scanned vertically to obtain an estimate of the breast contour. The estimated location of the contour is used to compute a predefined number of antenna positions. The mechanical positioning system locates the antenna to each of the predefined positions where microwave measurements are collected using a VNA at discrete frequencies, typically ranging from 10MHz to 12GHz in 10MHz steps for *TSAR* imaging with lower frequency further limited to 850 MHz in preprocessing steps due to practical considerations (Curtis, 2015). The results in (Curtis, 2015) also shows that higher sampling rates lead to similar time domain signals. This suggests that the number of frequency points during measurement can also be reduced. For testing algorithms, simulations of breast models illuminated by the antenna are performed with electromagnetics simulation tools (Curtis, 2015).

### 5.3 Preprocessing calculations in *TSAR* software

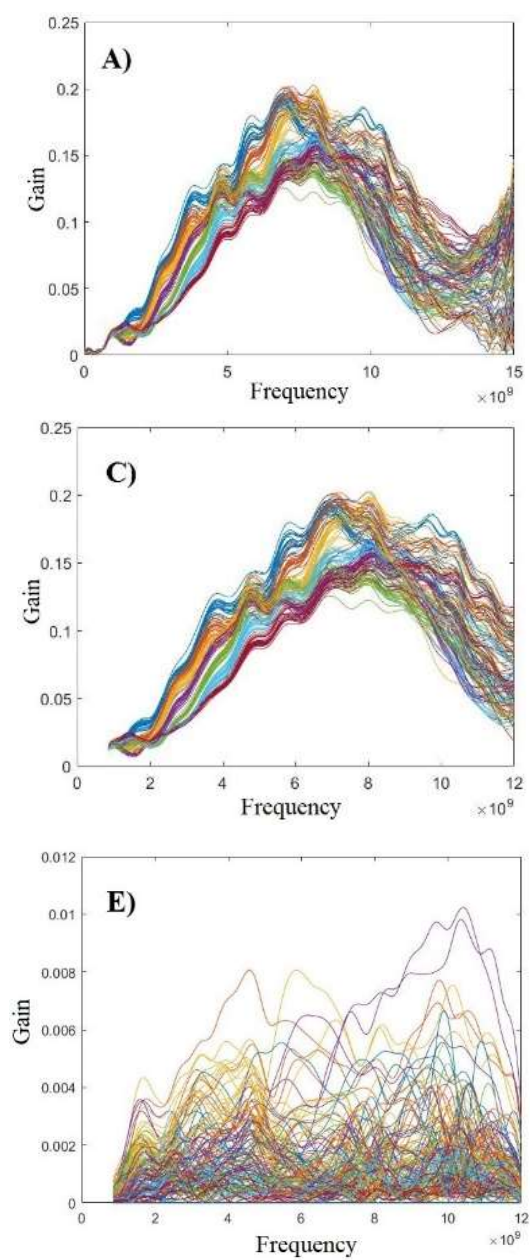
In this section, we review necessary preprocessing steps and discuss how they affect time signal characteristics. In the next section, we explore how Fourier manipulation of backscattered signals will help improving basis function characteristics of time signals.

#### 5.3.1 Necessary *TSAR* Preprocessing Steps and source of artifacts

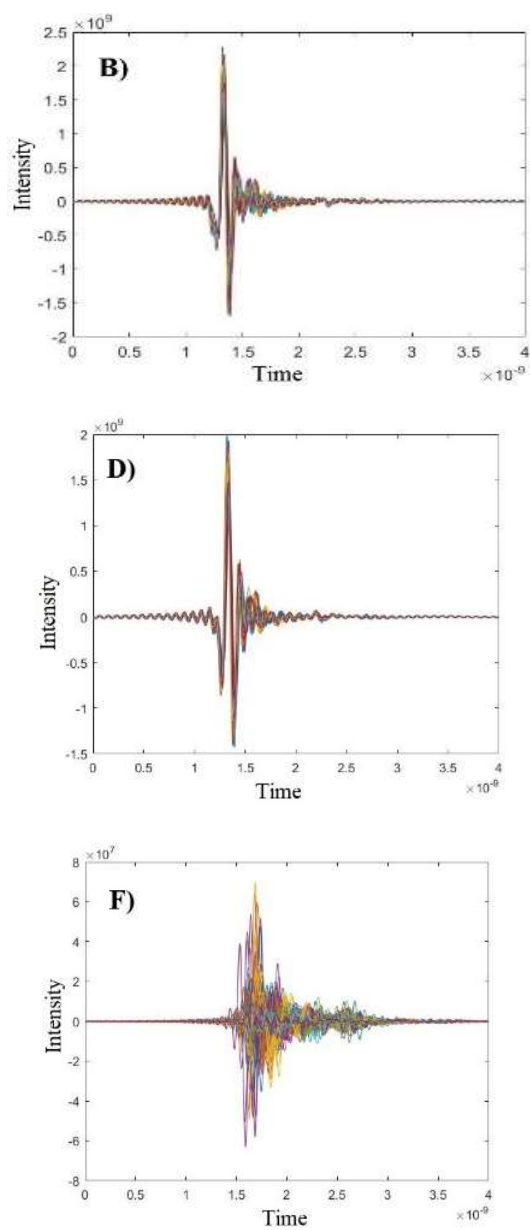
Four main sets of data are acquired during a *TSAR* scan: calibration data (data acquired without object present – referred to as “antenna only”), the target data (complex reflection coefficient of measured data with object present at antenna position), the antenna position data (antenna positions) and laser data (skin surface estimated by the laser). The following pre-processing steps, represented in pipeline 1 of Fig. 5.2, are applied using these four data sets:

1. *Calibration*: The target data not only consists of the back scattered signals from the target object but also includes the internal antenna reflections and the reflections from the system hardware. The necessary calibration step simply subtracts the antenna only data from the target data (Fig. 5.1A-B).
2. *Frequency truncation*: simulated data is acquired up to 15GHz, however is truncated to 12GHz to prevent high frequency noisy data from interfering with final contrast map (Fig. 5.1C-D). This is one of the steps which aims to avoid noise with the cost of truncation artifacts to processed signals.

Frequency signals



Time signals



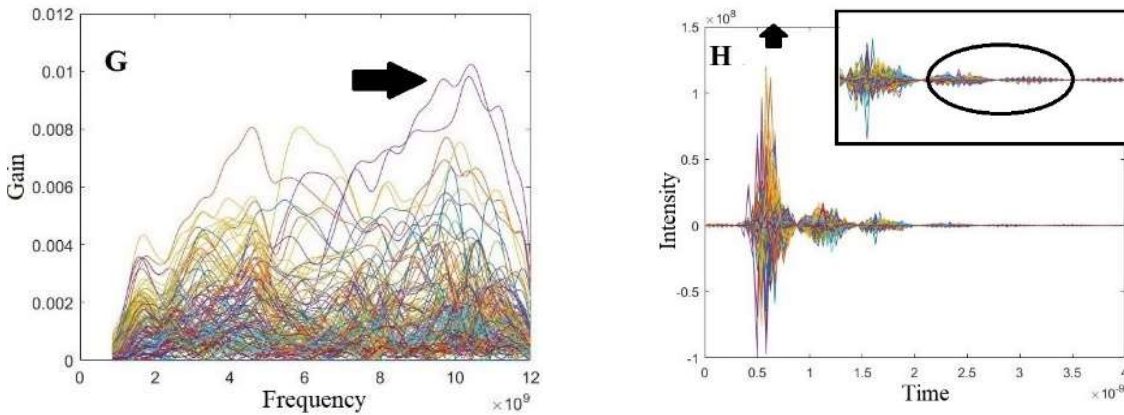


**Figure 5.1 Backscattered signals in preprocessing *TSAR* pipeline; Calibrated signal in A) frequency and B) time; signals after frequency truncation in C) frequency and D) time; signal after skin response subtraction in E) frequency and F) time; signals shifted to the aperture position in G) frequency and H) time;**

3. *Time Domain Transformation*: The frequency data have to be transformed to the time domain for further processing e.g. skin subtraction and final image formation (Curtis, 2015; Fear et al., 2002). Inverse chirp Z-transform (*ICZT*) is used for data transformation in *TSAR* software due to the following reasons. It has been shown in (Curtis and Fear, 2014) that to avoid quantization errors, a high time domain sampling rate is required. With maximum frequency of 12 GHz, the Nyquist sampling rate is  $\Delta t = 41.67 \text{ ps}$  while in fact the time signals are Sinc interpolated within *ICZT* algorithm to 2 ps sample spacing. Although *ICZT* eliminates the need to individually interpolate signals after transforming to time domain, this algorithm introduces oscillations to preprocessed data which can further influence image accuracy due to intensity loss of time signals.

4. *Skin Response Subtraction*: This step reduces the dominant reflection from the skin. An adaptive filtering method using the dominant skin response from a local neighborhood of

antennas (Maklad et al., 2012; Bond et al., 2003) is used in the *TSAR* algorithm to mitigate the dominant response from the skin (Fig. 5.1.E-F). Examination of frequency response of the tumour (Curtis, 2015) suggests the application of a *LPF* (e.g. a Hamming window) after skin subtraction. This aims at intensity reduction of higher frequencies which are not present when examining the isolated tumour response. While this filtering is important for reducing the dominant reflections from the skin that impede imaging, it might impose blurring and resolution loss to the final image maps.

5. *Shift to the aperture position*: There is a time delay between feed of the antenna where signals are measured and the aperture of the antenna. After suppression of skin response, the time signals are shifted such that their reference point corresponds to the antenna aperture. (Fig. 5.1G-&H).

6. *Image formation*: This step basically relates the time domain radar data to the spatial imaging domain using a delay and sum (*DAS*) imaging process introduced in (Curtis, 2015). Since the details of imaging algorithm is out of the scope of this thesis, the image formation process which consists of imaging grid definition and intensity allocation to pixel positions will be briefly reviewed in this section. In radar imaging, the grid spacing is defined using the breast surface estimate obtained from the laser data and is typically in 1-2mm cubic voxels (Curtis, 2015).

Next, intensity values are assigned to each reconstruction point. First, the path between each antenna and the reconstruction position is divided into immersion medium, skin, and the breast interior. The corresponding travel times are calculated and used to identify the portion of the signal associated with the reconstruction point. These signals are then summed for all antennas. When all the voxels have been assigned a value, the result is squared and displayed in 3D or 2D slices through the maximum intensity response (the estimated tumor location).



The intensity of the voxels ( $I(r)$ ) after reconstruction grid definition (Curtis, 2015) will be calculated through *DAS* algorithm as

$$I(r) = \sum_{m=1}^M s_m^2 [\text{round}(\frac{\tau_m(r)}{\Delta t})] \quad (5.1)$$

Where  $\tau_m(r)$ : round-trip time delay from antenna position  $r_m$  to voxel position  $r$ ,  $s_m[n]$ : discrete preprocessed radar signal. This equation implies that the sum of intensities of the time signals will directly impact each voxel's intensity in the final 3D image.

Based on the discussions on pre-processing stages in *TSAR* imaging, conversion of microwave signals between Fourier domains is unavoidable due to the characteristics of processing algorithms which necessitate calculations in frequency and time domain. The nature of delay-and-sum imaging for further intensity estimation of each voxel on a 3D grid is highly dependent on the intensity of individual signals after preprocessing. This indicates that *DFT*-imposed distortions are distributed to the final processed signals and might be suppressed after application of *LPF* (either through pulse shaping by using an equivalent of a *LPF* after frequency truncation or in the form of a hamming window after skin subtraction). This suggests the applicability of Fourier analysis of *TSAR* signals in investigating an alternative for the application of *LPF* to avoid the effects of intensity loss.

## Chapter Six: **Improving basis function characteristics of backscattered signals**

### **6.1 Introduction<sup>10</sup>**

In the previous chapter we explained that tumor detection in microwave imaging techniques such as *TSAR* is based on the high contrast of the tumor response compared to surrounding tissues. In this chapter, we provide information on an alternative Gibbs' removal technique that preserves the contrast of the dominant response. Next, we will show sub-duration shift of time data by Fourier domain manipulation mitigates the ringing effects while preserving the contrast of original back-scattered time data.

In section 6.2, the Fourier manipulation of *TSAR* signals to improve basis function characteristics of backscattered signals is discussed. In section 6.3, the proposed total variation optimization of Fourier shift manipulated data is introduced as a potential alternative for artifact reduction of the microwave imaging signals. Modifications to *TSAR* software [Curtis, 2015] to fit the new algorithm and the simulated breast models used to test the proposed preprocessing algorithm are also introduced in this section. The results of experiments are demonstrated in section 6.4 with the evaluation of proposed technique performed with subjective and objective comparison between unfiltered data, filtered data and data affected by the proposed method. The conclusions are drawn and possible future extensions are discussed in section 6.5.

---

<sup>10</sup> This chapter is based on the paper "Fourier manipulation of Tissue Sensing Adaptive Radar data to improve Tumor Detection Accuracy by Gibbs' Ringing Removal" by Paniz Adibpour, Michael Smith and Elise Fear, Under preparation for submission to IEEE Transactions on Computational Imaging or Progress in Electromagnetics Research by March 2018.

## 6.2 Fourier manipulation of backscattered signals to improve basis function characteristics

An early study in (Smith, 1993) aimed at avoiding the necessary application of resolution-destroying windows to mitigate the impact of truncation artifacts inherent in *DFT*-based algorithms by suggesting minor adjustments in the experimental data gathering procedures. This idea which is discussed in detail in section 4.4.2 is examined in the context of microwave imaging due to the *DFT* basis of the preprocessing procedure of the *TSAR* algorithm.

Windowing, which results in convolution in time domain with a sinc function, imposes ringing artifacts on the time-domain signals except when sampling positions coincide with the zero crossings of Sinc function. Based on this interpretation, optimum sub-duration shift of backscattered time signals via phase ramping (Eqn. 6.1) to match the sampling points to zero crossings of Sinc function will eliminate the side lobes of the sinc function.

$$S_{SHIFT}[f] = S[f] \exp(+j2\pi f T_{SHIFT} / N); \quad -N/2 \leq f \leq N/2 - 1; \quad (6.1)$$

From another point of view, frequency truncation imposes discontinuity which is interpreted in (Harris, 1978) as changing a basis function to a non-basis function in a Fourier space, generating artifacts in the *DFT*-transformed signal. The application of an *LPF* forces continuity in the frequency boundaries by suppressing the high frequency components with the cost of resolution loss. Frequency manipulation of signals by phase ramping aims at mimicking the basis function characteristics.

In realistic cases, there is no individual scatterer embedded in a time-domain response or individual fine object in image space. Therefore, one sub-duration shift might remove ringing artifacts from one scatterer while distorting another. Therefore, a criterion is necessary to choose

local adaptive windows within which Gibbs' effects are minimum. In the following section, this criterion is proposed in *TSAR* software as an optimization filtering technique.

### 6.3 Methods and materials

This section briefly introduces the simulation data which are used to test the algorithms. Next, the total variation (*TV*) optimization of Fourier manipulated backscattered signals is introduced as an alternative for the application of *LPF* in *TSAR* software. Finally, the necessary modifications to the *TSAR* preprocessing pipeline are detailed.

#### 6.3.1 Simulated realistic breast models

Simulated reflections of signals from breast models are obtained with a microwave-frequency simulation tool. The software used to simulate models is a commercial *FDTD* program (*Semcad X*, *SPEAG*, *CH*). Similar to prototype systems, the background of the simulation model is defined as canola oil ( $\epsilon_r = 2.5, \sigma = 0.04 S / m$ ). The model uses validated model of the *BAVA-D* antenna which mimics radiation pattern of a physical ultrawideband antenna used in experiments (Bourqui et al., 2010). A simulation system is demonstrated in Fig. 6.1, showing illumination of a simplified model with the *BAVA-D* antenna. To acquire the signals required to form an image, the antenna is scanned around the breast model to a number of different locations. To acquire the complex reflection coefficients, the spectrum of the received response is divided by the spectrum of the transmitted signal (Curtis, 2015).

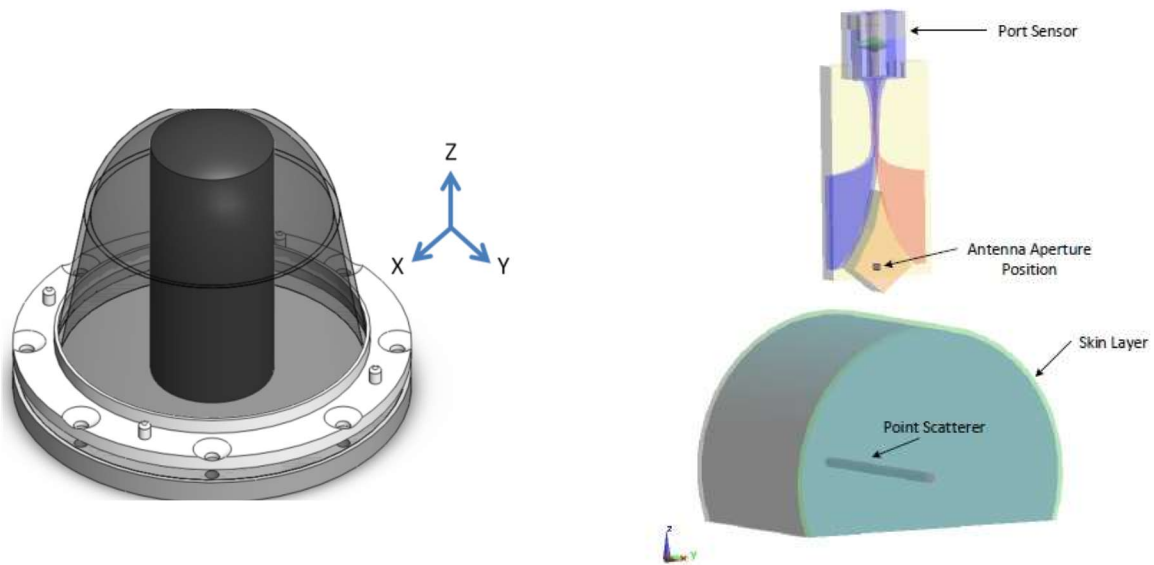


**Figure 6.1 Left: Computer-generated model of the breast phantom; © 2015 IEEE; Right: schematic of antenna and test object in simulation model; screenshot from SEMCAD @C.Curtis (Curtis, 2015)**

Several models, presented in table 6.1, are assessed in this paper. “Tumor only” models are idealistic models including a 1 cm tumor embedded in skin layer. The more sophisticated models include a glandular tissue model or consider additional reflections from the tank. Fig. 6.1 demonstrates a compute-generated model of breast phantom and the schematic of antenna and test object in simulation model. Fig. 6.2 also represents a sample of *TSAR* software result using the baseline pipeline.

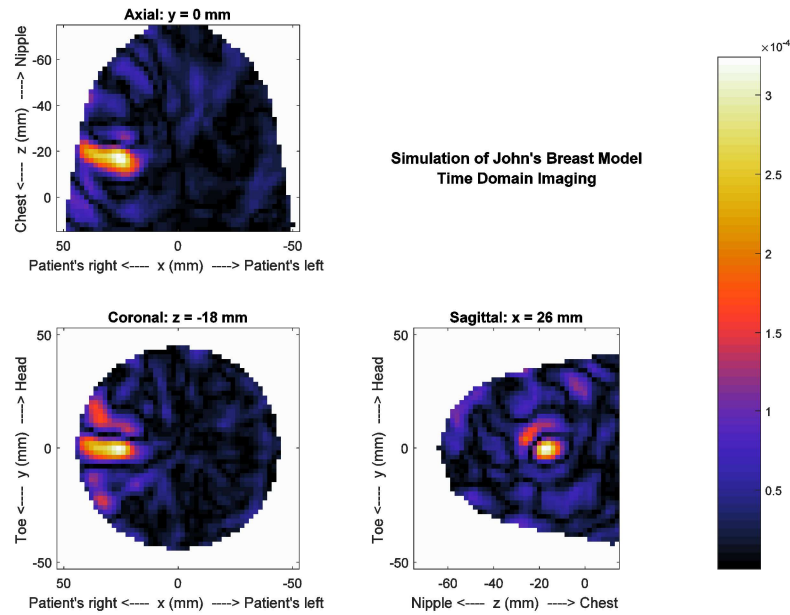


**Figure 6.2** It demonstrates how *TSAR* software generates three different slices of 3D simulated model;

Table 6-1 simulated breast models		
Model	Description of the Model	Tumor Position [x,y,z] mm
Case #1	Tumor #1 inclusion+ reflection from the lid	[25, 0, -17.85]
Case #2	Tumor #2 inclusion, ideal measurement system without tank, tank lid, etc.	[25, 0, -37.85]
Case #3	Tumor #1 inclusion+ single cylindrical Gland	[25, 0, -17.85]
Case #4	Tumor #1 inclusion+ no Glands+ Oil background	[25, 0, -17.85]

### 6.3.2 Total variation optimization of Fourier manipulated back scattered signals

As discussed in section 6.1, signal resampling can eliminate oscillations if resampling points coincide with the zero crossings of the Sinc function convolved with finite-length processed signals. In this section, we introduce an optimization method to automate data resampling.

Let's assume  $S[f \Delta F_N]$  is the Fourier transform of  $s[t \Delta T_N]$  with length  $N$ . A set of signals with sub-duration shifts are created by phase-ramping of the original frequency signal. To

find the appropriate re-sampled signal with minimum oscillation and therefore minimum ringing effects, a total variation ( $TV$ ) calculation metric is used. Variations can be measured by an absolute difference between neighboring time samples as  $TV = |s[t\Delta T_N] - s[(t-1)\Delta T_N]|$ .

Based on the considerations discussed in section 6.1, emphasizing the necessity of local resampling factors where various major scatterers are present in the backscattered signals, we propose to have local  $TV$  measures on adaptive time windows. Major scatterers are identified by detecting the position of major peaks. By calculating the peaks of the envelop of signals, the durations between two time slots where the envelope approaches zero intensity is considered as the approximate window where  $TV$  is measured for an individual scatterer. The window size is kept fixed for all the signals and the Fourier shift for which minimum  $TV$  is calculated is chosen as the optimized phase ramping factor.

$$\min_{T_{sh_i}} \sum_i TV(F^{-1}\{S_i(f) \cdot \exp(j2\pi f T_{sh_i} / N)\}), \quad (6.2)$$

$$\forall i, -1/2 \leq T_{sh_i} \leq 1/4, \forall i = 1, 2, \dots, M, N/2 \leq f \leq N/2 - 1$$

After optimization through Eqn. 6.2, the Fourier shifted signals ( $S_i(r)$  for  $i = 1, \dots, M$ ) have to be then interpolated with appropriate rate to fulfill the requirements discussed in section 5.3.1.

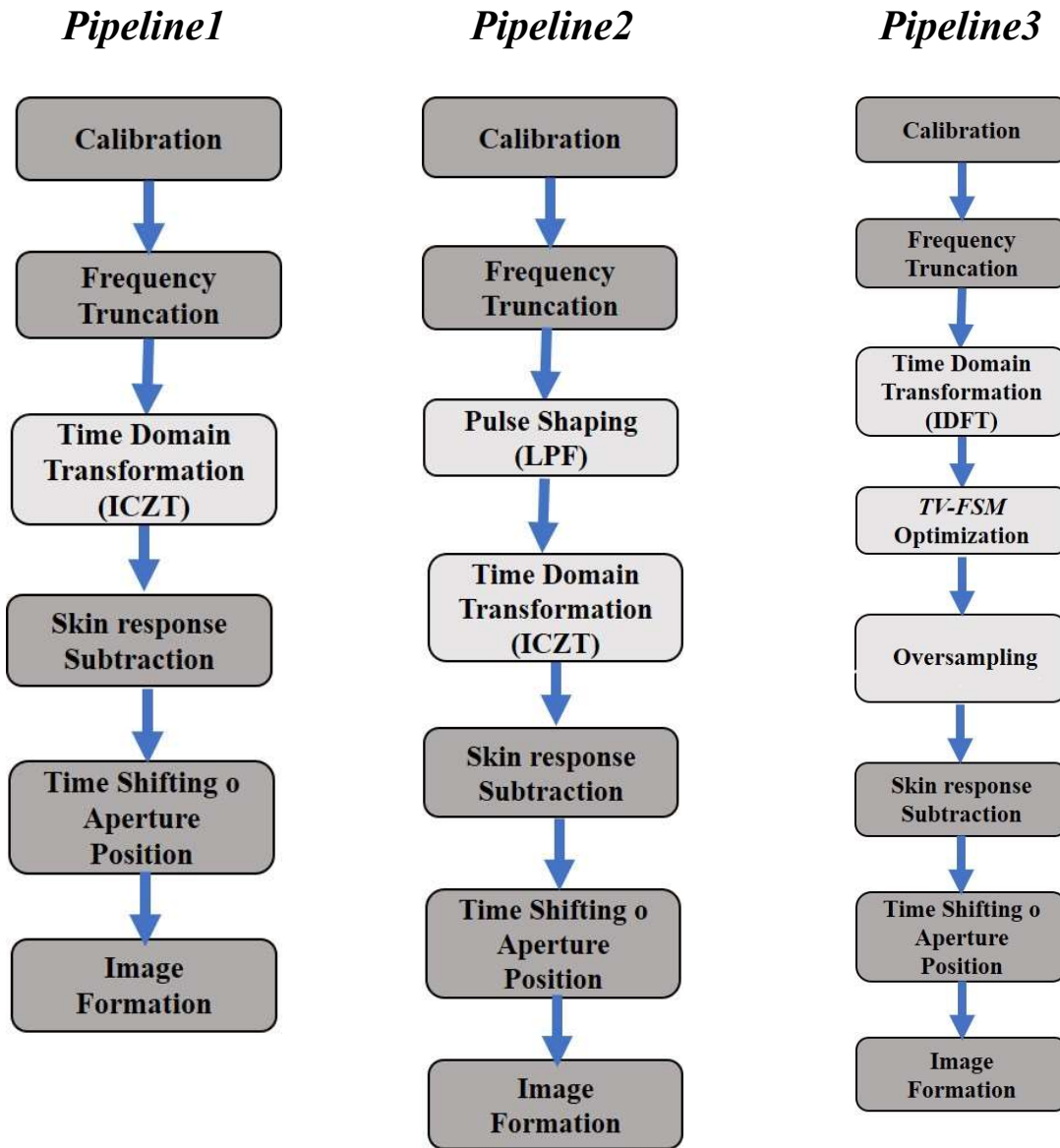


**Figure 6.3** Three pipelines for preprocessing procedure of *TSAR* software different in highlighted sections. Pipeline1: Without pulse shaping; Pipeline2: with pulse shaping; Pipeline3: *TV* optimized of Fourier shifted signals

### 6.3.3 *TSAR* Pipelines

In order to examine the proposed changes in *TSAR* software, three pipelines which are demonstrated in Fig. 6.3 are the focus of our results.



*Pipeline 1:* All necessary preprocessing stages are considered without inclusion of any filtering step throughout the pipeline (Fig. 6.3-A – baseline pipeline).

*Pipeline 2:* All stages of pipeline 1 are included and the effect of low pass filtering is also included in the pipeline as an original solution for *DFT*-imposed artifacts (Fig. 6.3-B – baseline + *LPF*).

*Pipeline 3:* In order to apply the proposed technique in *TSAR* software, the following modifications are included in the preprocessing pipeline. Note that resampling to improve basis function characteristics of signals is only applicable when signals are sampled at the Nyquist rate. As discussed in section 5.3.1, *TSAR* signals are transformed to time domain using *ICZT* with higher sampling rates to decrease quantization errors.

1. Frequency signals are transformed to time domain using *ICZT* or inverse discrete time Fourier transform (*IDFT*) sampled at Nyquist rate.
2. Time signals are optimized using proposed algorithm.
3. The output of the proposed optimization algorithm, total variation optimized Fourier manipulated signals, are oversampled to the appropriate rate used in original pipeline (2 ps) to match the requirements of *TSAR* software for image reconstruction (Curtis, 2015). Since *ICZT* uses Sinc interpolation which itself imposes oscillations to time signals and can be considered as another source of artifacts, we have investigated other types of interpolation to mitigate this effect (Fig. 6.3-C – baseline + *TV-FSM*).

### 6.3.4 Measurement criteria

In microwave imaging context, the signal to clutter ratio (*SCR*) has been extensively used to assess the performance of imaging algorithms. This poorly defined metric can occasionally lead

to a high numerical value for an unfocussed tumor response. In recent microwave imaging literature, new metrics have been introduced and tested on imaging algorithms. Tumor position error is a numerical metric which has been used in testing simulation models for which the position of tumor is known (Curtis, 2015). This metric calculates the Euclidean distance between the estimated and true tumor position.

To assess the three algorithms, two numerical criteria are used in this paper. *SCR* is defined as the ratio of the tumor response to the clutter response. The clutter response as defined in (Fear et al., 2002) is the maximum pixel value outside the tumor volume (tumor volume is considered as the pixels within twice the full width at half maximum (*FWHM*) of the tumor response). *FWHM* is defined as width of the signal at half of its maximum value (Fear et al., 2002).

## 6.4 Results and discussions

In the following sections, first an analysis of various oversampling techniques is evaluated with the aim of searching for an alternative for Sinc interpolation which impose extra oscillations to signals. Then, the effect of three introduced pipelines are evaluated on backscattered signals in terms of intensity and resolution of time signals. The final section represents results of image maps of simulated models using three pipelines and discusses the observations and differences between them.

### 6.4.1 Analysis of oversampling techniques

Before analysis of the final results acquired from three pre-processing procedures of Fig. 6.3, an analysis is done to determine which interpolation technique is more appropriate for over sampling of the time signals. For this purpose, five interpolation techniques are tested on

backscattered data with the same parameters, specifically Sinc, piecewise linear (*PL*), nearest neighbor (*NN*), piecewise cubic hermite (*PCH*) and spline interpolations. *FWHM* and *SCR* metrics are used to assess the results. Pipeline 3 is applied to three of the cases described in table 6.2 for consistency of the results. Table 6.2 represents the results of the metrics applied to a 2D cross section where the maximum response occurs (tumor position). Highest and lowest numerical values of *SCR* and *FWHM*, respectively, are obtained for piecewise linear interpolation. This choice of linear interpolation decreases the oscillations introduced by higher order interpolations such as Sinc interpolation originally used in *TSAR* software. Also, results indicate that the tumor was not detected with the sinc approach for cases #1 and #3, having very low signal to clutter ratio. This suggests that the proposed approach not only preserve the tumor response but also changes the characteristics of the clutter response.

<b>Table 6-2 Measurements on 2D cross sections of the maximum responses</b>						
		Sinc	PL	NN	PCH	Spline
Case #1	FWHM(mm)	(6,4)	(5,4)	(5,4)	(5,4)	(6,4)
	SCR(dB)	.008	<b>.326</b>	.134	.204	.231
Case #2	FWHM(mm)	(3,5)	(3,5)	(4,4)	(3,6)	(3,6)
	SCR(dB)	.302	<b>.447</b>	.188	.423	.289
Case #3	FWHM(mm)	(3,5)	(3,5)	(5,4)	(5,4)	(3,5)
	SCR(dB)	.085	<b>.211</b>	.111	.186	.108

#### 6.4.2 comparison of backscattered signals using three pipelines

Fig. 6.4 presents results of the preprocessing steps when backscattered signals are passed through the three pipelines. This section provides a comparison of characteristics of frequency and time signals and the possible effects of those characteristics on final image maps.

To suppress the nonidealities imposed after skin subtraction or frequency truncation to mitigate noise, the application of a *LPF* within the preprocessing algorithm either after the truncation or before image formation (Fig. 6.4-A-2 & B-2) is of interest. Pipeline 2 of Fig. 6.3 suggests another variant of the preprocessing procedure that considers pulse shaping (*LPF*) effect. As Figs. 6.4-A1, 6.4-B1, 6.4-A2 and 6.4-B2 imply, the application of a *LPF* smoothes out the ringing artifacts in time signals (zoomed-in time signal in A-1 & A-2), while inevitably reducing the intensity of dominant response (left solid arrow in A-1 & A-2). These effects will be further investigated on tumor position accuracy of final images.

As figs. 6.4, A-3 and B-3 demonstrate, the alternative algorithm forces the frequency data to mimic the basis function characteristics. The solid arrow in Fig. 6.4, A-3 shows that the spectrum tends to have continuous characteristics demonstrated by the low pass filtered data in A-2. This therefore degrades the ringing effects in the other Fourier domain due to discontinuity imposed on frequency data after truncation of spectrum (zoomed-in time signal in Fig. 6.4, B-3). On the other hand, this algorithm preserves the actual contrast between the dominant and clutter responses in comparison to the case where low pass filtering is used. Almost 46% of the intensity of the tumor response is decreased after application of *LPF* which will degrade the contrast of tumor and clutter response and can have detrimental effects on tumor detection accuracy.

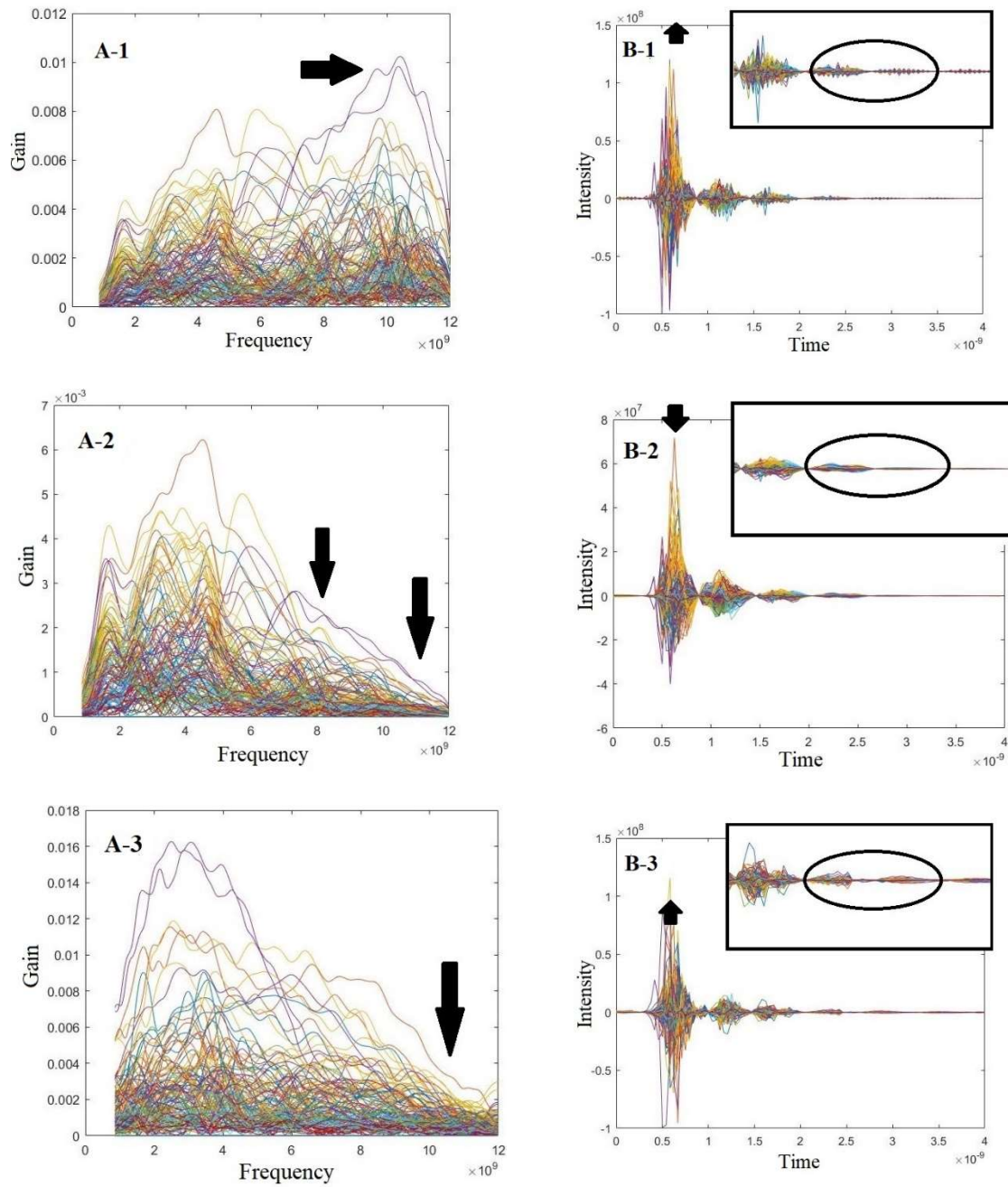


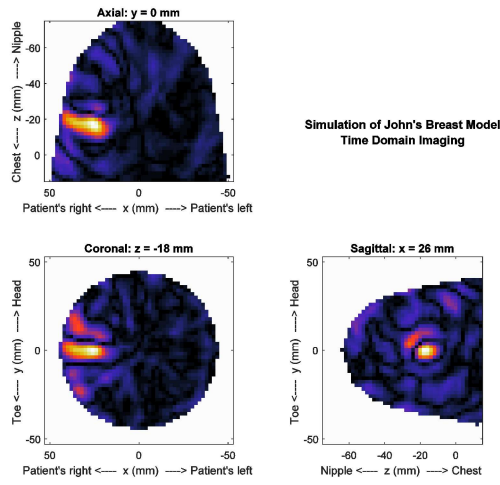
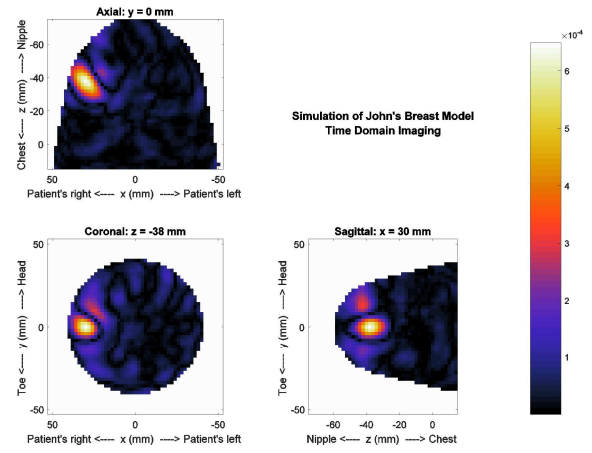
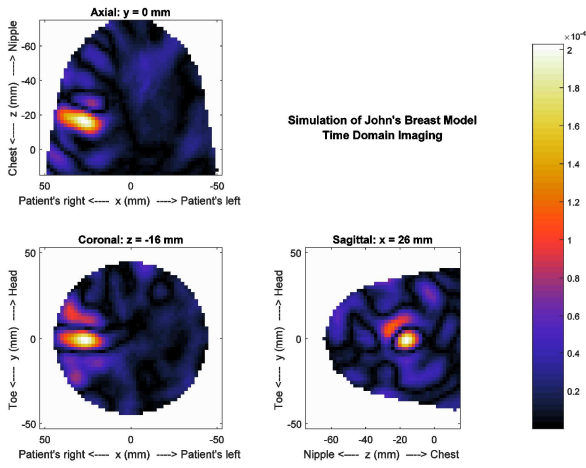
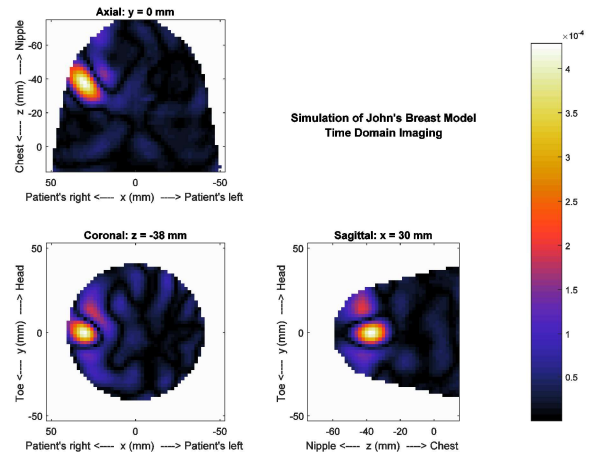
**Figure 6.4** Backscattered signals following three *TSAR* pipelines; A-1)frequency and B-1)time; signals after application of pipeline 1, baseline; A-2)frequency and B-2)time; signals after application of pipeline 2, baseline + *LPF*; A-3)frequency and B-3)time; signals after application of pipeline 3, baseline + *TV-FSM*;

### 6.4.3 Comparison of *TSAR* image maps

#### *Tumor only Models:*

Fig. 6.5 represents results for case #1 and #2 models processed with the 3 different pipelines presented in Fig. 6.3 (where pipeline 3 uses linear oversampling). The 3D images are sliced at the location of maximum intensity and the 2D slices are presented here for better comparison. All the pipelines succeed in generating a focused response. However, x and z slices of the maps from pipeline 1 and pipeline 2 have side lobes around the tumor response location. This is reduced in proposed *TV-FSM* method (c, f) where a more focused response is present in final images. Different characteristics of the clutter are also observed with *TV-FSM*.

The same analysis has been done on models including both tumor and glands. Fig. 6.6 represent the results of *TSAR* images comparing the three pipelines for case #3 and #4. All the algorithms show good tumor localization and appear subjectively consistent. Fig. 6.6.a-c demonstrate the results for a model which includes a 1 cm tumor and a single cylindrical gland. Results from x and z slices indicate that the pipeline 3 leads to a more focused maximum response with more clutter attenuation. The application of *LPF* generates blurriness in 2D reconstructed images and leads to the interference of the adjacent clutter with the tumor response (Fig. 6.6.b). The same interpretation is valid for Fig. 6.6.d-f for which a 1cm tumor is located within a homogeneous background. Low pass filtering imposes blurriness while the proposed algorithm suggests a more focused response with eliminated side lobes.

a) Baseline *TSAR* Imaging (Case #1)d) Baseline *TSAR* Imaging (Case #2)b) *TSAR* imaging + *LPF* (Case #1)e) *TSAR* imaging + *LPF* (Case #2)

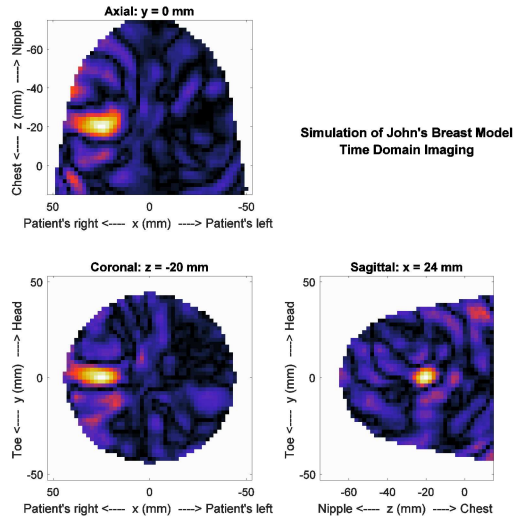
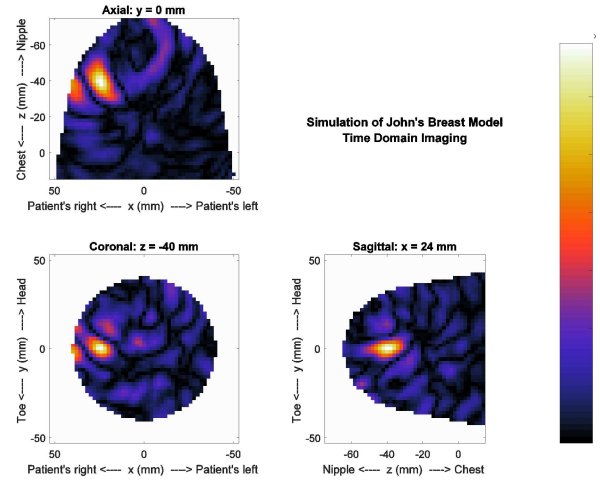
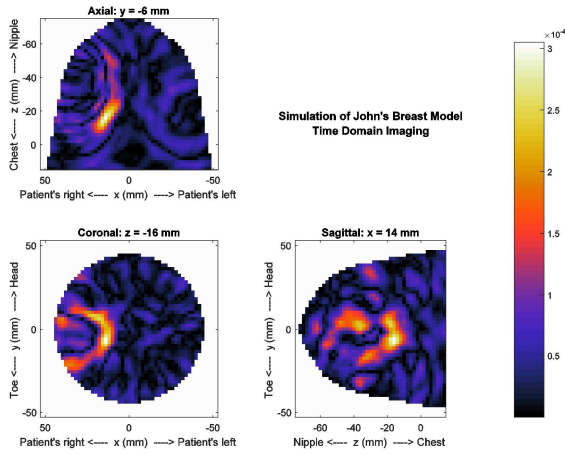
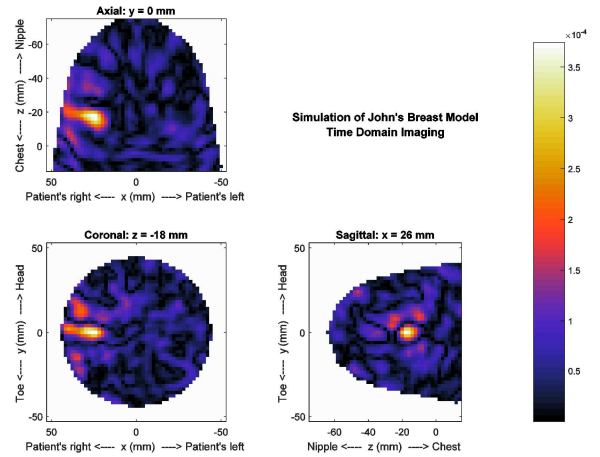
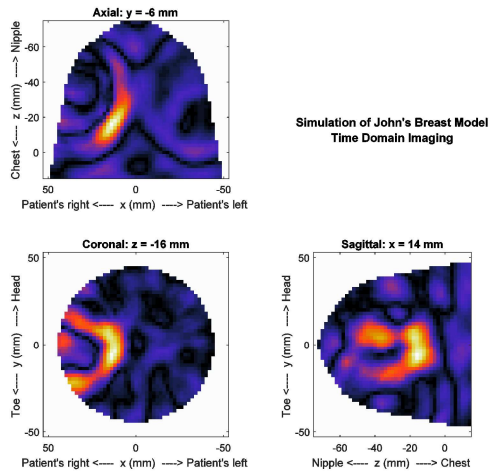
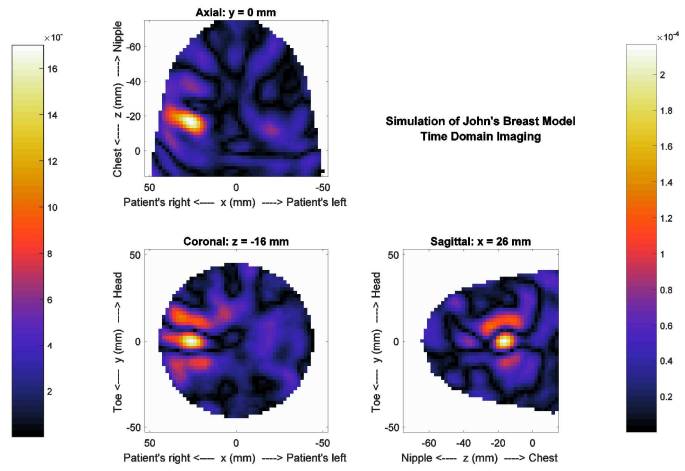
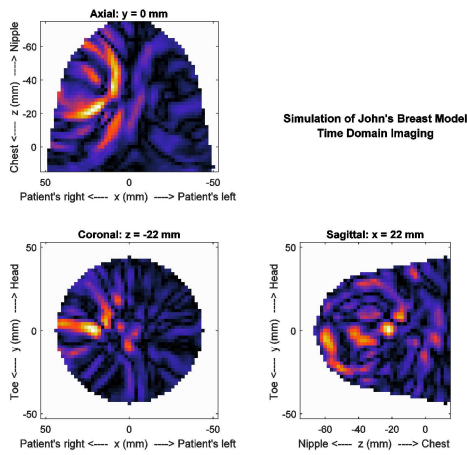
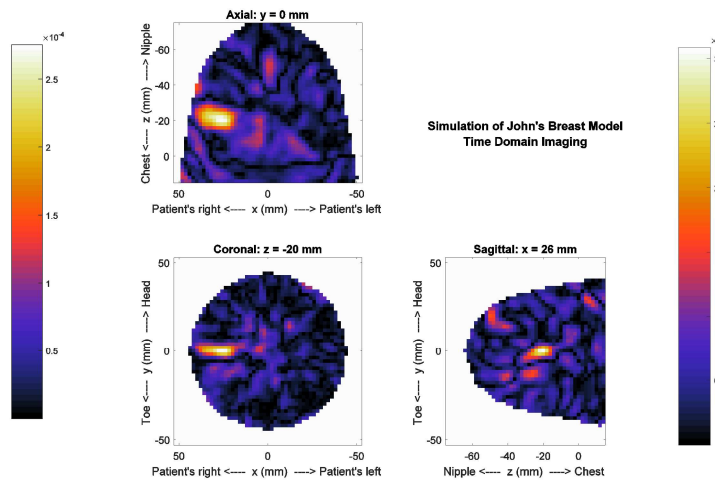
c) *TSAR* imaging + *TV-FSM* (Case #1)f) *TSAR* imaging + *TV-FSM* (Case #2)

Figure 6.5 Images of tumor only models

a) Baseline *TSAR* Imaging (Case #3)d) Baseline *TSAR* Imaging (Case #4)



b) *TSAR* imaging + *LPF* (Case #3)e) *TSAR* imaging + *LPF* (Case #4)c) *TSAR* imaging + *TV-FSM* (Case #3)f) *TSAR* imaging + *TV-FSM* (Case #4)**Figure 6.6 Images of more sophisticated models**

In order to determine how different preprocessing procedures might affect the tumor localization accuracy, the tumor position error, introduced in section 6.2.4, is compared for selected breast models in Fig. 6.7. The position error is in general within a smaller range when *TV-FSM* is used (pipeline 3). For cases 2 and 3, the position error is considerably smaller compared to the procedures including low pass filtering (pipeline 2) and the baseline with no

filtering effects (pipeline 1). Cases 1 and 4 show better position errors with pipelines 2 and 3. However, the position errors are very similar and the differences are neglectable between algorithms. In general, preprocessing procedure with proposed *TV-FSM* changes (pipeline 3) shows more stability in terms of detection accuracy and this is due to the effectiveness of this algorithm in mitigating the *DFT*-imposed artifacts, instead preserving the original intensity of time signals at tumor response locations.

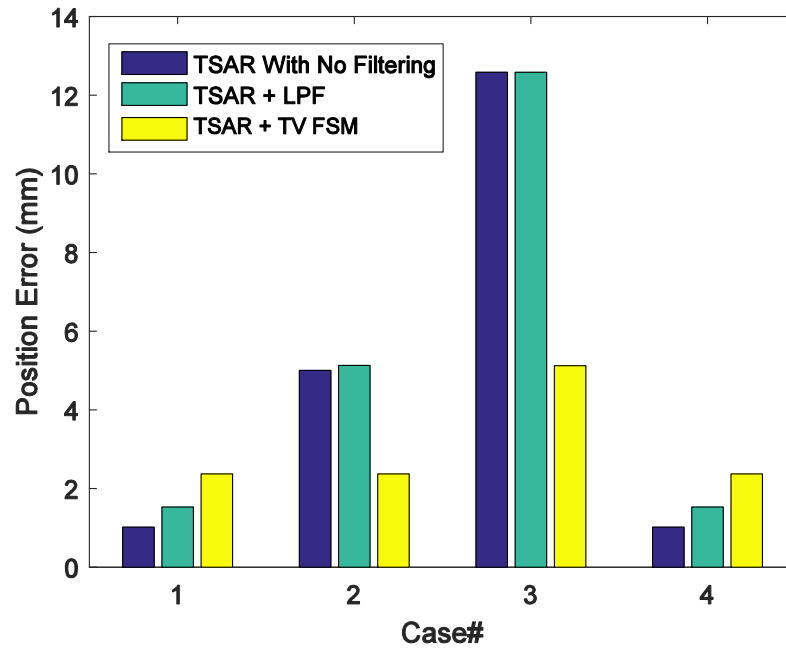


**Figure 6.7 Tumor position error**

## 6.5 Conclusion and Future work

This chapter applies an alternative simple yet effective method to mitigate Gibbs' artifact which is a common distortion in medical imaging applications due to the concerns associated with patient comfort, time resolution or practical limitations of infrastructure for data acquisition. The *TSAR* microwave imaging system, which confronts the same problem, has been studied in this

chapter. The *TSAR* pre-processing algorithm has eliminated oscillation effects using the application of *LPF*. However, the parameters of the *LPF* should be accurately chosen to compromise between smoothing and the inherent imposed resolution loss effects. The application of a proposed *TV* optimization method does not suffer destructive effects of low pass filtering on contrast of signals. Instead, it provides promising results with higher SNR and yet preserves the spatial resolution of final reconstructed image compared to the *LPF*. Results from breast models suggest that, in specific cases, this technique accentuates the tumor response by considerably reducing the ringing and clutter effects. Based on the numerical criterion of tumor position error, the *TSAR* system with proposed changes in pre-processing steps provides more reliable results.

## Chapter Seven: **Conclusion and Future Work**

In this research, preliminary observations of the effects of Fourier manipulation of the data generated during constrained *MR* imaging have led to the exploration of specific fundamental *DFT* properties. Such characteristics founded the basis for investigation of alternative methods capable of correcting *DFT*-imposed artifacts without imposing loss of intensity and resolution to final product of algorithms, e.g. 2D or 3D image maps. The general application of low pass filter (LPF) has long been used as a common and computationally inexpensive method to mitigate inevitable *DFT* artifacts in low resolution biomedical applications without considering its destructive effects on diagnostic results. In fact, the corruption of signals through a pipeline as the result of a loose solution like *LPF*, can propagate to the whole system and cause misinterpretation of final results.

It has been shown through this thesis that taking advantage of *DFT* properties, total variation optimization of Fourier shift manipulated (*FSM*) signals or data can be a potential alternative for *DFT* artifact reduction methods. This method basically aims to target *DFT* artifacts independently and through adaptation of deliberate change in data gathering procedure or deliberate shift of *FOV* through post processing stages, recover the corrupted fine details. The results from the preliminary studies were presented in following conferences for which I was the first author or contributed as co-author:

- **Adibpour, P.**, Smith, M., (June, 2015). An Approach to Improve the Effectiveness of Wavelet and Contourlet Compressed Sensing Reconstruction. *24th International Society of Magnetic Resonance in Medicine, Toronto, Canada.*

- Smith, M. R., MacDonald, M. E., Woehr\* J. and **Adibpour\* P.**, (June, 2015). Overcoming the Image Position-Dependent Resolution Inherent in DFT and CS Reconstructions. *24th International Society of Magnetic Resonance in Medicine, Toronto, Canada.*

Discussions on low resolution *MR* applications, as necessary complementary diagnostic techniques, introduce the need for resolution enhancement of such techniques due to *DFT*-imposed artifacts. This important factor makes *MR* applications an appropriate potential framework where the alternative proposed optimization method can be examined and integrated into *MR* reconstruction techniques. One of the very common and recent reconstruction methods which takes the attention of many current *MR* studies is compressed sensing. It has been shown that such sparse reconstruction method neglects independently addressing *DFT* artifacts and noise-like under-sampling artifacts. This thesis addresses this issue and integrates total variation optimization of Fourier manipulated data into one of compressed sensing algorithms based on analytical sparse basis named *SPARSE-MRI* by introducing two varieties of scenarios. In the first scenario, it is assumed that a preliminary initial scan is used to adjust *FOV* of scanned object. Taking advantage of Fourier manipulation information from this reference scan provides highly accurate *FSM* estimations which can further be applied on acquired under-sampled data.

The second scenario is when a reference scan is not available for this analysis. Then the only dataset which can directly be used in *FSM* estimation is zero-filled under-sampled data. However, experiments show that this dataset is too noisy to be able to provide accurate *FSM* information since random under-sampling imposes Gaussian-noise-like artifacts. Therefore, it is suggested to make use of an equivalent of a not-very-strong wiener filter to boost the *SNR* of zero-filled data and acquire *FSM* information from this manipulated zero-filled data. It is shown

that results from the first scenario are more accurate. While the second scenario still outperforms the original pipeline results, there is room to improve this method in the future to show comparable results to the former method. The methods used for validation of results are preliminary observer methods which are less common in literature while providing the highest correlation to subjective mean-opinion-score results. It is shown from metric results how the proposed methods succeed in recovering structural information of parts where highly affected by *DFT*-imposed artifacts. Results from these studies were presented in following conference and journal papers:

- **Adibpour, P.**, Smith, M. R., (Oct. 29<sup>th</sup>-Nov. 6<sup>th</sup>, 2016). Total Variation Assisted Fourier Shift Manipulation to Remove Gibbs' Artifacts in Compressive Sensing Techniques. *IEEE MIC, Strasbourg, France*, Poster Presentation.
- **Adibpour, P.**, Fear, E., Smith, M., (2017). Improved Compressive Sensing Resolution through Optimization of Basis Function Sparse Representation. *Ready for submission to IEEE Transaction on Computational Imaging by late January, 2018.*

Through this study, a new generation of *CS* techniques, *DL-MRI*, for which patch-based dictionary sets are defined first to more accurately model local features of objects in sparse bases. This method not only suffers from similar *DFT* artifacts but also the destructive effects of *DFT* artifacts are way higher than the former *CS* method. It is shown that the application of the proposed optimization method benefits this algorithm even more and not only recovers peak intensity of fine details but also mitigates residual artifacts. This study is submitted in the following conference paper:

- **Adibpour, P.,** Fear, E., Smith, M., (2018). Improved Dictionary learning compressed sensing for MRI through Patch-based total variation regularization. *Submitted October 2017 for IEEE International Conference on Acoustics, Speech and Signal Processing (ICASSP), Calgary, Canada.*

In order to generalize suggested method in various *DFT*-based algorithms, one of the microwave imaging techniques, tissue sensing adaptive radar (*TSAR*), is chosen as the third target of this thesis. This algorithm through which backscattered microwave signals go through a preprocessing pipeline and then image maps are generated through a delay-and-sum algorithm integrating all signals to achieve a pixel value, has several sources of resolution loss. Truncation of signals to avoid high frequency noise, application of Sinc oversampling which is a source of artifact itself and on top of those, application of *LPF* to mitigate those effects. It has not been considered that *LPF* proposes hard intensity loss to time signals which is dangerous considering the fact that contrast of malignant and natural tissues are the basis for tumor detection. Changes to the *TSAR* pipeline is proposed by which the application of *LPF* is removed from the pipeline, the proposed total variation optimization of *FSM* estimation of microwave signals are applied and a linear oversampling instead of sinc interpolation is suggested to the original pipeline. Results indicate that the proposed pipeline not only helps accentuating tumor response, it generates more focused response and also helps to undermine clutter responses. The results from his study is also included into the following journal paper which is under preparation:

- **Adibpour, P.,** Smith, M., Fear, E., (2017). Fourier manipulation of Tissue Sensing Adaptive Radar data to improve Tumor Detection Accuracy by Gibbs' Ringing Removal. *Under revision for submission to IEEE Transactions on Computational Imaging or Progress in Electromagnetics Research by March 2018.*

## References

- (Aharon et al., 2006) Aharon, M., Elad, M., & Bruckstein, A. (2006).  $\ell_1$ -SVD: An algorithm for designing overcomplete dictionaries for sparse representation. *IEEE Transactions on signal processing*, 54(11), 4311-4322.
- (Allen et al., 2012) Allen, L. M., Hasso, A. N., Handwerker, J., & Farid, H. (2012). Sequence-specific MR imaging findings that are useful in dating ischemic stroke. *Radiographics*, 32(5), 1285-1297.
- (American Cancer Society) American Cancer Society, "Cancer facts and figures 2005," Amer. Cancer Soc., Atlanta, GA, 2005.
- (Anand and Sahambi, 2008) Anand, C. S., & Sahambi, J. S. (2008, November). MRI denoising using bilateral filter in redundant wavelet domain. In *TENCON 2008-2008 IEEE Region 10 Conference* (pp. 1-6). IEEE.
- (Basant et al., 2013) Kumar, B., Kumar, S. B., & Kumar, C. (2013, December). Development of improved SSIM quality index for compressed medical images. In *Image Information Processing (ICIIP), 2013 IEEE Second International Conference on* (pp. 251-255). IEEE.
- (Bernstein et al., 2004) Bernstein, M. A., King, K. F., & Zhou, X. J. (2004). *Handbook of MRI pulse sequences*. Elsevier.



- (Bihan et al., 1986) Le Bihan, D., Breton, E., Lallemand, D., Grenier, P., Cabanis, E., & Laval-Jeantet, M. (1986). MR imaging of intravoxel incoherent motions: application to diffusion and perfusion in neurologic disorders. *Radiology*, 161(2), 401-407.
- (Bihan et al., 2006) Le Bihan, D., Urayama, S. I., Aso, T., Hanakawa, T., & Fukuyama, H. (2006). Direct and fast detection of neuronal activation in the human brain with diffusion MRI. *Proceedings of the National Academy of Sciences*, 103(21), 8263-8268.
- (Bond et al., 2003) Bond, E. J., Li, X., Hagness, S. C., & Van Veen, B. D. (2003). Microwave imaging via space-time beamforming for early detection of breast cancer. *IEEE Transactions on Antennas and Propagation*, 51(8), 1690-1705.
- (Borman and Stevenson, 1998) Borman, S., & Stevenson, R. L. (1998, August). Super-resolution from image sequences-a review. In *Circuits and Systems, 1998. Proceedings. 1998 Midwest Symposium on*(pp. 374-378). IEEE.
- (Bourqui et al., 2010) Bourqui, J., Okoniewski, M., & Fear, E. C. (2010). Balanced antipodal Vivaldi antenna with dielectric director for near-field microwave imaging. *IEEE Transactions on Antennas and Propagation*, 58(7), 2318-2326.
- (Candes and Wakin, 2008) Candès, E. J., & Wakin, M. B. (2008). An introduction to compressive sampling. *IEEE signal processing magazine*, 25(2), 21-30.
- (Chen et al., 2001) Chen, S. S., Donoho, D. L., & Saunders, M. A. (2001). Atomic decomposition by basis pursuit. *SIAM review*, 43(1), 129-159.

- (Chilla et al., 2015) Chilla, G. S., Tan, C. H., Xu, C., & Poh, C. L. (2015). Diffusion weighted magnetic resonance imaging and its recent trend—a survey. *Quantitative imaging in medicine and surgery*, 5(3), 407.
- (Curtis and Fear, 2014) Curtis, C., & Fear, E. (2014, April). Beamforming in the frequency domain with applications to microwave breast imaging. In *Antennas and Propagation (EuCAP), 2014 8th European Conference on* (pp. 72-76). IEEE.
- (Curtis, 2015) Curtis, C., (2015). Factors Affecting Image Quality in Near-field Ultra-wideband Radar Imaging for Biomedical Applications, *university of Calgary*.
- (Curtis et al., 2017) Curtis, C., Lavoie, B. R., & Fear, E. (2017). An Analysis of the Assumptions Inherent to Near Field Beamforming for Biomedical Applications. *IEEE Transactions on Computational Imaging*.
- (Doneva et al., 2010) Doneva, M., Börnert, P., Eggers, H., Stehning, C., Sénégas, J., & Mertins, A. (2010). Compressed sensing reconstruction for magnetic resonance parameter mapping. *Magnetic Resonance in Medicine*, 64(4), 1114-1120.
- (Donoho, 2006) Donoho, D. L. (2006). Compressed sensing. *IEEE Transactions on information theory*, 52(4), 1289-1306.
- (Dyrby et al., 2011) Dyrby, T. B., Lundell, H. M., Liptrot, M. G., Burke, M. W., Ptito, M., & Siebner, H. R. (2011). Interpolation of DWI prior to DTI reconstruction, and its validation. In *International Society for Magnetic Resonance in Medicine* (Vol. 19, p. 1917).

- (Eckert and Bradley, 1998) Eckert, M. P., & Bradley, A. P. (1998). Perceptual quality metrics applied to still image compression. *Signal processing*, 70(3), 177-200.
- (Engan et al., 1999) Engan, K., Aase, S. O., & Husoy, J. H. (1999). Method of optimal directions for frame design. In *Acoustics, Speech, and Signal Processing, 1999. Proceedings., 1999 IEEE International Conference on* (Vol. 5, pp. 2443-2446). IEEE.
- (Eskicioglu and Fisher, 1995) Eskicioglu, A. M., & Fisher, P. S. (1995). Image quality measures and their performance. *IEEE Transactions on communications*, 43(12), 2959-2965.
- (Fear et al., 2002) Fear, E. C., Li, X., Hagness, S. C., & Stuchly, M. A. (2002). Confocal microwave imaging for breast cancer detection: Localization of tumors in three dimensions. *IEEE Transactions on Biomedical Engineering*, 49(8), 812-822.
- (Ferreira et al., 2009) Ferreira, P., Gatehouse, P., Kellman, P., Bucciarelli-Ducci, C., & Firmin, D. (2009). Variability of myocardial perfusion dark rim Gibbs artifacts due to sub-pixel shifts. *Journal of Cardiovascular Magnetic Resonance*, 11(1), 17.
- (Fuhrmann et al., 1995) Fuhrmann, R. A., Wehrbein, H., Langen, H. J., & Diedrich, P. R. (1995). Assessment of the dentate alveolar process with high resolution computed tomography. *Dentomaxillofacial Radiology*, 24(1), 50-54.
- (Gallichan et al., 2009) Gallichan, D., Scholz, J., Bartsch, A., Behrens, T. E., Robson, M. D., & Miller, K. L. (2010). Addressing a systematic vibration artifact in diffusion-weighted MRI. *Human brain mapping*, 31(2), 193-202.

(Girod, 1993) Girod, B. (1993). What's wrong with mean-squared error. *Digital images and human vision*, 207-220.

(Gregoria et al., 2013) Andria, G., Attivissimo, F., & Lanzolla, A. M. L. (2013). A statistical approach for MR and CT images comparison. *Measurement*, 46(1), 57-65.

(Haacke et al., 1999) Brown, R. W., Haacke, E. M., Cheng, Y. C. N., Thompson, M. R., & Venkatesan, R. (2014). *Magnetic resonance imaging: physical principles and sequence design*. John Wiley & Sons.

(Hagness et al., 1998) Hagness, S. C., Taflove, A., & Bridges, J. E. (1998). Two-dimensional FDTD analysis of a pulsed microwave confocal system for breast cancer detection: Fixed-focus and antenna-array sensors. *IEEE Transactions on Biomedical Engineering*, 45(12), 1470-1479.

(Haldar, 2014) Haldar, J. P. (2014). Low-Rank Modeling of Local  $k$ -Space Neighborhoods (LORAKS) for Constrained MRI. *IEEE transactions on medical imaging*, 33(3), 668-681.

(Hao et al., 2013) Hao, W., Li, J., Qu, X., & Dong, Z. (2013). Fast iterative contourlet thresholding for compressed sensing MRI. *Electronics Letters*, 49(19), 1206-1208.

(Harris, 1978) Harris, F. J. (1978). On the use of windows for harmonic analysis with the discrete Fourier transform. *Proceedings of the IEEE*, 66(1), 51-83.

(Henkelman, 1985) Henkelman, R. M. (1986). Erratum: Measurement of signal intensities in the presence of noise in MR images [Med. Phys. 12, 232 (1985)]. *Medical physics*, 13(4), 544-544.

- (Hinshaw and Lent, 1983) Hinshaw, W. S., & Lent, A. H. (1983). An introduction to NMR imaging: From the Bloch equation to the imaging equation. *Proceedings of the IEEE*, 71(3), 338-350.
- (Hollingsworth, 2015) Hollingsworth, K. G. (2015). Reducing acquisition time in clinical MRI by data undersampling and compressed sensing reconstruction. *Physics in medicine and biology*, 60(21), R297.
- (Huang et al., 2014) Huang, Y., Paisley, J., Lin, Q., Ding, X., Fu, X., & Zhang, X. P. (2014). Bayesian nonparametric dictionary learning for compressed sensing MRI. *IEEE Transactions on Image Processing*, 23(12), 5007-5019.
- (Jesmanowicz et al., 1998) Jesmanowicz, A., Bandettini, P. A., & Hyde, J. S. (1998). Single-shot half k-space high-resolution gradient-recalled EPI for fMRI at 3 tesla. *Magnetic Resonance in Medicine*, 40(5), 754-762.
- (Jiang et al., 2013) Jiang, M., Jin, J., Liu, F., Yu, Y., Xia, L., Wang, Y., & Crozier, S. (2013). Sparsity-constrained SENSE reconstruction: an efficient implementation using a fast composite splitting algorithm. *Magnetic resonance imaging*, 31(7), 1218-1227.
- (Kellner et al., 2016) Kellner, E., Dhital, B., Kiselev, V. G., & Reiser, M. (2016). Gibbs-ringing artifact removal based on local subvoxel-shifts. *Magnetic resonance in medicine*, 76(5), 1574-1581.
- (Kim et al., 1997) Kim, S. G., Richter, W., & Uğurbil, K. (1997). Limitations of temporal resolution in functional MRI. *Magnetic resonance in medicine*, 37(4), 631-636.

- (Kim et al., 2009) Kim, Y., Altbach, M., Trouard, T., & Bilgin, A. (2009). Compressed sensing using dual-tree complex wavelet transform. In *Proceedings of the International Society for Magnetic Resonance in Medicine* (Vol. 17, p. 2814).
- (Kim et al., 2010) Kim, Y., Nadar, M. S., & Bilgin, A. (2010, September). Compressed sensing using a Gaussian scale mixtures model in wavelet domain. In *Image Processing (ICIP), 2010 17th IEEE International Conference on* (pp. 3365-3368). IEEE.
- (Lehmann et al., 1999) Lehmann, T. M., Gonner, C., & Spitzer, K. (1999). Survey: Interpolation methods in medical image processing. *IEEE transactions on medical imaging*, 18(11), 1049-1075.
- (Liang and Lauterbur, 1999) Liang, Z. P., & Lauterbur, P. C. (2000). *Principles of magnetic resonance imaging: a signal processing perspective*. SPIE Optical Engineering Press.
- (Liu et al., 2013) Liu, Q., Wang, S., Ying, L., Peng, X., Zhu, Y., & Liang, D. (2013). Adaptive dictionary learning in sparse gradient domain for image recovery. *IEEE Transactions on Image Processing*, 22(12), 4652-4663.
- (Ljunggren, 1983) Ljunggren, S. (1983). A simple graphical representation of Fourier-based imaging methods. *Journal of Magnetic Resonance (1969)*, 54(2), 338-343.
- (Lustig et al., 2007) Lustig, M., Donoho, D., & Pauly, J. M. (2007). Sparse MRI: The application of compressed sensing for rapid MR imaging. *Magnetic resonance in medicine*, 58(6), 1182-1195.

- (Lustig et al., 2008) Lustig, M., Donoho, D. L., Santos, J. M., & Pauly, J. M. (2008). Compressed sensing MRI. *IEEE signal processing magazine*, 25(2), 72-82.
- (Lustig, 2006) M. Lustig, 2006 [Online]. Available: <http://www.stanford.edu/~mlustig/>
- (Ma et al., 2008) Ma, S., Yin, W., Zhang, Y., & Chakraborty, A. (2008, June). An efficient algorithm for compressed MR imaging using total variation and wavelets. In *Computer Vision and Pattern Recognition, 2008. CVPR 2008. IEEE Conference on* (pp. 1-8). IEEE.
- (Ma, 2011) Ma, J. (2011). Improved iterative curvelet thresholding for compressed sensing and measurement. *IEEE Transactions on Instrumentation and Measurement*, 60(1), 126-136.
- (Maklad et al., 2012) Maklad, B., Curtis, C., Fear, E. C., & Messier, G. G. (2012). Neighborhood-based algorithm to facilitate the reduction of skin reflections in radar-based microwave imaging. *Progress In Electromagnetics Research B*, 39, 115-139.
- (Mantiuk et al., 2011) Mantiuk, R., Kim, K. J., Rempel, A. G., & Heidrich, W. (2011, August). HDR-VDP-2: A calibrated visual metric for visibility and quality predictions in all luminance conditions. In *ACM Transactions on Graphics (TOG)* (Vol. 30, No. 4, p. 40). ACM.
- (Mayer and Vrscaj, 2007) Mayer, G. S., & Vrscaj, E. R. (2007). Measuring information gain for frequency-encoded super-resolution MRI. *Magnetic resonance imaging*, 25(7), 1058-1069.
- (McGibney et al., 1993) McGibney, G., Smith, M. R., Nichols, S. T., & Crawley, A. (1993). Quantitative evaluation of several partial Fourier reconstruction algorithms used in MRI. *Magnetic resonance in medicine*, 30(1), 51-59.

- (McRobbie et al., 2003) McRobbie, D. W., Moore, E. A., & Graves, M. J. (2017). *MRI from Picture to Proton*. Cambridge university press.
- (Morgan and Bair, 2013) Morgan, W. F., & Bair, W. J. (2013). Issues in low dose radiation biology: the controversy continues. A perspective. *Radiation research*, 179(5), 501-510.
- (Olshausen and Field, 1996) Olshausen, B. A. (1996). Emergence of simple-cell receptive field properties by learning a sparse code for natural images. *Nature*, 381(6583), 607-609.
- (Pappas and Safranek, 2000) Pappas, T. N., Safranek, R. J., & Chen, J. (2000). Perceptual criteria for image quality evaluation. *Handbook of image and video processing*, 669-684.
- (Pejoski et al., 2015) Pejoski, S., Kafedziski, V., & Gleich, D. (2015). Compressed sensing MRI using discrete nonseparable shearlet transform and FISTA. *IEEE Signal Processing Letters*, 22(10), 1566-1570.
- (Peled and Yeshurun, 2001) Peled, S., & Yeshurun, Y. (2001). Superresolution in MRI: application to human white matter fiber tract visualization by diffusion tensor imaging. *Magnetic resonance in medicine*, 45(1), 29-35.
- (Plenge et al., 2012) Plenge, E., Poot, D. H., Bernsen, M., Kotek, G., Houston, G., Wielopolski, P., & Meijering, E. (2012). Super-resolution methods in MRI: Can they improve the trade-off between resolution, signal-to-noise ratio, and acquisition time?. *Magnetic resonance in medicine*, 68(6), 1983-1993.
- (Qu et al., 2002) Qu, G., Zhang, D., & Yan, P. (2002). Information measure for performance of image fusion. *Electronics letters*, 38(7), 313-315.



- (Qu et al., 2010) Qu, X., Cao, X., Guo, D., Hu, C., & Chen, Z. (2010). Combined sparsifying transforms for compressed sensing MRI. *Electronics letters*, 46(2), 121-123.
- (Ravishankar et al., 2011) Ravishankar, S., & Bresler, Y. (2011). MR image reconstruction from highly undersampled k-space data by dictionary learning. *IEEE transactions on medical imaging*, 30(5), 1028-1041.
- (Sill and Fear, 2005) Sill, J. M., & Fear, E. C. (2005). Tissue sensing adaptive radar for breast cancer detection—Experimental investigation of simple tumor models. *IEEE Transactions on Microwave theory and Techniques*, 53(11), 3312-3319.
- (Silverstein and Farrelt, 1996) Silverstein, D. A., & Farrell, J. E. (1996, September). The relationship between image fidelity and image quality. In *Image Processing, 1996. Proceedings, International Conference on* (Vol. 1, pp. 881-884). IEEE.
- (Smith, 1993) Smith, M. R. (1993). FFT—fRISCy fourier transforms?. *Microprocessors and Microsystems*, 17(9), 507-521.
- (Smith et al., 2013) Smith, M., Woehr, J., Marasco, E., & MacDonald, M. E. (2013). Impact of DFT properties on the inherent resolution of compressed sensing reconstructed images.
- (Smith et al., 2015) Smith, M., Woehr, J., MacDonald, M. E., & Adibpour, P. (2015). Overcoming the Image Position-Dependent Resolution Inherent in DFT and CS Reconstruction. In *Proc. Intl. Soc. Mag. Reson. Med* (Vol. 23, p. 3406).
- (Srinivasan et al., 2006) Srinivasan, A., Goyal, M., Azri, F. A., & Lum, C. (2006). State-of-the-art imaging of acute stroke. *Radiographics*, 26(suppl\_1), S75-S95.

- (Stejskal and Tanner, 1965) Stejskal, E. O., & Tanner, J. E. (1965). Spin diffusion measurements: spin echoes in the presence of a time-dependent field gradient. *The journal of chemical physics*, 42(1), 288-292.
- (Teo and Heeger, 1994) Teo, P. C., & Heeger, D. J. (1994, November). Perceptual image distortion. In *Image Processing, 1994. Proceedings. ICIP-94., IEEE International Conference* (Vol. 2, pp. 982-986). IEEE.
- (Thevenaz et al., 2000) Thévenaz, P., Blu, T., & Unser, M. (2000). Image interpolation and resampling. *Handbook of medical imaging, processing and analysis*, 1(1), 393-420.
- (Tieng et al., 2011) Tieng, Q. M., Cowin, G. J., Reutens, D. C., Galloway, G. J., & Vegh, V. (2011). MRI resolution enhancement: How useful are shifted images obtained by changing the demodulation frequency?. *Magnetic resonance in medicine*, 65(3), 664-672.
- (Tsaig and Donoho, 2006) Tsaig, Y., & Donoho, D. L. (2006). Extensions of compressed sensing. *Signal processing*, 86(3), 549-571.
- (Twieg, 1983) Twieg D (1983). "The k-trajectory formulation of the NMR imaging process with applications in analysis and synthesis of imaging methods.". *Medical Physics*. **10** (5): 610–21.
- (Uecker et al., 2010) Uecker, M., Zhang, S., Voit, D., Karaus, A., Merboldt, K. D., & Frahm, J. (2010). Real-time MRI at a resolution of 20 ms. *NMR in Biomedicine*, 23(8), 986-994.
- (Wang et al., 2004) Wang, Z., Bovik, A. C., Sheikh, H. R., & Simoncelli, E. P. (2004). Image quality assessment: from error visibility to structural similarity. *IEEE transactions on image processing*, 13(4), 600-612.

- (Wiest et al., 2008) Wiest-Daesslé, N., Prima, S., Coupé, P., Morrissey, S. P., & Barillot, C. (2008, September). Rician noise removal by non-local means filtering for low signal-to-noise ratio MRI: applications to DT-MRI. In *International Conference on Medical Image Computing and Computer-assisted Intervention* (pp. 171-179). Springer Berlin Heidelberg.
- (Winckler, 1999) Winkler, S. (1999). Issues in vision modeling for perceptual video quality assessment. *Signal processing*, 78(2), 231-252.
- (Xydeas and Petrovic, 2000) Xydeas, C. S., & Petrovic, V. (2000). Objective image fusion performance measure. *Electronics letters*, 36(4), 308-309.
- (Yaghoobi et al., 2009) Yaghoobi, M., Blumensath, T., & Davies, M. E. (2009). Dictionary learning for sparse approximations with the majorization method. *IEEE Transactions on Signal Processing*, 57(6), 2178-2191.

## Appendix A

### Copyright Permissions

The following is the list of permissions for materials captured from published papers:

- Figure 2.6 is cited following IEEE requirements. (© 2004 IEEE)
- Figure 6.1 is cited following IEEE requirements. (© 2015 IEEE)

Figures are cited within thesis based on IEEE requirements for illustrations (screenshot of regulation attached below) which are part of a IEEE publication. Terms can be found under the link [https://www.ieee.org/publications\\_standards/publications/rights/permissions\\_faq.pdf](https://www.ieee.org/publications_standards/publications/rights/permissions_faq.pdf)

- **Does IEEE require individuals working on a thesis or dissertation to obtain formal permission for reuse?**

The IEEE does not require individuals working on a thesis to obtain a formal reuse license, however, you must follow the requirements listed below:

#### **Textual Material**

Using short quotes or referring to the work within these papers) users must give full credit to the original source (author, paper, publication) followed by the IEEE copyright line © 2011 IEEE.

In the case of illustrations or tabular material, we require that the copyright line © [Year of original publication] IEEE appear prominently with each reprinted figure and/or table.

If a substantial portion of the original paper is to be used, and if you are not the senior author, also obtain the senior author's approval.